Exploiting the Structure-Property Relationship in Bragg Stacks: From Phononic Superlattices to Bioinspired Hybrids

Dissertation

zur Erlangung des Grades
"Doktor der Naturwissenschaften"
im Promotionsfach Chemie

am Fachbereich Chemie, Pharmazie und Geowissenschaften
der Johannes-Gutenberg-Universität Mainz

vorgelegt von

Faroha Liaqat, M.Phil. M.Sc

geb. in Islamabad (Pakistan)

JG|U

MAINZ, (2014)

Dekan: ████████. c. ████████████

Erster Berichterstatter: ████████████

Zweiter Berichterstatter: ████████████

Tag der mündlichen Prüfung: February 12, 2014

Erklärung

Die vorliegende Arbeit wurde in der Zeit von Juli 2010 bis December 2013 unter Anleitung von Herrn Prof. Dr. Wolfgang Tremel an der Johannes-Gutenberg-Universität Mainz, Institut für Anorganische und Analytische Chemie angefertigt.

Ich erkläre hiermit, dass ich die vorliegende Arbeit selbständig und ohne fremde Hilfe verfasst habe. Alle verwendeten Quellen und Hilfsmittel sind vollständig angegeben.

Mainz

January, 2014.

Dedication

Acknowledgements

I begin in the name of Allah, The Beneficent, The Merciful. Truly, this work would not have been possible without the immense strength I have always derived from Allah. On this long road of continuous toil, I invoked the name of Allah every time I came across an obstacle and never once was I disappointed. This journey is a testament of the rich rewards faith and hard work can bring. I also acknowledge deep love and bless our dearly beloved Prophet Muhammad (Peace be upon him).

In the start, I would like to thank my PhD supervisor, ████████████████████ for his help and guidance during the duration of this work. I am obliged to him for providing me a chance to pursue a PhD degree in his group and for giving new ideas whenever I was looking for some. I appreciate his guidance and mentorship and will always be indebted to him for the knowledge I gained from him.

I had the immense good fortune to have ████████████████ as a co-supervisor for my doctoral work. I always enjoyed our scientific discussions and can well and truly say that his love for science and perfectionism drove me to work harder and better. He was always lively, energetic and knowledgeable and I acknowledge his extensive contributions during the course of my doctoral studies. For all of this, I thank him.

I would also like to thank ████████████████ for the scientific input and calming influence he always brings with him. I am obliged also to ████████████████ for his help and support during the time of my stay in the International Research Training Group (IRTG) for Optoelectronics. I am grateful to ████████████████ and ███████ of the Seoul National University (SNU), South Korea for providing me an opportunity to carry out research in Seoul.

The help and support extended by ████████████████ during the last few years has been immense, be it in research or in my personal life. He has always been like an elder brother to me, guiding where I went astray and providing all the help he could provide. He was a wonderful collaborator in research, providing precursors and help whenever I needed it.

Acknowledgements

I am compelled to mention my friends who helped me whenever I was down, frustrated with the pace of work or when I needed some moral support. It is a blessing to have friends like these in a foreign country, thousands of miles away from home. They made my burden lighter and the road pleasant to travel. I have been very lucky to have friends who were always there for me whenever I needed them.

Acknowledgements

Finally, I come to the people who matter the most and who I love the best. This work would not have been possible without the immense encouragement, constant support and prayers of ███ ███ ████████████████████████. ██████████████████████ ██████████████████████ ██████████████████████ ██████████████████████████ █████████ ██████████████████████████████ █████████ ██████████████████████████ ██████████████████████████ ████████████████████

Publications

1. **"Engineering the Hypersonic Phononic Band Gap of Hybrid Bragg Stacks"**,
   Dirk Schneider, <u>Faroha Liaqat</u>, El Houssaine El Boudouti, Youssef El Hassouani, Bahram Djfari-Rouhani, Wolfgang Tremel, Hans-Jürgen Butt and George Fytas, *Nano Lett*. **2012**, 12, 3101.

2. **"Defect-Controlled Hypersound Propagation in Hybrid Superlattices"**,
   Dirk Schneider, <u>Faroha Liaqat</u>, El Houssaine El Boudouti, Ossama El Abouti, Wolfgang Tremel, Hans- Jürgen Butt, Bahram Djafari-Rouhani and George Fytas, *Phys. Rev. Lett.* **2013**, 111, 164301.

3. **"Ultrastrong Composites from Dopamine-Modified-Infiltrated-Colloidal Crystals"**
   <u>Faroha Liaqat</u>, Muhammad Nawaz Tahir, Michael Kappl, Günter Auernhammer, Dirk Schneider, George Fytas, Kooekheon Char, Hans-Jürgen Butt and Wolfgang Tremel, *Mater. Horiz.* **2015**, 2, 434-441.

4. **"High-Performance TiO_2 nanoparticle/DoPA-Polymer Composites"**,
   <u>Faroha Liaqat</u>, Muhammad Nawaz Tahir, Michael Kappl, Günter Auernhammer, Hand-Jürgen Butt and Wolfgang Tremel, *Macromol. Rapid. Comm.* **2015**, 36, 1129-1137.

5. **"Collective Behavior in Assemblies of Iron Oxide Nanoparticles Imbedded in a Sticky Polymer Matrix Observed by Mössbauer Spectroscopy"**,
   <u>Faroha Liaqat</u>, Sergi Shylin, Muhammad Nawaz Tahir, Vadim Ksenofontov and Wolfgang Tremel, *In progress.*

Conference Proceedings

1. **"Engineering the Band Diagram of One-dimensional Hypersonic Phononic Crystals**",
   <u>Dirk Schneider</u>, Faroha Liaqat, El Houssaine El Boudouti, Youssef El Hassouani, Bahram Djafari-Rouhani, Wolfgang Tremel, Hans-Jürgen Butt, George Fytas, *Meeting of American Physics Society (APS)*, Boston, USA (February, 2012).

2. <u>**Oral Presentation**</u>**: "Creating and Exploring Barriers: Phononic Band Gap in One-dimensional Periodic Bragg Stacks in Hypersonic region",**
   Dirk Schneider, <u>Faroha Liaqat</u>, El Houssaine El Boudouti, Youssef El Hassouani, Bahram Djafari-Rouhani, Wolfgang Tremel, Hans-Jürgen Butt, George Fytas, *IUPAC World Chemistry Congress*, Istanbul, Turkey (August 2013).

3. Participant in *24th International Liquid Crystal Conference, ILCC 2012*, Mainz, Germany (August, 2012).

4. Dirk Schneider, <u>Faroha Liaqat</u>, El Houssaine El Boudouti, Bahram Djafari-Rouhani, Wolfgang Tremel, Hans–Jürgen Butt and George Fytas, *J. Acoust. Soc. Am.* 2011, 130, 2402.

5. <u>**Oral Presentation**</u>**: "A Bioinspired Strategy to Fabricate Bragg Stacks as Hard and Adhesive Coatings",**
   <u>Faroha Liaqat</u>, Muhammad Nawaz Tahir, Michael Kappl, Hans-Jürgen Butt and Wolfgang Tremel, *IUPAC World Chemistry Congress*, Istanbul, Turkey (August, 2013).

6. Participant in summer school on "Optoelectronics", *University of Cambridge, UK* (August, 2011)

7. **<u>Poster Presentation:</u> "A Bioinspired Strategy to Fabricate Bragg Stacks as Hard and Adhesive Coatings",**

   <u>Faroha Liaqat</u>, Muhammad Nawaz Tahir, Michael Kappl, Hans-Jürgen Butt and Wolfgang Tremel, *8th German-Korean Polymer Workshop*, Hamburg, Germany (August 2013).

8. **<u>Oral Presentation</u>: "Ultrastrong Polymer Infiltrated Multilayers of Metal Oxide Nanoparticles",**
   Faroha Liaqat, Muhammad Nawaz Tahir, Eugen Schechtel, Dirk Schneider, George Fytas, Michael Kappl, Hans-Jürgen Butt and <u>Wolfgang Tremel</u>, *Fall Meeting of Material Research Society (MRS)*, Boston, MI, USA (December, 2013).

9. Participant in *Korea - Japan workshop* in Seoul National University, Seoul, South Korea (November, 2012).

Abstract

Structural organization found in many examples from nature provides an inspiring model of engineering to produce smart materials. This approach is based on exploiting the theme of structure-property relationship to design new materials in which the applications stem from their structural aspects. The work presented in this thesis highlights this idea by exploiting diverse properties of specially designed hybrid Bragg stacks built up from different constituent polymer and nanoparticles. This thesis is a compilation of work done on a variety of multilayered systems involving their fabrication and a detailed analysis of their phononic, mechanical and magnetic properties. In particular, one-dimensional phononic crystals are studied in detail to devise ways to mold the flow of elastic energy and obtain a full description of the phononic band diagram which is instrumental in providing an insight into the fundamental concepts of heat management and acousto-optic interactions. In addition, this provides a way to manipulate and control the propagation of elastic waves in periodic materials.

One-dimensional hypersonic phononic structures are fabricated with a high degree of control using a soft matter approach and characterized with the non-destructive technique of spontaneous Brillouin Light Spectroscopy (*BLS*). Hybrid Bragg stacks composed of alternating layers of poly (methyl methacrylate) (*PMMA*) and porous silica (*p-SiO$_2$*) are built up on glass substrate using high-speed spin coating, in contrast to the conventional semi-conductor fabrication techniques. The multilayered stacks exhibit large and well-defined band gaps in the Gigahertz (*GHz*) region of frequency and show direction dependent elastic wave propagation. The complimenting experimental and theoretical dispersion diagrams are fully explained normal to and along the direction of periodicity in the *PMMA/p-SiO$_2$* Bragg stacks. The intensities of the lower and upper phononic branches, the width of the band gap and the phonon frequencies are found to be strongly reliant on the structural parameters of the phononic structures investigated. The elastic modulus and elasto-optic coefficients of the individual layers are also estimated. Oblique incidence significantly alters the phonon propagation and offers a way of engineering the phononic band gap along with an estimation of the shear moduli of the constituents. The phonon dispersion is found to be robust to withstand fabrication related structural imperfections.

Abstract

A second approach to engineer the band gap in one dimensional hypersonic phononic crystals is the introduction of defects in otherwise perfect superlattices. The easy fabrication of *PMMA/p-SiO$_2$* superlattices with superb control makes the task of studying defect-controlled hypersound propagation much simpler. This work includes fabrication and characterization of hybrid superlattices of *PMMA* and *p-SiO$_2$* containing surface and cavity defect layers in isolation or in combination with each other. This is the first observation of surface and cavity modes in soft matter based phononic superlattices and their subsequent interaction. The defects are introduced in the perfect phononic lattice by varying the material, thickness or position of the surface and cavity defect layers. This comprehensive study provides a complete theoretical description of the band diagram based on the Green's function method in addition to the experimental phonon dispersion. Breaking the high symmetry of the phononic superlattice is found to be a way to manipulate the band gap as well as to study the interaction between different defect modes. Such phononic structures with controlled defects are found to contain an optical stop band in addition to a phononic band gap and can qualify as *phoxonic* in nature.

The strength and load-bearing properties of many structural materials found in nature provide motivation to fabricate artificial structures with high mechanical properties. Taking inspiration from super strong nacre and the adhesive character of the constituent *DOPA* (3, 4-dihydroxyphenylalanine) in marine mussels, hybrid multilayers of a polymer rich in catechol groups (DOPA-polymer) and iron oxide nanoparticles (*Fe$_3$O$_4$*) are fabricated by a spin coating procedure. The combination of alternating hard and soft constituent layers cemented by strong interactions between DOPA and iron oxide nanoparticles ensure that the resulting crosslinked network makes the hybrid hard and robust. Nanoindentation studies show very high values of elastic modulus (in GPa) and hardness and the hybrid multilayers can be used as multifunctional adhesive coatings. In addition, the structural ordering in the hybrid multilayers appears to be an important factor in the Mössbauer measurements when the thin films are studied in external magnetic field.

Zusammenfassung

In der Natur gibt es viele Beispiele für geordnete Strukturen, die inspirierende Modelle für die Entwicklung intelligenter Materialien sind. Dieser Ansatz basiert darauf sich die Struktur-Eigenschafts Beziehungen zunutze zu machen, um neue Materialien zu entwerfen, deren Anwendungen auf ihrer strukturellen Beschaffenheit basieren. Die in dieser Dissertation präsentierte Arbeit hebt diese Idee hervor, indem sie sich der vielfältigen Eigenschaften speziell entworfener hybrider Braggstapel aus unterschiedlichen Polymeren und Nanopartikeln bedient. Diese Arbeit ist eine Zusammenstellung einer Vielzahl an mehrschichtigen Systemen sowie deren Herstellung und detaillierte Analyse ihrer phononischen, mechanischen und magnetischen Eigenschaften. Insbesondere werden eindimensionale phononische Kristalle ausführlich untersucht, um Möglichkeiten zu entwickeln, die es erlauben den Fluss der Verformungsenergie zu beeinflussen und eine volle Beschreibung der phononischen Bandstrukturen zu erhalten. Phononische Bandstrukturen sind essentiell für ein tieferes Verständnis der grundlegenden Konzepte des Gitterbeitrags zur Wärmeleitfähigkeit und akustisch-optische Wechselwirkungen. Darüber hinaus kann dadurch die Ausbreitung von elastischen Wellen in periodischen Materialien beeinflusst und kontrolliert werden.

Eindimensionale phononische Strukturen, im Ultraschallbereich, werden mit einem hohen Grad an Kontrolle mittels einer weichen Materie Synthese (soft matter approach) hergestellt und mittels zerstörungsfreier Brillouinlichtspektroskopie (*BLS*) analysiert. Hybride Braggstapel, die aus alternierenden Schichten aus Polymethylmethacrylat (*PMMA*) und porösen Silica (*p-SiO$_2$*) bestehen, werden auf einem Glasträger durch Rotationsbeschichtung (spin coating), im Gegensatz zu konventionellen Halbleiterherstellungsmethoden, aufgebracht. Die vielschichtigen Stapel besitzen große und wohldefinierte Bandlücken im Gigahertzbereich (*GHz*) und zeigen eine richtungsabhängige Ausbreitung elastischer Wellen. Die komplementierten experimentellen und theoretischen Dispersionsdiagramme werden vollständig in Richtung und orthogonal zur Stapelrichtung der *PMMA/p-SiO$_2$* Braggstapel erklärt. Die Intensitäten des unteren und oberen phononischen Zweigs, die Breite der Bandlücke sowie die Frequenzen der Phononen zeigen eine

starke Abhängigkeit von den strukturellen Parametern der untersuchten phononischen Strukturen. Ferner werden die Elastizitätsmoduln und elasto-optischen Koeffizienten der individuellen Schichten abgeschätzt. Der Einfallswinkel beeinflusst die Ausbreitung der Phononen in signifikanter Weise und ermöglicht es die phononische Bandlücke zu konstruieren und eine Abschätzung der Schermoduln der Bestandteile vorzunehmen. Die Phononendispersion ist robust gegenüber fertigungsbedingten strukturellen Fehlordnungen.

Ein zweiter Ansatz zur Konstruktion von Bandlücken in eindimensionalen hypersonischen phononischen Kristallen ist das gezielte Einbringen von Defekten in ansonsten ideale Supergitter. Die leichte Herstellung von *PMMA/p-SiO$_2$* Supergittern mit hervorragender Kontrolle vereinfacht die defektkontrollierte Ultraschallausbreitung. Diese Arbeit beinhaltet die Darstellung und Charakterisierung von hybriden Supergittern aus *PMMA* und *p-SiO$_2$* mit Oberflächen oder internen Defektschichten oder einer Kombination aus beidem. Dies stellt die erste Beobachtung von Oberflächen- und internen Moden in phononischen Supergittern, basierend auf weicher Materie, und deren resultierende Wechselwirkung dar. Defekte werden durch eine Variation des Materials, der Dicke oder der Position der Oberflächen- und internen Defektschichten in das vormals perfekte phononische Gitter eingebracht. Diese umfassende Studie behandelt eine vollständige theoretische Beschreibung des Bändermodells basierend auf der Greenschen Funktionsmethode zusätzlich zu den experimentellen Phononendispersionsdaten. Es wird gezeigt, dass durch einen Symmetriebruch der hohen Symmetrie in dem phononischen Supergitter eine Möglichkeit besteht die Bandstruktur zu beeinflussen sowie die Wechselwirkung zwischen den unterschiedlichen Defektmoden zu untersuchen. Solche phononischen Strukturen mit kontrollierten Defekten verfügen über ein optisches Stopband zusätzlich zur phononischen Bandlücke und qualifizieren sich damit als *phoxonisch*.

Die Stärke und Belastbarkeit vieler Verbundmaterialien in der Natur liefert die Motivation zur Herstellung künstlicher Strukturen mit ebendiesen guten mechanischen Eigenschaften. Als Inspirationsquelle dient Perlmutt mit dessen hoher Widerstandfähigkeit und der adhäsive Charakter von Muschelkleber durch DOPA. In Analogie werden Mehrschichtsysteme aus einem catecholreichen Polymer (DOPA-polymer) und Eisenoxidnanopartikeln (*Fe$_3$O$_4$*) durch Rotationsbeschichtung hergestellt. Die Kombination aus alternierenden einzelnen weichen und harten Schichten wird durch die starken Wechselwirkungen zwischen DOPA und den Eisenoxidnanopartikeln gefestigt und bewirkt, dass die resultieren vernetzten Schichten das Kompositmaterial hart und robust machen. Nanoindentierungsstudien zeigen sehr hohe Werte für

Zusammenfassung

den Elastizitätsmodul (in GPa) und Härte. Die Hybridvielschichten können als multifunktionale adhäsive Beschichtungen verwendet werden. Darüber hinaus scheint die strukturelle Anordnung der hybriden Multilayer einen wichtigen Faktor in den Mössbauermessungen darzustellen, wenn die dünnen Filme in einem externen Magnetfeld gemessen werden.

Table of Contents

Table of Contents

Table of Contents

Motivation

When it comes down to nano-materials, it is the structure that determines the function. This fundamental principle of nano-science and the contemporary advances in technology have enabled scientists to produce intelligent functional materials. Phononic crystals belong to that category of smart materials that have come to light in the past 20 years. The interest in phononics is partly to explore the fundamentals of physics and study the propagation of elastic waves in periodic media. However, the other appealing aspect of working on phononic crystals is the possibility of controlling heat flow and studying acousto-optic interactions. The challenge grows as we move to the hypersonic region of sound propagation. Designing stable nanostructures that can show a phononic band gap in the requisite frequency range is a daunting task. To make the process of fabrication easy is even more challenging.

Inspired by the successful utilization of Bragg stacks in photonic crystals, this work elaborates on the concept to build soft hypersonic phononic superlattices of *PMMA/SiO$_2$*. An advantage of these phononic structures is their ease of fabrication. One-dimensional phononic superlattices allow a separate treatment of the parallel and perpendicular modes of polarization and consequently render a simpler band diagram. In addition, this method of fabrication affords superb structural control. A comparison of the theoretical and experimental models of one dimensional phononic Bragg stacks can provide greater insight into the design of nanostructures and the subsequent effect on the band structure. Synthesis of designed nanocomposite structures capable of having a hypersonic phononic band gap is highly desirable, as it offers an opportunity of studying the phonon-photon interactions by creating a dual photonic-phononic band gap and hence paving way to the realization of phoxonic crystals. Oblique scattering of elastic waves through the one-dimensional phononic Bragg stacks leads to mixing of the transverse and longitudinal polarization modes.

Lastly, the method of fabrication employed makes it much easier to create defects in the *PMMA/SiO$_2$* hybrid phononic superlattices. The defect containing phononic structures can be designed by altering the periodicity, sequence or thickness of individual component layers. These

changes dramatically change the phononic band diagram and shed valuable light on the complex physics of surface and cavity defects. It also affords an easy method of band-gap engineering, a discipline that required extensive efforts earlier.

Taking the theme of hybrid Bragg stacks further and deriving inspiration from nature, the weak polymer and strong inorganic constituent layers are combined alternatively to produce multilayered stacks consisting of a polymer rich in DOPA and iron oxide nanoparticles. The work is described later in the thesis with an emphasis on the mechanical properties of the hybrid stacks. The motivation for the work lies in the strength shown by many biological materials with high structural hierarchy. Nacre is a text book example that combines typically weak constituents in an organized structure to achieve high values of elastic modulus and strength. A polymer rich in catechol groups is chosen as one of the components of the designed Bragg stacks on account of its strong interactions with the iron ions in aqueous environment. This phenomenon has been widely studies in marine mussels with the hope of understanding the adhesion of the byssal mussel threads (which are rich in DOPA) in wet environment. The Bragg stacks thus fabricated, can be used in producing multifunctional hard coatings and magneto-optic devices.

1

Introduction to Bragg Stacks and Phononics

A significant change has been brought on the scientific scene by the advance of Nanotechnology from the second half of the 20th century, as an expertise that transformed the design, methods and characterization of functional materials. Starting from the famous 1959 lecture of Richard Feynmann and his article "There's plenty of room at the bottom", [1] the advances in nanotechnology have been phenomenal. In the words of Richard Smalley, "The resultant technology of our 20th century is fantastic, but it pales when compared to what will be possible when we learn to build things at the ultimate level of control, one atom at a time". It promises to enable scientists to fabricate and control structures at the sub-molecular level and utilize them in cutting edge devices.

A nanoparticle can be considered to be an aggregation of bonded atoms with a dimensional radius of 1-100 nm (*$1nm = 10^{-9}$ m*). [2] Nanostructures can be built up by manipulating and assembling atoms and molecules by the "bottom-up approach", a strategy that is useful in the synthesis of nanoparticles of uniform size and shape. Nano-science exploits the fact that the nano-materials exhibit properties vastly different from their bulk counterparts and these novel characteristics can be used for the development of smart materials having a variety of applications. This structure-property relationship in nanomaterials can be used to make a whole range of devices where the function of the device can be changed by modifying the properties of the constituents. For example, the optoelectronic properties of certain nanoparticles have been actively exploited in devices such as light emitting diodes (*LEDs*), optical sensors and solar cells. [3] Nanomaterials are also used extensively in diagnostics and as bio-sensors [4, 5], for magnetic drug delivery [6, 7], and in sustainable energy applications. [8] The quantum size effect in nanoparticles increases the reactivity at their surface, opening doors for functionalization by polymers, small molecules, surfactants and biomolecules, etc. [9] Using this concept of surface functionalization, the

interactions of the nanoparticles with surround materials or environment can be manipulated and directed to get a self-assembly or designed structures.

Nanostructures come in various sizes, shapes and dimensions. Controlling the morphology and assembly is a way of extracting the desired properties out of a nanomaterial. For example, different synthetic approaches lead to nanoparticles, nanowires, nanotubes, nano-rods or hierarchical structures (Figure 1.1). Thin films and coatings have only one dimension in the nano scale while nano-rods and nanotubes are two dimensional. Nanoparticles having three dimensions include quantum dots, polymer and gold nanoparticles. [4]

Thin films

SiO$_2$ nanoparticles

Quantum dots

Carbon nanotubes

Nanorods
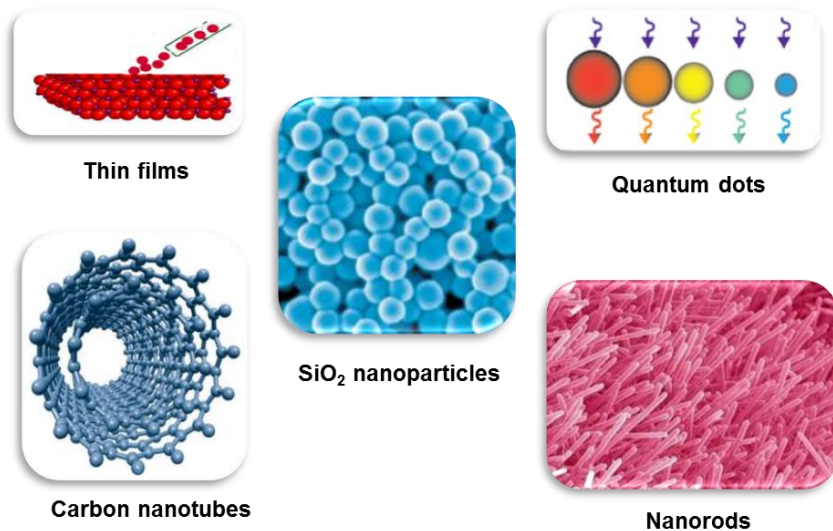
Figure 1.1. *An example of synthetic nanostructures of different shapes and dimensions*

1.1. Structural Organization in Nano-materials

Many interesting properties of nano-materials arise from their shape or organization. Hierarchically ordered systems are commonly seen in nature [10-12] and in recent years, a vast amount of research has gone into designing such structures on a nano scale in a laboratory. [13-15] Structural assemblies can be modeled on natural or synthetic patterns to induce desired properties in nano-structures, be they optical, acoustic, mechanical and electronic, etc. One of the most prominent characteristic of many multilayered nano-materials is structural color. The coloration

Effect is a direct result of interference in multilayered structures. In particular, periodic nano-structures are investigated frequently in recent years as a way of producing desired functional materials.

1.1.1. Bragg Stacks

One-dimensional periodic structures, often known as Bragg Stacks, can be designed to control the propagation of waves through the effective medium. If the electromagnetic waves are forbidden from propagating through the medium in a certain frequency range, the periodic structure is called a Photonic Crystal. [16] Such a Bragg Stack consists of alternating layers of two constituents with a stark refractive index contrast. The frequency range where photons are forbidden is, thus called the Photonic Band Gap. On the other hand, if a Bragg Stack is made up of alternating layers having an acoustic impedance contrast, it gives rise to a Phononic Structure. [17] In such materials, phonons are forbidden from travelling in a certain frequency range known as the Phononic Band Gap (PBG). A schematic of multi-dimensional Bragg stacks is shown in Figure 1.2. The concept of fabrication of Bragg Stacks can also be used to produce hierarchical structures inspired from nature. These periodic structures can be designed to have excellent mechanical properties. Many of these concepts are discussed in detail in the following sections.
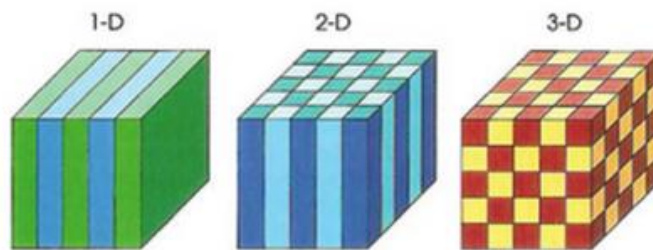
Figure 1.2. Periodicity in Bragg Stacks in one, two or three dimensions (Reference: Nanophotonics: Accessibility and Applicability, The National Academies Press, 2008).

In all multilayered structures, it is necessary that the alternating layers should be held together by specific interactions. [18] These could be electrostatic forces or covalent in nature; the important parameter is to ensure that such interactions exist between subsequent layers so that the second

layer could be easily adsorbed on the first one and the Bragg stack holds. Several other factors come into consideration such as using orthogonal solvents and suitable heat treatment.

1.1.2 Hybrids as Multilayered Assemblies

Architectures in assembled Bragg Stacks can be designed to have alternating films of polymer and nanoparticles, effectively giving rise to a "hybrid". Hybrids or composites are composed of two or more different materials. Inorganic-organic hybrids can be categorized into four groups depending on the embedment or penetration of material A into matrix B (or vice versa) or by maintaining an individual character of A and B. [19] Bragg stacks constructed from alternating polymeric and nanoparticle layers offer the promising perspective of combining the "soft" polymer and "hard" inorganic properties. They also offer a soft matter approach to the field of solid state physics which will be detailed in the coming sections.

1.2. Phononic Crystals

Phononic Crystals (*PhC*) are composite structures having a periodic arrangement of materials with contrasting elastic properties (density/ sound velocity/ elastic constants). Some interesting properties emerge as a result. If the wavelength (λ) of propagating waves is comparable to the periodicity (a) of the phononic structure, a barrier arises over a certain frequency range where propagation of sound or phonons is forbidden. This is known as the Phononic Band Gap. [20] In this regard, the phononic crystals are the acoustic equivalent of photonic crystals. A comparison of both of these periodic structures is represented in Table 1.1 [21], in which the parameters are ε (dielectric permittivity), μ (magnetic permeability), ρ (mass density) and c_T, c_L (sound velocity, transverse or longitudinal).

Table 1.1. Comparison of Properties of Photonic and Phononic Crystals.

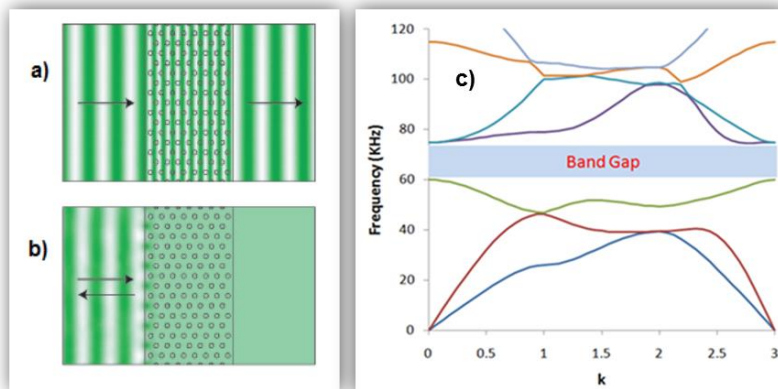| Property	Photonic Crystal	Phononic Crystal
Materials	Made from atleast two dielectric materials	Made from at least two elastic materials
Key Parameters	ε, μ	ρ, c_T, c_L
Particle	Photon	Phonon
Wave	Electromagnetic	Vibrations/sound
Polarization	Transverse	Coupled (transverse and longitudinal)

In recent years, scientific research has focused on the elucidation of band structure and propagation of elastic waves in phononic crystals. These periodic materials show unique properties (e.g. negative refraction) which can be manipulated for applied research apart from being of interest in fundamental science. [22, 23] In 1946, Brillouin exploited the concept of wave propagation in periodic structures [24]. Owing to a similarity in concept of photonic and phononic crystals and the extensive scientific research focused on photonics in recent times, acoustic meta-materials and phononic structures have sparked a lot of scientific activity only in the last 20 years. The term "phononic" indicates that the excitations in these periodic structures concern "phonons" or vibrational waves. These mechanical waves can be transverse or longitudinal, in divergence with the scalar electron waves or transverse electromagnetic waves.

1.3. The Phononic Band Gap

Sound waves travelling through a medium can be taken as elastic waves propagating through small masses connected by springs. As phononic structures are made up of alternating materials

having an impedance contrast, the travelling sound waves will experience fluctuating phase velocity i.e. decreased phase velocity in the low impedance layers and vice versa. [25] The interference and scattering of acoustic or elastic waves in a phononic crystal lattice give rise to a "band gap". This is quite in line with the Bragg scattering when the periodic dimensions of the phononic lattice (*lattice parameter, a*) is comparable to the wavelength (λ) of the propagating sound wave. For a band gap to arise in a phononic crystal, constructive interference (*path difference of the interfering waves = nλ, where n is an integer*) must take place between incident and scattered secondary waves reflected from each interface of the periodic lattice. The outcome of such a scenario is a "band gap" or stop-band where propagation of that specific frequency wave is forbidden. On the other hand, destructive interference allows transmission through the crystal lattice, leading to "propagation bands".

Figure 1.3. *Depiction of a phononic band gap (a) shows propagation bands through a phononic crystal acting as an acoustic conductor while (b) shows a stop band where the incoming elastic wave is not allowed to travel, making the phononic crystal an acoustic insulator for waves of this specific frequency [27] (c) gives the phonon dispersion diagram showing a bang gap between 60-80 kHz.*

Band gap engineering refers to manipulating the width and center of frequency of the phononic band gap by changing various parameters. The width of the band gap strongly depends on the acoustic impedance (Z) contrast and reflectivity (R), [26]

$$Z = c\rho \tag{1.1}$$

$$R = \left[\frac{Z_2 - Z_1}{Z_2 + Z_1} \right]^2 \tag{1.2}$$

Where c and ρ are the sound velocity and density of each independent individual constituent in the phononic crystal, respectively. The elastic waves are reflected back for $R = 1$; if $R < 1$, the waves propagate through the medium. As is evident from (1.2), the greater the elastic impedance contrast more will be the reflectivity of the incident elastic wave from the interface. As a result, the width of the band gap increases for a phononic crystal that is composed of materials with largely varying acoustic impedances. In addition, an important parameter to tailor the band gap is by changing the filling ratio or volume fraction of each constituent in the phononic lattice. [28] Tailoring of the frequency of the band gap also depends strongly on the lattice spacing, a (see equation 1.3).

$$\omega \sim \frac{1}{\lambda} \sim \frac{1}{a} \tag{1.3}$$

It is important to note here that the wave functions of an elastic wave travelling through periodic superlattices is different from those of a plane wave by a factor representing periodicity, according to the Bloch theorem. [29] Phononic band gaps can be either *complete* or *partial*, depending upon if they restrict propagation of elastic waves along all directions or a specific direction, respectively.

In recent years, research in the field of phononics has been focused on the theoretical and experimental determination of the phononic band gap [30-32], with 2D and 3D materials remaining the choice of most scientists. The presence of the longitudinal mode of vibration makes elucidation of the acoustical band spectrum much more complex than the photonic crystals. A comprehensive review on two-dimensional phononic crystals by Pennec et al., details the theory, examples and applications of solid-solid, fluid-fluid and solid-fluid phononic crystals. [33] To date, the experimental research has largely concentrated on sonic (*20 Hz - 20 kHz*) [34] and

ultrasonic (*20 kHz – 1 GHz*) [35] phononics corresponding to wavelengths ranging from meters to centimeters to millimeters. However, hypersonic phononic crystals *(> 1 GHz)* have gained in popularity recently, as they can make prime use of nanostructures and new fabrication methods.

1.4. Hypersonic Phononic Crystals

Phononic structures on a length scale of sub micrometer or nanometer have band gaps in the frequency range of Gigahertz (GHz) (*1-100 GHz*); such materials are called hypersonic phononic crystals. The exciting part about hypersonic phononic materials is their ability to interact with light, paving the way to the field of acousto-optics. [27] As the structures become smaller and smaller, we enter the range of wavelengths of visible and infra-red light. This not only gives us a prospect of coupling interactions between photons and phonons but it also leads us to understanding the phenomenon of thermal management. [36] The applications of phononic crystals in these two areas are extensive, ranging from heat control at the nano-scale to photonic-phononic waveguides. [37]

Several experimental realizations of hypersonic band gaps in 2D and 3D systems have been investigated. [38, 39] Cheng et al reported a hypersonic band gap in colloidal crystals of aqueous poly styrene after a novel fabrication process. [40] In 2010, Sato et al described their study on engineering the hypersonic band gap in polymer nanocomposites of anodic aluminum oxide and poly (vinylidene diflouride). [41] However, there have been few attempts to develop one-dimensional functional nanomaterials with a phononic band gap facilitating hypersound propagation despite potential applications and ease of fabrication. A one-dimensional polymer nanostructure was investigated by Walker et al [17] describing elastic wave propagation through these phononic materials without losing their coherence. Periodically structured polymer multilayers of poly carbonate and poly (methyl methacrylate) have also been examined in detail to understand phonon dispersion. [42]

1.5. Applications of Phononic Crystals

Phononic crystals offer a way to modify and manipulate the propagation of acoustic waves in periodic materials. The applications are extensive depending upon the frequency of operation (Figure 1.4). The increasing interest and the subsequent research in the field of phononics has led to the development of acoustic resonators, sound filters, acoustic lenses, etc. [43] It is possible to produce waveguides [44] by introducing defects in a phononic crystal, leaving the propagating elastic waves no other option than to travel the path defined by the defects. Acoustic diodes use the concept of phononic materials to allow elastic wave propagation in one direction and ban it from the other, in analogy with the electric diodes. [45]
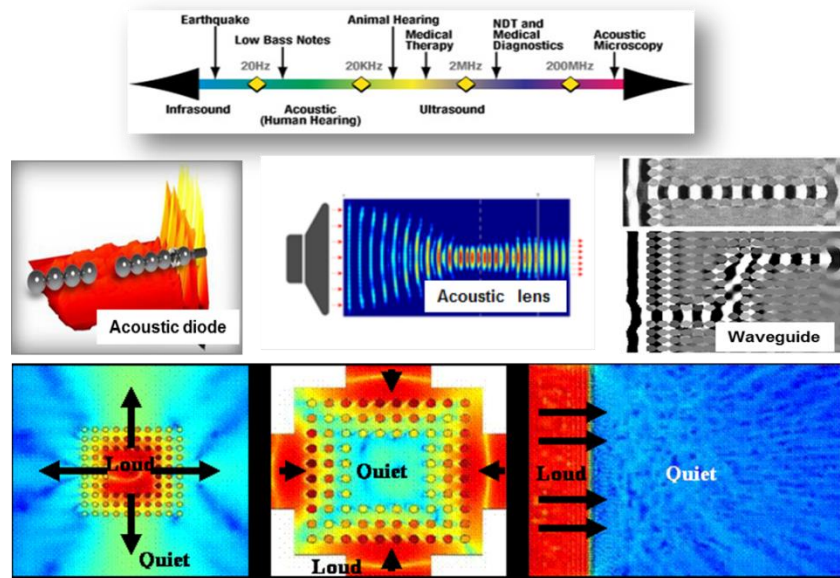

Figure 1.4. Some applications of phononic crystals [43, 45]

Manipulating propagation of elastic waves in hypersonic phononic crystals has led to more advanced applied devices. Phononic structures can be engineered to manage heat flow and charge carrier mobility by controlling the propagation of high energy phonons through periodic materials. [26, 46] The thermal conductivity of many semi-conducting materials depends largely on phonons as carriers, in contrast to the electronic carriers in metals. It is, therefore, possible to use

hypersonic phononic materials as a means to reduce the flow of phonons through a medium and consequently reduce the heat conductivity. [36]

Owing to the small dimensions of hypersonic phononic materials that go down to the nano-scale, the interaction of phonons with photons becomes a distinct possibility. The acousto-optic interactions have been modulated in opto-crystals by confining photons and phonons in the same region. [47] Such materials showing a dual band gap (photonic and phononic) are called Phoxonic Crystals. Examples of phoxonic cavities are known which show localization of sound and light and also allow coupling between them. [48] This not only makes the underlying physics of hypersonic phononic crystals interesting but also applicable in cutting edge acousto-optic devices. Simultaneous control of electromagnetic and elastic waves could also be instrumental in sensor applications, as recently theoretically predicted by Lucklum et al. [49] Functional materials can therefore be fabricated by using phononic crystals having a band gap in the gigahertz range of frequency.

1.6. Fabrication Methods

The usual phononic structure consists of periodic scattering centers of component *A* incorporated in a matrix of component *B*, where both the components have a large acoustic impedance contrast. These macro and micro-fabrication techniques work well for sonic and ultrasonic phononic crystals. In most reported cases of phononic crystals, conventional fabrication techniques have been used or structures have been manually assembled. [38, 50] However, when it comes to hypersonic phononic crystals, it is necessary to go down to nanostructures which could effectively allow band gaps in the Gigahertz frequency range. Two dimensional hexagonal arrays of porous alumina have been investigated to control the hypersound propagation. [51] Such nanostructures provide a facile platform of engineering the phononic band gap by varying the porosity, size and filling of the nanopores.

Colloidal nanoparticles are a viable option in intelligent functional materials that provide opportunities of variation of elastic properties, directly impacting the phononic band diagram. There have been instances where core-shell spheres of PMMA-silica were studied to investigate the effect of particle shape and size on the mechanical properties of the hybrids. The difference between the bulk and nanoscale properties of such architectures is shown by the different elastic

moduli after a study of vibrational excitations. [52] Self-assembly has also been a way to obtain a periodic arrangement of colloidal nanospheres of polystyrene on a glass substrate. [40] These vertical deposition techniques, however lead to the presence of some structural defects, which have the ability to significantly affect the phononic band gap. The colloidal assemblies are usually held together by van der Waal forces of interaction. The acoustic properties of self-assembled block copolymers have also been studied. The phonon energy flow can be directed by modifying the process of self-assembly. [53] A precise control over fabrication of phononic structures is, therefore highly desirable.

Compared to the hand-assembled or machined phononic crystal structures, the micro-fabricated techniques are less time consuming. Nanofabrication methods are, however less costly, reproducible, easy and effective. The use of mature technologies brings in simplicity in the fabrication process. Interference lithography is one such technique that has been used to produce 1D, 2D and 3D periodic structures by employing coherent light beams. Three dimensional poly (dimethylsiloxane)/ air elastomers have been fabricated by multi-beam interference lithography to mechanically tune the phononic band diagram. [54] Lithography provides control over geometry to generate large area periodic patterns. Although it is fast, the method is still incapable of producing arbitary phononic structures and involves a complex optical setup. [55]

Layer-by-layer fabrication process is a soft technique of producing nanostructures on a large area with low cost and precise structural control. In one additive approach, a patterned structure can simply be put on top of another and so on, to obtain an assembled periodic structure. [56] Multilayered polymer films of poly (methyl methacrylate) (PMMA) and poly (ethylteraphthalate) (PET) stacked in one direction have been investigated to determine the phonon dispersion through such structures. [42] Walker et al studied the coherence of propagating elastic waves in a multilayered phononic structure of poly (vinyl pyrolidone) (PVP) and poly (styrene). [17] The methods employed to produce phononic structures through a layer-by-layer assembly include soft lithography, spin-coating and anodization. [57] The one important factor to consider while designing phononic structures is the direct effect of structure on the phononic band diagram. Due to the limitations in many fabrication techniques, one of the approaches is to use these methods in conjunction with each other to obtain the desired effects.

Bibliography

1. R. Feynman, *Science.* **1991**, *254*, 1300.

2. B. Bhushan, *Springer handbook of Nanotechnology*; Springer E-books: **2010**

3. K. W. C. Lai and N. Xi, *Nano Optoelectronic Sensor and Devices*; Elsevier: Oxford **2012**.

4. S. K. Vashist, A. G. Venkatesh, K. Mitsakakis, G. Czilwik, G. Roth, F. Stetten and R. Zengerle, *BioNanoSci.* **2012**, 2, 115.

5. H. Shao, C. Min, D. Issadore, M. Liong, T. Yoon, R. Weissleder and H. Lee, *Theranostics*. **2012**, 2, 55.

6. M. Arruebo, R. F. Pacheco, M. R. Ibarra and J. Santamaria, *Nanotoday*. **2007**, 2, 22.

7. S. C. McBain, H. HP. Yiu and J. Dobson, *Int. J. Nanomedicine*. **2008**, 3, 169.

8. E. Serranoa, G. Rus and J. G. Martinez, *Renewable and Sustainable Energy Reviews.* **2009**, 13, 2373.

9. R. Mout, D. F. Moyano, S. Rana and V. M. Rotello, *Chem. Soc. Rev*. **2012**, 41, 2539.

10. J. Rhoa, L, Kuhn-Spearing and P. Zioupos, *Medical Engg & Phys*. **1998**, 20, 92.

11. J. Aizenberg, J. C. Weaver, M. S. Thanawala, V. C. Sundar, D. E. Morse and P. Fratzl, *Science*. **2005**, 309, 275.

12. K. Zhang, H. Duana, B. L. Karihaloo and J. Wang, *PNAS*. **2010**, 107, 9502.

13. F. Natalio, T. P. Corrales, M. Panthöfer, D. Schollmeyer, I. Liberewirth, W. E. G. Müller, M. Kappl, H. Butt and W. Tremel, *Science*. **2013**, 339, 1298.

14. L. J. Bonderer, A. R. Studart and L. J. Gauckler, *Science*. **2008**, 319, 1069.

15. A. Sellinger, P. M. Weiss, A. Nguyen, Y. Lu, R. A. Assink, W. Gong and C. J. Brinker, *Nature*. **1998**, 394, 256.

16. J. Xie, H. Deng, Z. Q. Xu, Y. Li and J. Huang, *J. Crystal Growth*. **2006**, 292, 227.

17. P. M. Walker, J. S. Sharp, A. V. Akimov and A. J. Kent, *App. Phys. Letters*. **2010**, 97, 073106

18. A. N. Shipway, E. Katz and I. Willner, *Chem Phys Chem*. **2000**, 1, 18.

19. P. Judeinstein and C. Sanchez, *J. Mater. Chem.* **1996**, 6, 511.

20. V. Romero-Garcia, J. V. Sanchez-Perez, S. Castineira-Ibanez and L. M. Garcia-Raffi, *App. Phys. Lett*. **2010**, 96, 124102.

21. M. S. Kushwaha, P. Haievi, L. Dobrzynski and B. Djfari-Rouhani, *Phys. Rev. Lett*. **1993**, 71, 2022.

22. M. Sigalas, M. D. Kushwaha, E. N. Economou, M. Kafesaki, I. E. Psarabos and W. Steurer, *Z. Kristallorg*. **2005**, 220, 765.

23. X. Zhang and Z. Liu, *App. Phys. Lett*. **2004**, 85, 341.

24. L. Brillouin, *Wave Propagation in Periodic Structures;* McGraw-Hill: New York, **1946**.

25. E. A. Rietman and J. M. Glynn, *Band-Gap Engineering of Phononic Crystals: A Computational Survey of Two-Dimensional Systems;* Physical Sciences Inc; Massachusetts, **2007**.

26. T. Gorishnyy, *Hypersonic Phononic Crystals*; PhD Thesis, Department of Materials Science and Engineering, MIT, **2007**.

27. E. L. Thomas, T. Gorishnyy and M. Maldovan, *Nature Mat*. **2006**, 5, 773.

28. M. Lu, L. Feng and Y. Chen, *Materials Today*. **2009**, 12, 34.

29. C. Kittel, *Introduction to Solid State Physics*; John Wiley & Sons: New York, **1996**.

30. J. O. Vasseur, B. Djafari-Rouhani, L. Dobrzynski, M. S. Khushwaha and P. Halevi, *Phys. Condens. Matter*. **1994**, 6, 8759.

31. M. M. Sigalas and E. N. Economou, *J. Sound & Vib*. **1992**, 158, 377.

32. R. C. Norris, J. S. Hamel and P. Nadeau, *J. Appl. Phys*. **2008**, 103, 104908.

33. Y. Pennec, J. O. Vasseur, B. Djafari-Rouhani, L. Dobryzynski and P. A. Deymier, *Surf. Sci. Rep*. **2010**, 65, 229.

34. Z. Liu, X. Zhang, Y. Mao, Y. Y, Zhu, Z. Yang, C. T. Chan and P. Sheng, *Science.* **2000**, 289, 1734.

35. S. Yang, J. H. Page, Z. Li, M. L. Cowan, C. T. Chan and P. Sheng, *Phys. Rev. Lett*. **2002**, 88, 104301.

36. T. Gorishnyy, M. Maldovan, C. Ullal and E. Thomas, *Sound ideas; Phys. World.* **2005**, 18, 24.

37. H. Shin, W. Qiu, R. Jarecki, J. A. Cox, R. H. Olsson III, A. Starbuck, Z. Wang and P. T. Rakich, *Nature. Comm*. **2013**, 4, 1.

38. T. Gorishnyy, J. H. Jang, C. Koh and E. L. Thomas, *Appl. Phys. Lett*. **2007**, 91, 121915.

39. A. S. Salasyuk, A. V. Scherbakov, D. R. Yakovlev, A. V. Akimov, A. A. Kaplyanskii, S. F. Kaplna, S. A. Grudinkin, A. V. Nashchekin, A. B. Pevtsov, V. G. Golubev, T. Berstermann, C. Brüggemann, M. Bombeck and M. Bayer, *Nano. Lett*. **2010**, 10, 1319.

40. W. Cheng, J. Wang, U. Jonas, G. Fytas and N. Stefanou, *Nature Mat*. **2006**, 5, 830.

41. A. Sato, Y. Pennec, N. Shingne, T. Thurn-Albrecht, W. Knoll, M. Steinhart, B. Djafari-Rouhani and G. Fytas, *ACS Nano*. **2010**, 4, 3471.

42. W. Cheng, N. Gomopoulos, G. Fytas, T. Gorishnyy, J. Walish, E. L. Thomas, A. Hiltner and E. Baer, *Nano Lett*. **2008**, 8, 1423.

43. S. S. Lin and T. J. Huang, *Phys. Rev. B*. **2009**, 79, 094302.

44. A. Khelif, A. Choujaa, S. Benchabane, B. Djafari-Rouhani and V. Laude, *Appl. Phys. Lett*. **2004**, 84, 4400.

45. B. Li, *Nature Mater*. **2010**, 9, 962.

46. A. N. Cleland, D. R. Schmidt and C. S. Yung, *Phys. Rev. Lett*. **2005**, 94, 115501.

47. M. Eichenfield, J. Chan, R. M. Camacho, K. J. Vahala and O. Painter, *Nature*. **2009**, 462, 78.

48. N. Papanikolaou, I. E. Psarobas, N. Stefanou, B. Djafari-Rouhani, B. Bonello and V. Laude, *Microelectronic Engg*. **2012**, 90, 155.

49. R. Lucklum, M. Zubtsov and A. Oseev, *Anal Bioanal Chem*. **2013**, 405, 6497.

50. T. Still, G. Gantzounis, D. Kiefer, G. Hellmann, R. Sainidou, G. Fytas and N. Stefanou, *Phys. Rev. Lett*. **2011**, 106, 175505.

51. A. Sato, Y. Pennec, T. Yanagishita, H. Masuda, W. Knoll, V. Djafari-Rouhani and G. Fytas, *New. J. Phys*. **2012**, 14, 113032.

52. T. Still, R. Sainidou, M. Retsch, U. Jonas, P. Spahn, G. P. Hellmann and G. Fytas, *Nano Lett*. **2008**, 8, 3194.

53. A. M. Urbas, E. L. Thomas, H. Kriegs, G. Fytas, R. S. Penciu and L. N. Economou, *Phys. Rev. Lett*. **2003**, 90, 108302-1.

54. J. Jang, C. K. Ullal, T. Gorishnyy, V. V. Tsukruk and E.L. Thomas, *Nano Lett*. **2006**, 6, 740.

55. J. Jang, C. K. Ullal, M. Maldovan, T. Gorishnyy, S. Kooi, C. Y. Koh and E. L. Thomas, *Adv. Func. Mater*. **2007**, 17, 3027.

56. J. Lee, J. P. Singer and E. L. Thomas, *Adv. Mater*. **2012**, 24, 4782.

57. L. C. Parsons and G. T. Andrews, *J. Appl. Phys*. **2012**, 111, 123521.

2

Fabrication and Methods

In the first section, this chapter contains details of the fabrication methods employed in the production of one-dimensional Bragg stacks. Since the phonon propagation and the subsequently emerging band spectrum is heavily reliant on the structure of the phononic superlattices, it is necessary to look into the state-of-art fabrication in detail. In the second section, the basic principles of Brillouin light spectroscopy (*BLS*) are explained. BLS is the primary analytical method to obtain and characterize the one-dimensional phononic Bragg stacks.

2.1. Tunable Hybrid Bragg Stacks

An integral synthetic approach is necessary to design nanostructures showing a phononic band gap in hypersonic frequencies. As described in section 1.1.1, Bragg stacks define a superlattice made up of an alternating sequence of layers of two or more materials. The materials constituting such a periodic stack should have a contrast in density, sound velocity or acoustic impedance to be eligible of becoming a phononic superlattice. The stack could be made up of "solid-solid" or "solid-fluid" layers. [1] This approach of constructing phononic structures is different from the traditional macro and micro-fabrication techniques and therefore, the nanostructures discussed in this work obtained from this fabrication process fall in the category of "soft phononics".

The pre-dominant reason of selecting multi-layered Bragg stacks as 1D phononics to be investigated is their ease of fabrication and short time of preparation. In addition, the Bragg stacks are highly "tunable". This means that a structure can be designed as desired based on theoretical studies. It is possible to insert defect layers of same or different materials in the Bragg stack, as described in detail in Chapter 4 of this thesis. The previous examples

of tunable superlattices used for bandgap materials came from photonic crystals made up of mesoporous SiO_2, TiO_2, ZrO_2 or WO_3 nanoparticles. [2, 3] Examples of hybrid Bragg stacks are also known in which polymer layers alternate with the nanoparticle layers. [4] This arrangement ensures that an effective medium exists where the soft polymer combines with the hard inorganic nanoparticles to show a novel phononic behavior. Therefore, such a system of poly (methylmethacrylate) (*PMMA*) and porous silica (*SiO₂*) nanoparticles is chosen in this work to study elastic wave propagation. The constituent layers combine to give a periodic medium that effectively stops hypersonic elastic wave propagation in a designed range of frequency. To obtain the assembled structure, a modified method of high speed spin coating coupled with heat treatment is employed. This method of accumulation of alternate multilayers has considerable advantages over the charge-adsorption technique of layer by layer (*LbL*) or the slower dip-coating method.

2.2. Spin Coating

Spin-coating is a fast technique of obtaining homogenous thin films or multilayers on large area substrates. The method is well-known for its reproducibility and uniform structural homogeneity. The technique is widely used in making protective coatings, membranes and optical coatings. [5] During the coating process, the solution used for coating is dropped on the substrate and the substrate- mounted platform of a spin-coater rotates at user-determined high speed. Owing to the acting centrifugal force and the adhesive interactions between the substrate and the liquid at the interface, strong sheer forces arise which push off the excess liquid from the rotating disc in a radial movement. This is accompanied by evaporation of the solvent and as a result, a uniform coating of the liquid is obtained on the substrate. [6] Figure 2.1 describes a standard spin-coating procedure.
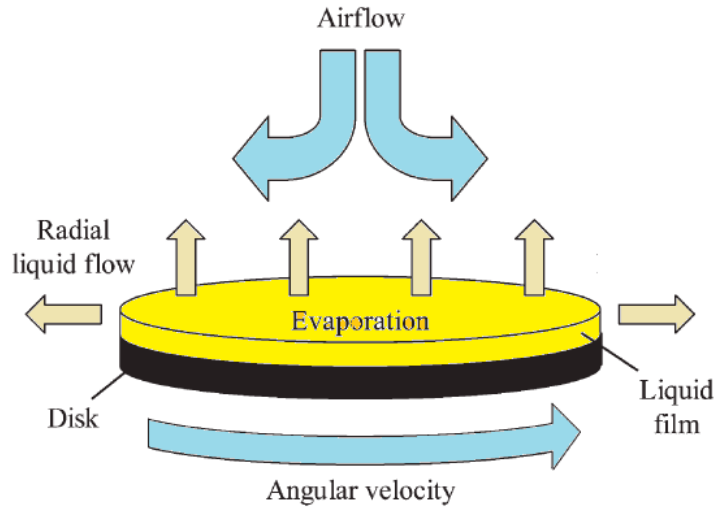
Figure 2.1. *Standard spin coating procedure*. [5]

In order to obtain homogenous thin films, some important parameters have to be taken into account. According to a mathematical model of spin coating, [6] the evaporation rate of the solvent, the concentration and viscosity of the solution play a significant role in the formation of the thin film (See equation 2.1). In addition, the thickness of the films directly depends on the rotation speed and time.

$$\frac{dh}{dt} = \frac{2\rho\omega^2 h^3}{3\eta_o} \tag{2.1}$$

Where ρ is the density of the liquid, ω is the spinning speed, h is the thickness of the film, t is the spinning time while η_o is the initial viscosity of the liquid. From the above equation, it becomes obvious that it is imperative to adjust these parameters to get a film of desired dimensions.

2.3. Preparation of Stable Precursor Solutions

Since this work is greatly affected by the physical characteristics of individual layers, a great deal of effort has been spent on optimizing the determining factors to get a periodic structure of desired dimensions. Bragg stacks should have uniform layers and smooth interfaces. In order

to achieve this end, it is necessary to have high quality, stable precursor dispersions. There is a limited concentration range that must be strictly adhered to; too much concentrated precursor solutions lead to aggregation while dilute solutions show less adhesion to the substrate. In constructing Bragg stacks, the colloidal nanoparticle dispersions must conform to the above conditions. It is particularly necessary to avoid agglomeration of nanoparticles as it causes scattering of light and dampens any prospect of having a phoxonic structure. [7]

In the present work, the system selected for studying elastic wave propagation is of poly (methyl methacrylate) (*PMMA*) and porous silica (*SiO₂*). PMMA beads used for the layers in the spin-coated stack were obtained from Acros, M_w= 35 kDa. The polymer layer was chosen due to its low modulus whereas inorganic silica nanoparticles show the higher modulus, thereby giving a strong contrast required in a phononic lattice. The polymeric stock solution was made at 10% w/v in toulene. The choice of solvent in fabricating Bragg stacks is extremely important. Orthogonal solvents are chosen for the two contrasting materials constituting the Bragg stacks so that the alternating layers are phase-separated. Miscible solvents, on the other hand, lead to the formation of a hybrid rather than a multilayered stack.

The silica dispersion used as precursor is the commercially available LUDOX AS-30 colloidal silica by Aldrich, which is a 30 % wt suspension of nanoparticles in water, stabilized by ammonium counter ions. However, for the spin coating of Bragg stacks, addition of surfactant to the stock solution is necessary to ensure smooth and easy formation of a thin film. For this purpose, sodium dodecyl sulphate (*SDS*) is chosen to reduce the high surface tension of the silica dispersion. SDS is primarily selected because an anionic surfactant stable under alkaline conditions is required, since the nanoparticles are stable in basic medium. Therefore, a stock solution of SDS, 10 % *w/v* was made in water and 0.1 % (1000 ppm) SDS solution was added to the commercial silica dispersion prior to spin coating. 14% ammonium hydroxide solution (*NH₄OH*) was also added to provide the alkaline medium.

However, the concentration of silica used for the preparation of the precursor solution depends on the desired thickness of the film in the Bragg stack. In the standard *PMMA/SiO₂* Bragg stack of ten bilayers, every layer is designed to have a thickness of 50 nm. For this purpose, ellipsometric measurements were carried out to determine the dependence of thickness of the SiO₂ layer on the

concentration of silica solution (Appendix: Section 8.1). Controlling the thickness of the individual layers in a Bragg stack is highly desirable as it directly affects the band gap in phononic lattice. After a careful optimization of all relevant parameters, it was found that a SiO_2 layer of 50 nm can be obtained by spin-coating a precursor solution comprising 3.4 % LUDOX AS-30 silica colloidal particles and 1000 ppm SDS in 14 % ammonium hydroxide. The details can be found in supplementary section.

In a similar way, the thickness of the PMMA layer was carefully controlled to 50 nm. For this purpose, a range of concentrated polymer solutions in toulene (from 2 – 6 %) *w/v* were spin-coated on silicon wafers and the resulting PMMA films were analyzed for thickness. [7] From a linear progression curve of

$$h_{(PMMA)} = 39.2 + 40.5\, c_{(PMMA)} \tag{2.2}$$

it was determined that a 2.2 % (*w/v*) PMMA solution in toulene was required to produce a film of 50 nm thickness. Equation 2.2 can also be used to coat polymer films of greater thickness if needed, as in the case of defect layers discussed in chapter 4 of this thesis.

2.4. Fabrication of Hybrid Bragg Stacks

The first challenge in the fabrication of hybrid Bragg stacks with a view of studying phonon propagation is the experimental difficulty of controlling the thickness of each layer in the superlattice to a definite length scale. A careful optimization has been done beforehand to ensure the concentration of PMMA and silica nanoparticles that will give a desired thickness (for example 50 nm in the standard superlattice) for a given set of spin coating parameters. Temperature and humidity factors were taken into account and spin-coating was always carried out in a clean environment. Despite all these precautionary measures, small variations in thickness and surface roughness can occur. However, all the experimental errors in this work fell well within the range of the BLS experimental resolution and did not affect the band diagram by any considerable factor.

The Bragg stacks are coated on microscopic glass slides with a size of 2 x 2 cm. The substrate must be free of dust particles or other impurities to ensure smooth film deposition. Otherwise, comets or striations are observed on the surface of the coated films and serves as defects in a superlattice. *Comets* occur due to the presence of bigger particles or agglomerates in the solution used for spin coating. One of the common spin coating defect is the appearance of *streaks* due to presence of impurities on the surface of substrate before coating. This can be avoided by working in clean conditions. *Striations*, on the other hand, are radial patterns on a substrate that arise out of unbalanced surface tension changes due to evaporation of the solvent. [8]

Comets   Striations   Air bubbles   Incomplete coating
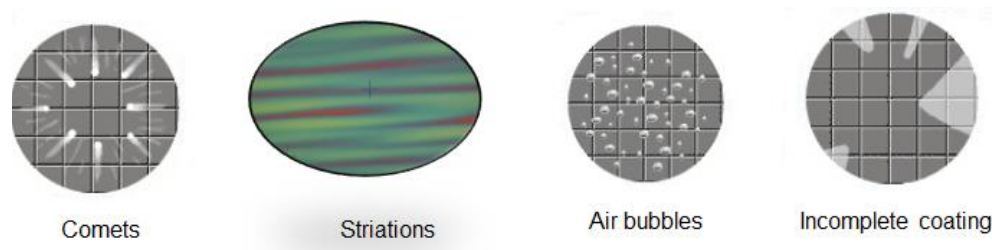
Figure 2.2. Common spin coating defects

To avoid the formation of defects and ensure a smoothly coated film in this work, the substrates are pre-cleaned in a piranha solution (2:1, *v/v*) of concentrated sulphuric acid (Aldrich) and 30 % hydrogen peroxide (Acros). After cleaning for about 45 min, the substrates are washed repeatedly by de-ionized water and ethanol (Carl Roth). Subsequently, a stream of nitrogen gas is used to dry the substrates and heat treatment is carried out in a furnace at 450 ˚C for 15 minutes. This process removes organic residues from the substrate, necessary for a smooth coating without defects. The sintering step also helps hydrolyzing the surface of the substrate.

The Bragg stacks are coated on the pre-cleaned substrate starting from the PMMA layer. The substrate is first exposed to a nitrogen stream to get rid of any dust particles. A 0.2 µm PTFE syringe filter was used for casting the solutions on the substrate for spin coating. Afterwards, as described in section 2.3, the coating is carried out from a 2.2 % PMMA solution in toluene and 3.4 % silica dispersion in water containing 0.1 % SDS and 14 % ammonium hydroxide. The

optimized concentrations give a layer thickness of 50 nm for each PMMA and SiO_2 layer. A detailed schematic of the fabrication process is given in Figure 2.3.
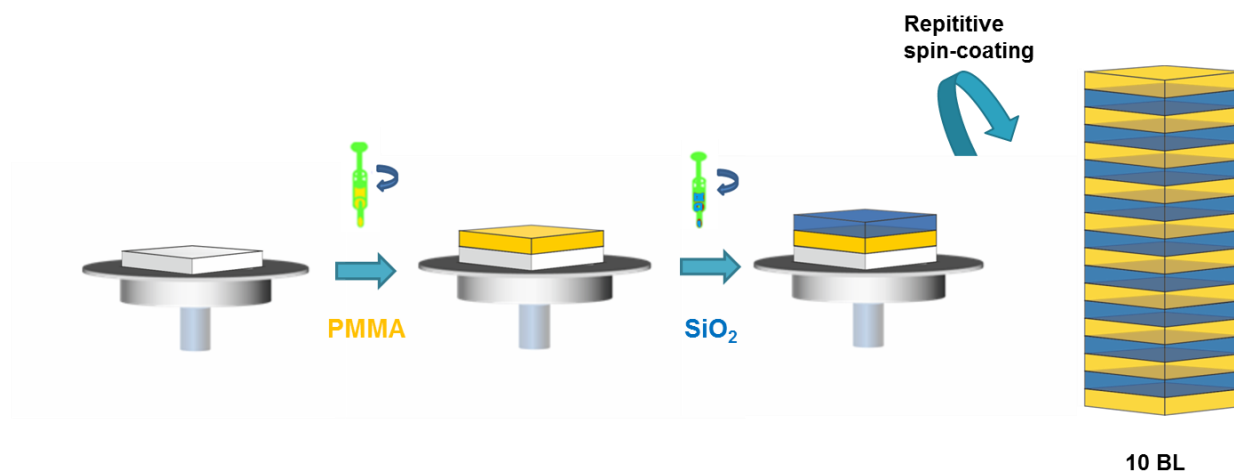
Figure 2.3. *Schematic representation of the fabrication process of PMMA/SiO₂ hybrid Bragg stacks consisting of ten bilayers (BL).*

Spin coating was carried out on a Laurell WS-400-6NPP-LITE instument, with the following fixed parameters.

Speed: 5000 rpm

Acceleration: 5040 rpm/s

Time: 20 s

Subsequent to each coating, the substrate was subjected to a heat treatment at 105 ˚C for 15 min. This ensures that all the additional solvent has evaporated from the superlattice and the coating is

cemented. This is a necessary step to obtain smooth interfaces between multilayers. The ten-bilayer Bragg stacks of PMMA/SiO$_2$ are characterized by Scanning Electron Microscopy (SEM) images to confirm the periodicity of the lattice (shown in Figure 2.4).

1 µm
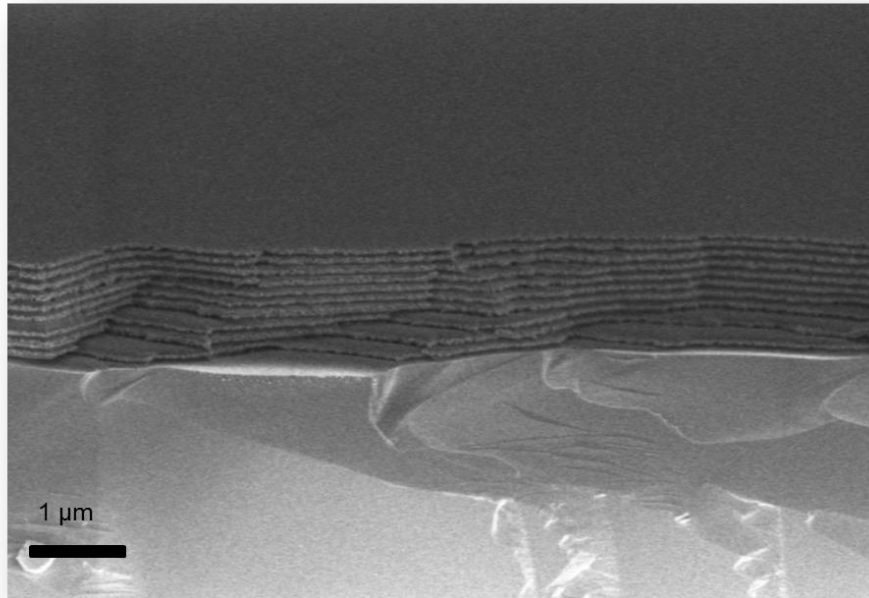
Figure 2.4. *Scanning Electron Microscope (SEM) image of 10 bilayers of PMMA/SiO$_2$ Bragg stack fabricated by repetitive high speed spin-coating. The period is well reproduced throughout and the structure is uniform on the whole length of the substrate.*

A recurring feature during the fabrication of the *PMMA/SiO$_2$* Bragg stack is the coloration which appears on coating successive bilayers when the multilayers are built on silicon wafer. Structural color is an important feature of multilayers that comes from different reasons, a prominent one being interference of light due to periodic nanostructure. [9] This phenomenon is noticeable in nature in different animals, for instance in peacock feathers and butterfly wings. [10] The idea of tunable structural colors features prominently in most recent research on 1D photonic crystals. [11, 12]

During the course of fabrication in this work, it was observed that the color of the film deposited on silicon wafer changes as more bilayers are added. However, no Bragg reflection peak was observed indicating a photonic band gap, for the 10 BL standard supperlattice of PMMA and silica due to the small refractive index contrast. Small radial variations in color are noted at the edge of the silicon substrate due to the intrinsic Marangoni effect in spin coating which is unavoidable. [13]

2.5. Brillouin Light Scattering (BLS)

The phononic superlattices of PMMA/SiO$_2$ with different lattice spacings (details in Chapter 3) are characterized for phonon propagation by Brillouin Light Scattering (*BLS*). BLS is a non-destructive and non-contact technique which provides experimental measurement of a phononic band gap along with a systematic evaluation of several other parameters affecting phonon propagation in periodic media. The working principle of Brillouin light scattering is based on photo-elastic interaction between the incident photons from a single-frequency laser and time-dependent density variations (phonons, in the present case) in the sample medium that have been thermally excited. [14] Since the scattering is inelastic, the incident photon gives way to a scattered photon of lower energy and a phonon is created (*Stokes process*). Alternatively, a phonon can be annihilated and the photon can gain energy (*Anti-Stokes process*). The difference in frequency of the incident and scattered photons is then equal to the frequency of the phonon. The frequency shift is terned as the Brillouin shift (*Δf*) after L. Brillouin, [15] who first discussed light scattering by thermal phonons. Coupled with the Bragg's law, this Doppler shift can be determined by the experimental scattering geometry. The classical theory of light scattering in condensed matter is applied to the Brillouin scattering by phonons in this work in which the phonons are considered to have wavelengths in the range of nanometers [16] The details are provided in Section 8.2 of Appendix.

The scattering geometry determines the direction of propagation of the elastic waves and is defined by the wave vectors of the scattered and incident photons, given by k_s and k_i respectively. If q is the scattering wave vector of the phonon and θ is the scattering angle, the scattering plane

can be defined by different geometries. A simple schematic showing the relation of the wave vectors is given in Figure 2.5.
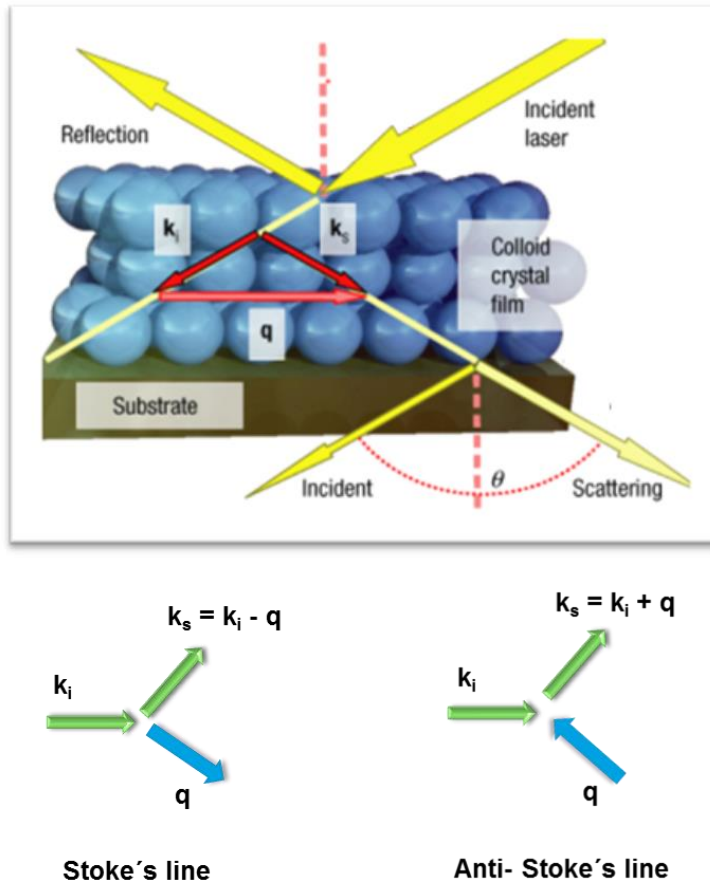
Figure 2.5. *Inelastic light scattering in a colloidal crystal film. The wavevectors of the incident and scattered light are clearly shown.* [17] *The Stokes and anti-Stokes process relate to the creation and annihilation of a phonon, respectively.*

The wave vectors k_s and k_i of the scattered and incident photons define the scattering plane and are related to the scattering wave vector q by the equation 2.3.

$$q = k_s - k_i \tag{2.3}$$

Two scattering geometries are of considerable relevance to the present work, differing in the direction of propagating phonons in the medium. If the wave vector q is parallel to the layers ($q = q_{\parallel}$) as in the transmission mode, its magnitude is independent of the refractive index n of the medium and is given by equation 2.4.

$$q_{\parallel} = q = \frac{4\pi}{\lambda} \sin \frac{\theta}{2} \tag{2.4}$$

However, in the case of perpendicular propagation of light along the direction of periodicity of the Bragg stack, the wave vector q is normal to the film surface ($q = q_{\perp}$). In the reflection geometry, the scattering wave vector relies on the refractive index of the medium, [14] as shown in equation 2.5 and out of plane phonon excitations are considered. The dispersion relation and the phononic band gap are obtained from this scattering geometry at the Bragg

$$q = \frac{4n\pi}{\lambda} \sin \frac{\theta}{2} \tag{2.5}$$

In the BLS set up, the incident laser beam is reflected many times and undergoes interference at the detector. In the event of constructive interference, maximum reflection takes place and the case is represented by the equation, [16]

$$\lambda = 2na \sin \frac{\theta}{2} \tag{2.6}$$

Here, a is the periodicity in the multi-layered Bragg stack. Comparing equations (2.5) and (2.6) for the value of λ, the magnitude of q is obtained as

$$q = \frac{2\pi}{a} \tag{2.7}$$

The value of q depends on the scattering angle θ. During the course of BLS measurements, q is varied by manipulating the angle of scattering and the spectrum is recorded. In case of homogenous systems, the law of conservation of momentum holds that q is equal to k whereas q involves an additional term for lattice reciprocal vector G for periodic systems. [18] The Doppler shift that occurs during Brillouin light scattering is measured in terms of angular frequency (equation 2.8), leading to doublets in the BLS spectra corresponding to the Stokes and anti-Stokes processes.

$$\omega = \omega_s - \omega_i = \pm\, c\, k \tag{2.8}$$

Brillouin light scattering proves itself as a sensitive characterization technique provided the periodic lattice spacing is comparable to the phonon wavelength ($2\pi/q$). The PMMA /SiO$_2$ stacks studied in this work fulfill these criteria, with a lattice spacing of around 100 nm. This enables us to study the elastic behavior of these hybrid nano-structures and determine parameters like elastic modulus, mass density of materials, etc.

2.5.1. BLS Instrumental Setup

Hypersonic phononic crystals can easily be analyzed with a specially designed Brillouin Spectrometer which makes use of tandem Fabry- Perot interferometer (FP) to achieve the high resolution required to detect the small frequency shifts. Spectrometers using diffraction gratings fail in this regard as the BLS peaks lie quite close to the high intensity peak of elastic Rayleigh scattering. [19] The scattered light is analyzed in the BLS instrument by using a designed combination of monochromatic laser source (532 nm, in this case), a focusing mechanism and a Fabry-Perot interferometer for spectral resolution. Lasers with narrow spectral width prove an instrumental role in resolving the small frequency shifts. [20] A FP interferometer makes use of two highly reflecting plane surfaces which are parallel to each other and separated by an adjustable distance d. High resolution is achieved by changing the distance between the two mirrors and thereby studying transmission of light at different wavelengths. [21] A schematic of the BLS set up is shown in Figure 2.6. In this work, a six-pass tandem FP interferometer was used.

For effective dispersion measurements, it is necessary to use an arrangement where the scattering angle can be varied as this gives access to more phonon wave vectors. It is also possible to use a rotation stage to change the orientation of the sample with respect to the incoming incident light beam. This latter point is critical in the case of experiments described in Chapter 3 for measuring phonon dispersion relations in-plane, out of plane and at oblique incidence.
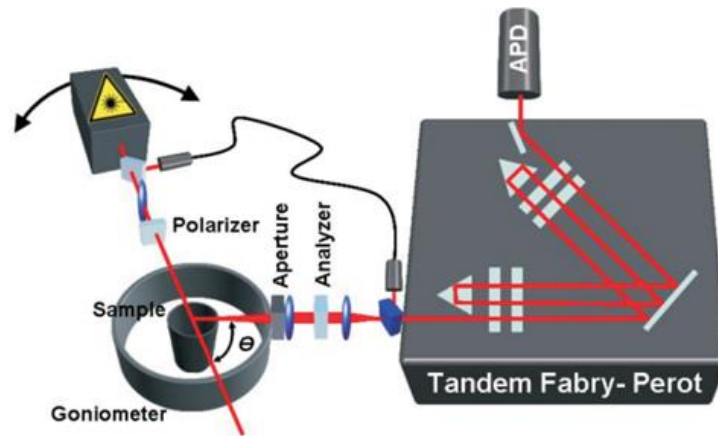
Figure 2.6. *Instrumental set up of BLS. Monochromatic laser beam is incident on the sample and a rotating platform allows variation of scattering angle θ. The scattered light is resolved by a six-pass Tandem Fabry-Perot interferometer.* [21]

During the course of this work, most of the measurements were carried out in the transmission geometry to eliminate the effect of the refractive index of the sample on the wave vector of the phonon. Further experimental details of the instrumental set up are available in the thesis of N. Gomopoulos and T. Gorishnyy. [20, 21] In this work, the BLS measurements are carried out at room temperature with a variation in the angle of incidence from $0° - 150°$. A monochromatic Nd: YAG laser beam (150 mW at 532 nm) is used as the light source. The weak signals of Brillouin frequency shifts are separated and resolved by using a six- pass Tandem FB interferometer (JRS Scientific Instruments). The detection of transmitted light is carried out by a photo- diode (APD) and analyzed by a multi-channel analyzer.

Bibliography

1. P. A. Deymier (ed.), *Acoustic Metamaterials and Phononic Crystals*; Springer: Berlin, **2013**.

2. E. Redel, C. Huai, M. Renner, G. Freymann and G. A Ozin, *Small*. **2011**, 7, 3465.

3. J. R. C. Smirnov, M. E. Calvo and H. Miguez, *Adv. Funct. Mater*. **2013**, 23, 2805.

4. Z. Wang, J. Zhang, Z. Wang, H. Shen, J. Xie, Y. Li, L. Lin and B. Yang, *J. Mater. Chem. C*. **2013**, 1, 977.

5. K. Norman, A. Ghanbari-Siahkali and N. B. Larsen, *Ann. Rep. Prog. Chem*. **2005**, 101, 174.

6. D. B. Hall, P. Underhill and J. M. Torkelson, *Polymer Engg & Sci*. **1998**, 38, 2039.

7. D. Maschke, *A New Class of Bragg Stacks and Its Principle Application*; PhD thesis, Department of Inorganic and Analytical Chemistry, Johannes Gutenberg University of Mainz, **2010**.

8. D. P. Birnie, *Langmuir*. **2013**, 29, 9072.

9. O. Karthaus (ed.), *Biomimetics in Photonics*; Taylor & Francis: Florida, **2013**.

10. S. Kinoshita and S. Yoshioka, *ChemPhysChem*. **2005**, 6, 1442.

11. H. Wang and K. Zhang, *Sensors*. **2013**, 13, 4192.

12. G. M. Nogueira, D. Banerjee, R. E. Cohen and M. F. Rubner, *Langmuir*. **2011**, 27, 7860.

13. D. P. Birnie, *J. Mater. Res*. **2001**, 16, 1145.

14. N. Gomopoulos, D. Maschke, C. Y. Koh, E. L. Thomas, W. Tremel, H. J. Butt and G. Fytas, *Nano Lett*. **2010**, 10, 980.

15. L. Brillouin, *Annal. Phys*. **1922**, 17, 88.

16. T. Still, *High Frequency Acoustics in Colloid-Based Meso and Nanostructures by Spontaneous Brillouin Light Scattering*; Springer-Verlag: Heidelberg, **2010**.

17. W. Cheng, J. Wang, U. Jonas, G. Fytas and N. Stefanou, *Nature Mat*. **2006**, 5, 830.

18. A. Trzaskowska, S. Mielcarek and J. Sarkar, *J. App. Phys*. **2013**, 114, 134304.

19. J. Lee, J. P. Singer and E. L. Thomas, *Adv. Mater.* **2012**, 24, 4782.

20. T. Gorishnyy, *Hypersonic Phononic Crystals*; PhD Thesis, Department of Materials Science and Engineering, MIT, **2007**.

21. N. Gomopoulos, *Nanomechanical and Phononic Properties of Structured Soft Materials*; PhD Thesis, Johannes Gutenberg Universität-Mainz, **2009**.

3

1-D Hypersonic Phononic Bragg Stacks

Corresponding Publication:

Dirk Schneider, <u>Faroha Liaqat</u>, El Houssaine El Boudouti, Youssef El Hassouani, Bahram Djfari-Rouhani, Wolfgang Tremel, Hans-Jürgen Butt and George Fytas,
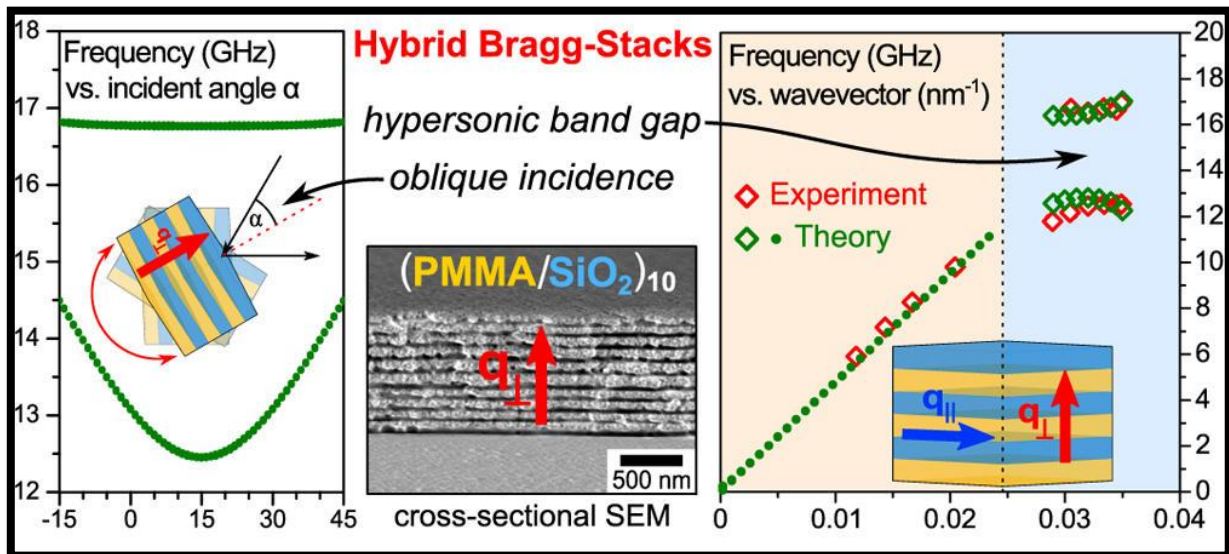
3.1. Introduction

As discussed in Chapter 1 of this thesis, phononic crystals belong to the class of meta-materials which deal with manipulation of elastic waves and their propagation in a periodic medium. Materials having a periodic modulation in mass density/modulus have frequency regions where propagation of elastic waves is forbidden and waves are decaying. Phononic crystals (*PnC*) are a promising class of composite materials that allow for systematic manipulation of elastic (acoustic) wave propagation. In simple terms, the subject deals with the creation and exploration of barriers, in this case a phononic band gap.

The mature field of Photonic Crystals (periodic variation of refractive index n) and the recently studied Phononic Crystals (variation of density ρ and longitudinal c_L and transverse c_T sound velocities) share many similarities, such as Bragg reflection and characteristic dispersion relations. However, theoretical prediction of phononic behavior becomes complicated due to a larger number of parameters associated with elastic waves. A full description of propagation of sound waves reqires vector waves. On the other hand, the band diagram of semi-conductors and photonic crystals can be simply elucidated by scalar and transverse waves, respectively.

The effort to control the elastic wave propagation in periodic structures spans a large range of frequencies; from Hz (sound waves) to THz. [1, 2] Controlling sound propagation has been an intensely studied field during the past years, ranging from architectural design to acoustic diodes, [3] and acoustic metamaterials. [4] The first observation of a phononic band gap was reported for audible frequencies in a manually made metallic sculpture in the centimeter range. [1] Phononic studies cover microstructures as well as nano-materials. Most of the research on recent years has focused on investigating phononic properties in micro-fabricated structures [5]. Recent advances in nanotechnology enable designed fabrication of periodic structures in meso-scale dimensions, thereby allowing an access to the corresponding frequency regions of GHz. The hypersonic phononic crystals having a band gap in the GHz region of frequency appear to be suitable candidates to study acousto-optic interactions and heat management. [6]

The need to reach high frequencies in the hypersonic (GHz) range imposes considerable demand on design and fabrication techniques because of the inherently much smaller length scale. The first phononic band gap in the hypersonic regime was experimentally observed in a three dimensional self-assembly of polymer colloids. [7] High frequency phononic structures offer the possibility of tuning and engineering the band gap for various applications, thereby underlining

the importance of controlled wave propagation. However, a complete narrative of phonon propagation in multi-dimensional periodic assemblies still remains elusive and challenging.

Few experimental techniques have been effective in describing phononic band gaps in high frequency periodic structures, a restriction that arises from the small length scale involved. Raman spectroscopy has also been used to study folded acoustic phonons in a semi-conductor superlattice. [8] Recently, Brillouin light scattering (*BLS*) and other laser photo-acoustic methods [9] have been useful in probing phonon propagation in periodic media and provide experimental evidence for the existence of a hypersonic phononic band gap. In particular, BLS provides non-destructive and non-contact measurements of acoustic wave propagation in GHz region for thin films as well as bulk. During the course of this work, BLS has been used to study hypersonic phonon propagation in 1-dimensional hybrid Bragg stacks.

One-dimensional hypersonic phononic superlattices offer relative ease of fabrication and great control over structural parameters, as compared to the 2D and 3D phononic crystals. This is a great advantage coupled with the fact that 1D phononic structures do not require extensive theoretical calculations. There have been few instances of using multi-layered periodic systems to study the physical phenomenon of Brillouin scattering by thermal phonons. [10] Other 1D systems investigated in the GHz range include multi-layers of silica-silicon with a phoxonic cavity [11], porous silicon Bragg mirrors [12, 13] and poly (styrene-b-isoprene) copolymer lamellar forming systems. [14] For 1D periodic structures, the first direct observation of a sizable normal incidence hypersonic phononic band gap was reported in periodic hybrid multilayer films. [15]

Multilayered phononic structures offer many perspectives to control the acoustic properties and phonon dispersion behavior in a number of ways. Manipulating phonon propagation in a superlattice can come either by controlling the number of layers or the thickness of each layer. As such, a hybrid Bragg stack offers many rich possibilities with regard to controlling acoustic properties. For this reason, this chapter focuses on designed hybrid nanostructures of periodic silica/poly (methyl methacrylate) (*p-SiO$_2$/ PMMA*) multilayer films. These Bragg stacks show direction-dependent elastic wave propagation and a well-defined band gap in the hypersonic region of frequency.

This chapter highlights phonon propagation in *PMMA/p-SiO₂* Bragg stacks and the robustness of the dispersion to fabrication inherent imperfections. Both elastic moduli (longitudinal and shear) and elasto-optic coefficients of the individual layers are also estimated. The work also provides the theoretical representation of the dispersion relations for normal and oblique incidence and the intensities of the two, lower and upper, phononic branches of the gap are co-related. In general, new phononic nanostructures have been designed successfully showing GHz acoustic excitations and a hypersonic band gap.

3.2. Results and Discussion

3.2.1. Preparation of 1-D Hybrid Bragg Stacks

Bragg stacks composed of ten bilayers serve as phononic structures in which PMMA and porous silica have been used as the high and low elastic modulus materials, respectively. The stacks are built up by sequential spin coating of the stock solutions of *PMMA/p-SiO₂* on a clean glass substrate, as described in sections 2.3 and 2.4 of this thesis. Each layer was subjected to heat treatment after spin coating for 15 min at 105 ˚C. To demonstrate the effect of layer spacing on the phonon dispersion, two Bragg stacks are investigated with different thicknesses of the PMMA and SiO₂ layers. Hence, the periodicity *a* (equation 3.1) is different in the two stacks A and B although each consists of 20 alternating layers of PMMA and p-SiO₂.

$$a = d_{PMMA} + d_{SiO2} \qquad (3.1)$$

A combination of scanning electron microscopy (SEM) and confocal microscopy (Appendix: Section 8.3 and Figure 8.1) was used to determine the relative distribution of each component material and the absolute thickness of the multilayer structure. All thickness values used in the theoretical measurements are taken from the SEM images, thereby accounting for the experimental discrepancy that arises out of the penetration of PMMA into the voids in the silica

layer. The SEM images are shown in Figure 3.1. As computed from the images, the periodicity of the two stacks A and B is given as:

Stack A:
$$a = 117 \text{ nm}$$
$$d_{PMMA} = 38 \pm 4 \text{ nm}$$
$$d_{SiO2} = 79 \pm 6 \text{ nm}$$

and

Stack B:
$$a = 100 \text{ nm}$$
$$d_{PMMA} = 45 \pm 5 \text{ nm}$$
$$d_{SiO2} = 55 \pm 5 \text{ nm}$$

The thickness of the PMMA and silica layers obtained from SEM images is used for the theoretical calculations of the spectra. The slight thickness variations of the constituent layers do not influence the robust band structure, as discussed later in Section 3.2.6. However, a change in lattice spacing as in the case of stacks A and B can greatly alter the phonon dispersion, thereby making periodicity a prominent factor in engineering the band diagram in 1D phononics.
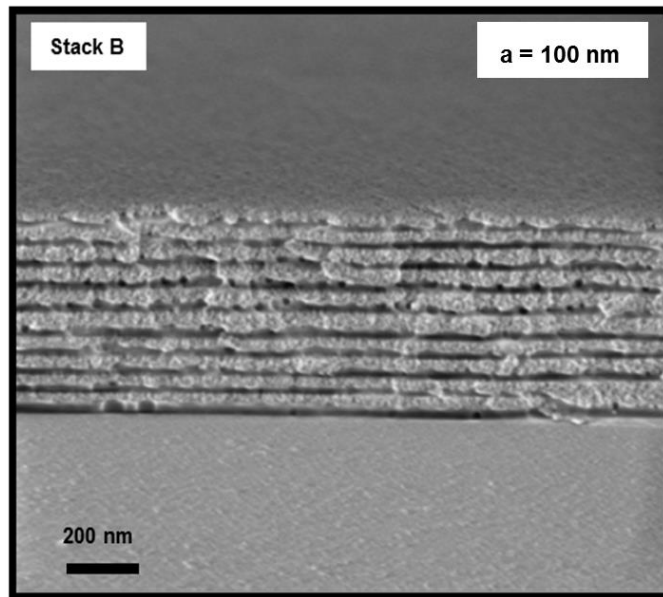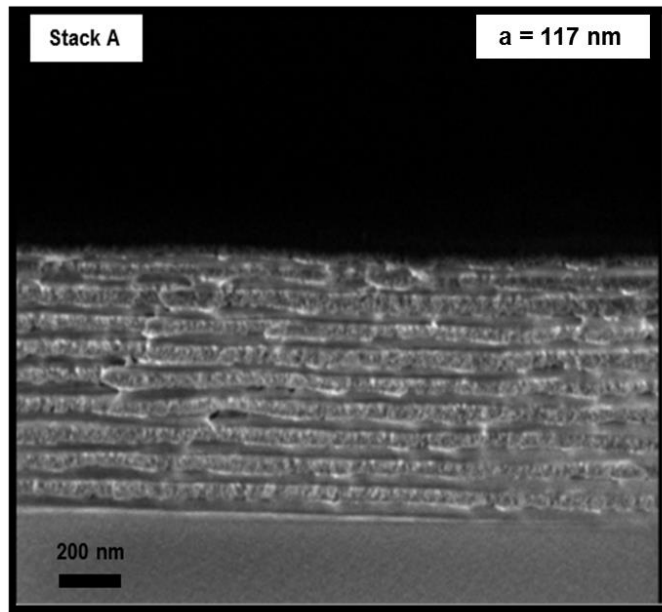
Figure 3.1. *Cross-sectional SEM images of two spin-coated PMMA/p-SiO$_2$ Bragg stacks A and B with periodicity a = 117 and 100 nm, respectively. The scale bar is 200 nm.*

The SEM images clearly show that periodicity is retained throughout the fabrication process. The thickness variations of each layer (± 5nm) obtained from the SEM images does not adversely affect the robustness of the band diagram, as can be seen later in this chapter.

3.2.2. Phonon Propagation in Hybrid Bragg Stacks

Spontaneous Brillouin Light Scattering (BLS) Spectroscopy is employed to analyze phonon propagation in the *PMMA/SiO2* hybrid Bragg stacks. The theory and experimental details of BLS are given in Section 2.5. For a periodic structure, the scattered wave vector q differs from the wave vector of photon by a factor G, where G is the reciprocal lattice vector of the phononic crystal. The dispersion relation is then described by the plot $\omega(k)$. The direction of propagation can be selected by changing the scattering geometry. During the course of this work, different scattering geometries are taken into account (Figure 3.2). Along the direction of periodicity (on-axis), $q = q_\perp$ is perpendicular to the layers (hence, $q_{//} = 0$), whereas in-plane propagation is investigated for $q = q_{//}$ along the layers (and hence $q_\perp = 0$). Oblique incidence is discussed later in this chapter where phonon propagation is considered under the conditions of $q_\perp, q_{//} \neq 0$ (off-axis).

In-plane   **Out-of plane**
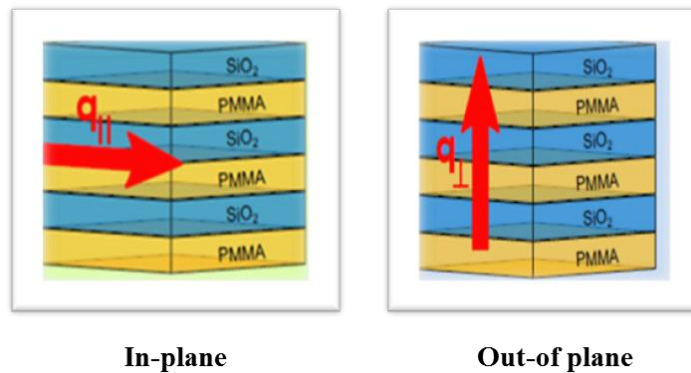
Figure.3.2. *Phonon propagation in hybrid Bragg stacks in different scattering geometries*

Both stacks A and B were investigated through an available q-range to obtain the dispersion relation $f(q_\perp)$ for phonon propagation. The BLS spectra for two $q_\perp$ values near the edge of the

first Brillouin zone (BZ) are shown in Figure 3.3. For the 1D *PMMA/SiO$_2$* hybrid Bragg stack, q_{BZ} = π/a appearing at G/2, where *G* is the reciprocal lattice vector. Figure 3.3 shows the double-peak structure of the BLS spectra for stacks A and B at q_{BZ} = 0.0269 and 0.0314 nm^{-1}. The values differ due to the different periodicity of both the stacks (117 nm for stack A and 100 nm for stack B).
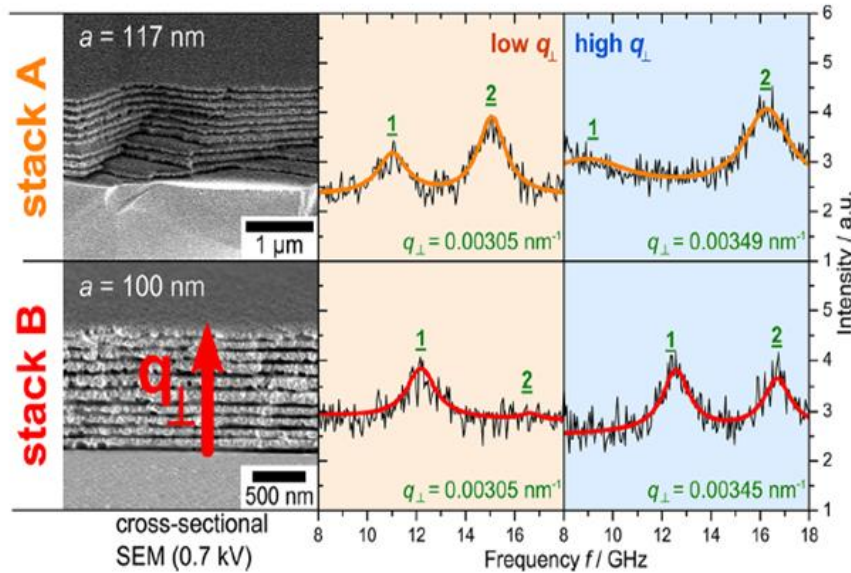
Figure 3.3. *The phononic band gap of the two Bragg stacks A and B can be seen at a glance. The two phonon branches (1 and 2) vary in intensity for both of the stacks at same $q_\perp$ values, a direct result of different lattice spacing in Stacks A and B (as evident from the SEM images).*

As can be seen from Figure 3.3, the BLS spectra shows a double peak structure corresponding to two bands (1) and (2) which denote the low and high frequency peaks respectively. Since the periodicity in stack A and B is different, this is reflected also in the BLS spectral shape. For the high $q_\perp$ value, stack A with $a = 117$ nm shows mainly the high frequency branch (2) at about 16 GHz and a very weak low frequency branch (1) at 9 GHz. Stack B on the other hand displays both branches at the same high $q_\perp$ value (right panel of Figure 3.3). This situation is reversed for the low $q_\perp$ values (middle panel of Figure 3.3). This behavior demonstrates the shape sensitivity

of the BLS spectra to the different periodicity of stack A and B. The BLS spectra corresponds to different $q_\perp a$ values and the Bragg gap depends on the proximity to the edge of the Brillouin zone (at $q_\perp a = \pi$).

The eight frequencies of the four BLS spectra shown in Figure 3.3 are mapped to give the normalized dispersion diagram for phonon propagation perpendicular to the layers of the two stacks A and B. Figure 3.4 shows the Bragg gap occurs at $q_\perp a /\pi = 1$ and the center of the gap lies at $2fa/c_{L,\perp} = 1$, where $c_{L,\perp}$ is the effective longitudinal sound velocity along the z-axis.
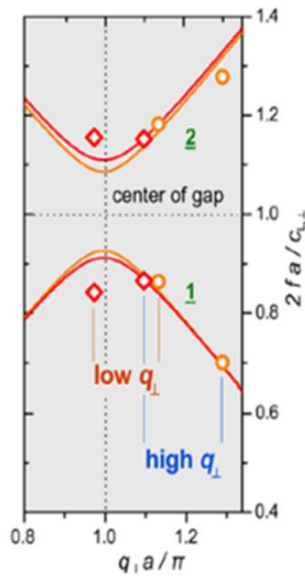
Figure 3.4. *The normalized dispersion diagram of the eight frequencies of the four BLS spectra from Figure 3.3 is shown, with the indicated Bragg gap. The orange and red lines denote the dispersion relation for stacks A and B respectively.*

The BLS spectra are represented by a double Lorentzian line shape. Theoretical measurements were also carried out and explained in detail in section 3.2.3. Figure 3.5 gives a comparison of experimental and theoretical data for the two stacks. The solid lines (blue and green) represent the theoretical spectra for stack A and B respectively in the background of the experimental signals. It is observed that the theoretical and experimental data agree largely with each other.
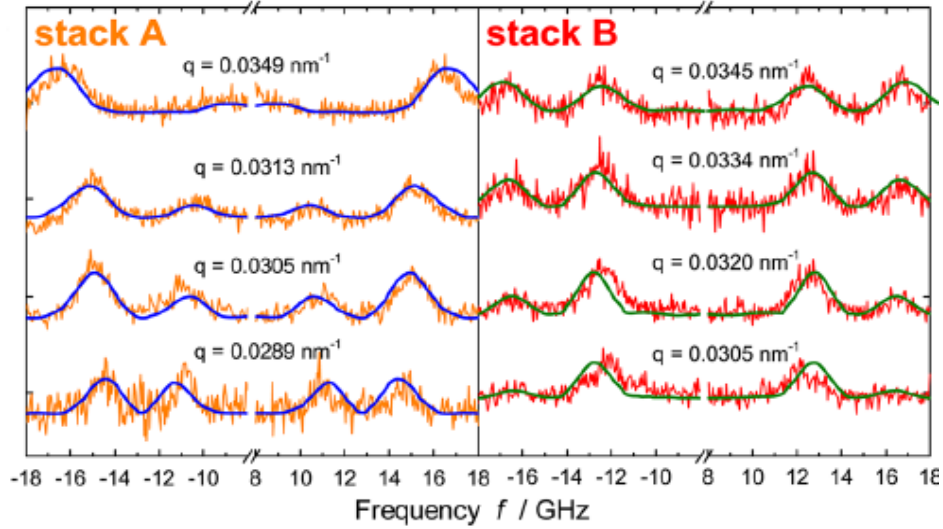
Figure 3.5. *Experimental BLS spectra of the stack A and B superimposed with the theoretical spectra (solid lines) at different phonon wave vectors $q_\perp$ normal to the layers.*
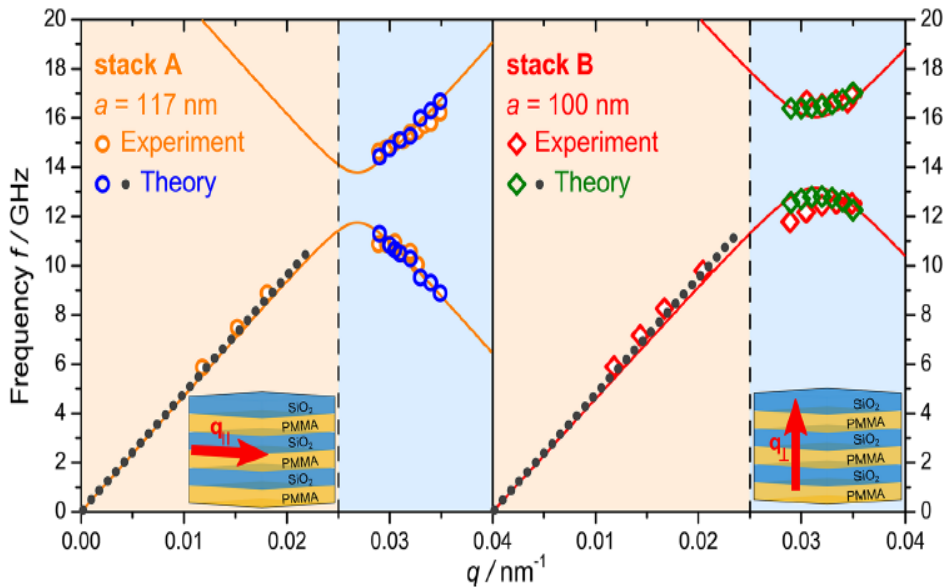
Figure 3.6. *Dispersion relation of stacks A and B with the experimental data shown in yellow circles/red diamonds. The theoretical data is indicated by blue and green colors for stacks A and B respectively. The in-plane and out of plane phonon propagation is depicted by peach and blue back ground respectively, separated by vertical dashed lines.*

The in-plane and out of plane phonon propagation is well represented by the dispersion relation, f versus $q_\perp$ for the two hybrid stacks (Figure 3.6). The peach and blue backgrounds indicate in-plane and out of plane propagation separated by the dashed vertical lines. For the 1D Bragg stack of PMMA and SiO_2 with twenty alternating layers, a stop band is observed in the hypersonic region of frequency. However, the position of the stop band is different since the two stacks have different periodicity ($q_\perp a = \pi$). The opening of a hypersonic phononic stop band along the periodicity direction is demonstrated with the two stacks covering different regimes in the Brillouin zone (BZ); stack A falls mainly into the second BZ. Stack B shows a larger band gap with a width of around 3 GHz due to its lower lattice spacing compared to that of stack A. Within this frequency region, hypersonic longitudinal phonons cannot propagate normal to the layers, thus giving rise to a unidirectional band gap.

The linear dispersion for phonon propagation parallel to the stacks (*for $q_{//}$*) is indicated as a dotted line along with the experimental data along the same direction. It is observed that the solid lines (*for $q_\perp$*) and the dotted lines (referring to $q_{//}$) do not coincide, signifying different effective medium sound velocities along the two directions. The low $q_\perp$ values (when $q_\perp < q_{BZ}$) cannot be retrieved due to experimental limitations. However, the BLS spectrum in this region is easily accessible for in-plane propagation of phonons and thus recorded. Figures 3.5 and 3.6 show experimental and theoretical data which are closely overlapping despite the small differences in the elastic parameters of the two stacks (Table 3.1).
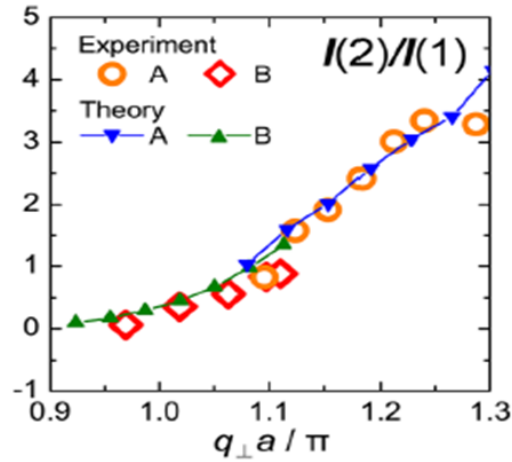
Figure 3.7. *The ratio I (2)/I (1) of the intensities of the high and low frequency bands obtained from the BLS spectra shown in Figure 3.5.*

The intensities of the low and high frequency peaks in the BLS spectra defined by *I (1)* and *I (2)* are different in both of the stacks under consideration. The intensity ratio of the two stacks is plotted and compared to the theoretical results in Figure 3.7. It is observed that although the stacks A and B have different layer spacing, the intensity ratio *I (2)/I (1)* of the two bands superimpose on a common curve when plotted versus $q_{\perp}a$, thereby justifying the larger ratio observed for stack A (Figure 3.5). The intensities *I(1)* and *I(2)* of the two first-folded modes depend on the relative fraction of the two layers, while the strong variation of *I (2)/I (1)* is predicted at the edge of the first BZ. [16]

Table 3.1. *Values Used in Theoretical Calculations* [a]

	Parameters	**PMMA**	**p-SiO$_2$**	**Substrate**
Stack A	c_L (m/s)	2800 [b]	3100	5600
	c_T (m/s)	1400 [b]	1800	
	ρ (kg/m^3)	1190 [b]	1420	2200
	d (nm)	38	79	
	n	1.49	1.46	1.53
Stack B	c_L (m/s)	2800 [b]	3030	5600
	c_T (m/s)	1400 [b]	1800	
	ρ (kg/m^3)	1190 [b]	1500	2200
	d (nm)	45	55	
	n	1.49	1.46	1.53

[a] Sound velocities (c_L, c_T), density (ρ), thickness of layer (*d*) and refractive index (*n*).

[b] Parameters fixed to the values of bulk PMMA film.

3.2.3. Theoretical Calculations for Phonon Propagation

A thorough understanding of the phononic properties of 1D hybrid Bragg stacks requires a full interpretation of the experimental BLS spectrum that involves the simultaneous representation of intensities of the two modes and the dispersion relations. A detailed computation of the BLS spectrum is therefore carried out based on the calculation of the density of vibrational states (*DOS*) and the ratio of elasto-optic coefficients in PMMA and p-SiO$_2$. The latter co-relate

material displacements with refractive index variations. The values of the physical quantities used in theoretical calculations are given in Table 3.1.

In the present work, the density of states *n(ω,k)* is calculated by using the Green's method and the theory of interface response in accordance with the elasticity theory.[17] This combination offers an easy calculation of the displacement field at any point inside the composite material, particularly the reflected and transmitted waves. The dispersion relations of propagating and localized modes are given by the determinant of the inverse Green's function of the interface space g (MM) in equation 3.2.

$$\det \left[g \, (MM) \right]^{-1} = 0 \tag{3.2}$$

The Green's function takes into account the interfaces M separating the layers in a phononic lattice. The details of the calculation can be found in a review by El Boudouti et al [17]. However, some specifics are described here in view of relevance to the present work. When an acoustic wave propagates through the superlattice, periodic variations of strain induce a modulation of the dielectric tensor ε_α in the medium α due to its photo-elastic connection to elastic fluctuations. In the hybrid Bragg stacks under consideration, the medium α is taken to be PMMA or SiO_2. The dielectric fluctuation in each medium is related to the longitudinal displacement field along the periodicity direction z by the photo-elastic constant p_α, as indicated by equation 3.3.

$$\Delta\varepsilon_\alpha = p_\alpha \, \frac{\partial u_\alpha \, (z)}{\partial z} \tag{3.3}$$

and

$$p_\alpha = -\varepsilon_\alpha{}^2 P_{1133}{}^\alpha \tag{3.4}$$

The factor $P_{1133}{}^\alpha$ in equation 3.4 is the photo-elastic tensor in medium α along x = 1 and z = 3 directions. The scattered field $E_s \, (\omega, \, q_\perp)$ occurs due to an interaction between incident light and phonons. Generally, the theoretical calculation is done by taking into account the variable factors, in this case the elastic and optical variation of the layers. In addition, the modulation $\delta\varepsilon$ caused by the displacement of the interface because of the strain (the opto-mechanical effect) is also to be

considered. In the present case however, the dielectric modulation of the multilayer structure can be neglected because the layers are thin (<100 nm) as compared to the probing optical wavelength (532 nm). The case also holds when the layers have almost the same refractive indices. From the optical point of view, the system can then be considered as homogenous leading to a simplified E_s relation. The scattered intensity I_s is related to the scattered field E_s by the relation

$$I_s\ (\omega,\ q_\perp)\quad \alpha \quad |\ E_s\ (\omega,\ q_\perp)^2\ | \tag{3.5}$$

The values of the parameters in Table 3.1 and the equation 3.5 are used to give a theoretical fit to the BLS spectra shown in Figure 3.5. Similarly, the computed intensity ratio of the two modes in the BLS spectra (Figure 3.7) and the frequencies of modes (1) and (2) (blue and green symbols in Figure 3.6) in the dispersion relations of the two stacks are in good agreement with the corresponding experimental values. Even if the theoretical calculations for stack B at higher $q_\perp a/\pi$ values (between 1.1−1.3) are extrapolated, slightly lower intensity ratios are observed as compared to those seen in stack A.

3.2.3.1. Computation of Sound Velocities

The dispersion diagram (Figure 3.6) for the 1-D hypersonic phononic crystals is given by the relation [18] derived from equation 3.6.

$$\cos\ (ka) = \cos\ \left(\frac{\omega d_{SiO_2}}{c_{L,SiO_2}}\right)\cos\left(\frac{\omega d_{PMMA}}{c_{L,PMMA}}\right) - \frac{1}{2}\left(\frac{Z_{SiO_2}}{Z_{PMMA}} + \frac{Z_{PMMA}}{Z_{SiO_2}}\right)sin\left(\frac{\omega d_{SiO_2}}{c_{L,SiO_2}}\right)sin\left(\frac{\omega d_{PMMA}}{c_{L,PMMA}}\right)$$

$$\tag{3.6}$$

In equation 3.6, d is the thickness of the layer, a is the periodicity and $Z = \rho c_L$ is the longitudinal elastic impedance of the layer. The values from Table 3.1 are used in computing the dispersion relation based on equation 3.6. The close agreement of the experimental and theoretical dispersion relation is obvious from Figure 3.6. The effective medium longitudinal sound velocity $c_{L,\perp}$ is obtained from the slope of the linear part of the dispersion relation in the low q-limit in Figure 3.6. The value comes out to be *2970m/s for stack A and 2890*

m/s for stack B. Theoretically, these values can also be calculated from Wood's law, [19] which in turn is obtained from Taylor expansion of equation 3.6 at $\omega = 0$.

$$\frac{1}{\rho_{eff}c^2{}_{L,\perp}} = \frac{\phi}{\rho_{PMMA}c^2{}_{L,PMMA}} + \frac{1-\phi}{\rho_{SiO_2}c^2{}_{L,SiO_2}} \tag{3.7}$$

In equation 3.7, $\rho_{eff}c_{L,\perp}{}^2$ denotes the bulk modulus of stack A or B, ρ_{eff} is the effective density and ϕ is the volume fraction given by the relation.

$$\rho_{eff} = \phi\rho_{PMMA} + (1-\phi)\rho_{SiO_2} \tag{3.8}$$

$$\phi = \frac{d_{PMMA}}{a} \tag{3.9}$$

The equations 3.7, 3.8 and 3.9 can be used to calculate the theoretical effective medium longitudinal sound velocity in stack A or B. In the direction parallel to the layers, the effective medium sound velocity $c_{L,//}$ is an average of the elastic properties in the individual layers because of the influence of the sagittal modes. It is observed from the dispersion diagram that the computed in-plane acoustic phonon frequency[20] (dots indicating theoretical data points in Figure 3.6) is in agreement with the experimental frequencies along the same direction. The slopes of these dotted lines for the two stacks give the sound velocities for in plane propagation *$c_{L,//}(A) = 3020$ m/s and $c_{L,//}(B) = 2990$ m/s* respectively. These are slightly higher than the corresponding sound velocities for out of plane propagation, $c_{L,\perp}$. This slight difference in the sound velocities might indicate a low (<5%) mechanical anisotropy normal and parallel to the layers.

3.2.3.2. Determination of Band Gap Width

The calculation of the width of the band gap requires setting down certain conditions. In the present computations, two standard cases are taken into account. The first case holds that the stack A follows the provision in equation 3.10,

$$\frac{d_{SiO_2}}{c_{L,SiO_2}} = 2 \left(\frac{d_{PMMA}}{c_{L,PMMA}} \right) \tag{3.10}$$

In this situation, the frequencies of the upper and lower limit of the band gap are given by

$$f_{1,2} = \frac{c_{L,PMMA}}{2\pi d_{PMMA}} \cos^{-1} \left(\frac{Z_{PMMA,SiO_2}}{Z_{PMMA} + Z_{SiO_2}} \right) \tag{3.11}$$

Calculating the frequencies f_1 and f_2 from the band diagram, the band gap width is calculated from equation 3.12

$$\Delta f = f_2 - f_1 \tag{3.12}$$

For stack A, the width of the band gap is computed to be approximately **2 GHz** which is in good agreement with the experimentally observed band gap (Figure 3.6). To calculate Δf for stack B, the assumption is made that

$$\frac{d_{PMMA}}{c_{L,PMMA}} = \frac{d_{SiO_2}}{c_{L,SiO_2}} \tag{3.13}$$

The system is then taken to be a *"quarter wave stack"* as the center of the first gap is given by equation 3.14. This means that the individual layers in the stack have the thickness of a quarter of the wavelength. This leads to the widest possible band gap in a one dimensional phononic crystal [21] and the frequency branches for the upper and lower limit of the band gap are given by equation 3.15.

$$\frac{f_o d_{PMMA}}{c_{L,PMMA}} = \frac{f_o d_{SiO_2}}{c_{L,SiO_2}} = \frac{1}{4} \tag{3.14}$$

$$f_{1,2} = f_o + \frac{2f_o}{\pi} \sin^{-1}\left(\frac{Z_{PMMA} - Z_{SiO_2}}{Z_{PMMA} + Z_{SiO_2}}\right) \tag{3.15}$$

In equation 3.15, f_o is the frequency at the center of the band gap described by the wave vector k_{BZ} = π/a. From calculations, stack B shows a larger band gap (*Δf ~ 3 GHz*) as compared to that of stack A (*Δf ~ 2 GHz*) which is also in agreement with the experimentally measured band gap width. The above equation 3.15 is the same for 1D photonics and phononics in the case of quarter wavelength multilayers at normal incidence. [22] The above calculations for the width of the band gap hold for two special cases described earlier. In general, the band gap width can be determined by the relation in equation 3.16 for phononic structures with relatively small elastic impedance contrast ($\Delta Z/\bar{Z}$). [23]

$$\Delta f \cong \frac{2f_o}{\pi} \sin\left(\frac{\pi d_{PMMA} c_{L,SiO_2}}{d_{PMMA} c_{L,SiO_2} + d_{SiO_2} c_{L,PMMA}}\right) \frac{\Delta Z}{\bar{Z}} \tag{3.16}$$

In equation 3.16, $\Delta Z = |Z_{PMMA} - Z_{SiO2}|$ *and* $\bar{Z} = (Z_{PMMA} Z_{SiO2})^{1/2}$. The value of f_0 is obtained from the relation

$$\frac{1}{2f_0} = \frac{d_{PMMA}}{c_{L,PMMA}} + \frac{d_{SiO_2}}{c_{L,SiO_2}} \tag{3.17}$$

The term f_o indicates the middle frequency of the band gap only for a quarter wave stack for which the width of the band gap is maximum. In other instances, the band gap width depends on a number of parameters such as the thickness and sound velocity of the individual components of a 1-D phononic crystal. The impedance contrast ($\Delta Z/\bar{Z}$) also plays an important role in determining the width of the band gap. In the present case of 1D phononic Bragg stacks of *PMMA/p-SiO₂*, the impedance mismatch is about 0.37.

The width of the band gap in stacks A and B can be calculated from equations 3.11, 3.15 and 3.16 since both the stacks present small elastic contrast. Two simple relation are achieved for stack A ($d_{PMMA}/d_{SiO2} \cong 0.5$) and stack B ($d_{PMMA}/d_{SiO2} \cong 1$).

$$\Delta f \cong \frac{\sqrt{3}}{6} \frac{c_{L,PMMA}}{\pi d_{PMMA}} \frac{\Delta Z}{Z} \cong 1.8 \; GHz \tag{3.18}$$

and

$$\Delta f \cong \frac{1}{2} \frac{c_{L,PMMA}}{\pi d_{PMMA}} \frac{\Delta Z}{Z} \cong 3 \; GHz \tag{3.19}$$

It is obvious from a comparison of equations 3.18 & 3.19 with Figure 3.6 that the theoretical and experimental stop band widths are in close agreement with each other. The above exercise and the resulting agreement lead to important conclusions summarized below.

(i)   In 1D phononic structures, the phononic dispersion is not only dependent on the mismatch of elastic impedance $\Delta Z/Z$ as is the case in photonics. In contrast, the density and sound velocity of both constituent layers figure prominently in phononics as shown explicitly in equation 3.6.

(ii)   There is a difference in the physical parameters, density, and longitudinal elastic modulus of the porous SiO_2 layer as compared to those in silica glass. The slightly lower values in the hybrid stacks may be due to the porosity in the SiO_2 layer. The quantities are also slightly different in the two stacks.

(iii)   The thicknesses of the individual layers are uniquely attained.

(iv)   The effective medium elastic parameters such as ρ, $c_{L,\perp}$ are obtained from the low frequency mode in the BLS spectra which appears only at low $q_{\perp}$ values.

3.2.4. Tuning Phononic Band Structure by Oblique Incidence

In the present work, a versatile method to tune the phononic band structure has been adopted. The key feature of this technique is to utilize the concept of oblique incidence by simply rotating the film around its axis normal to the scattering plane (also known as the sagittal plane). A schematic

in Figure 3.8 shows the geometry in which the scattering wave vector q deviates from $q_\perp$. This triggers a mixing with sagittal modes which are the in-plane propagating transverse modes.
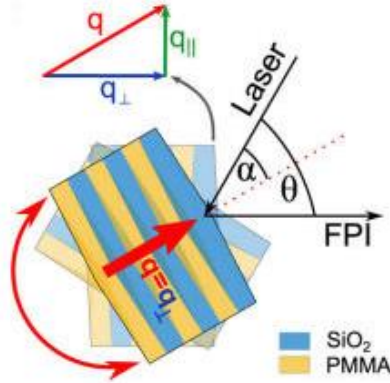
Figure 3.8. Oblique propagation of phonons. The experimental geometry indicates that the laser and detector remain fixed while the Bragg stack is rotated around the normal of the sagittal plane.

In an endeavor to tune the band structure, the geometry of the oblique incidence means a fixed position for the laser and the detector. The angle α is varied at constant scattering angle $\theta = 150°$. In the case of oblique incidence, the scattering wave vector q is represented by a linear combination of $q_\perp$ and $q_{//}$. Hence in this experimental geometry, q is a function of both the scattering angle θ and the incident angle α as given by the following relations.

$$q_\parallel = q \ \sin\left[\frac{1}{2}\left(\sin^{-1}\left(\frac{1}{n}\sin\alpha\right) - \sin^{-1}\left(\frac{1}{n}\sin(\alpha+\theta)\right)\right)\right] \tag{3.20}$$

$$q_\perp = q \ \cos\left[\frac{1}{2}\left(\sin^{-1}\left(\frac{1}{n}\sin\alpha\right) - \sin^{-1}\left(\frac{1}{n}\sin(\alpha+\theta)\right)\right)\right] \tag{3.21}$$

$$q = \sqrt{q^2_\parallel + q^2_\perp} \tag{3.22}$$

The experimental depiction of the dependence of the wave vector q on the incident angle α can be observed in Figure 3.9.
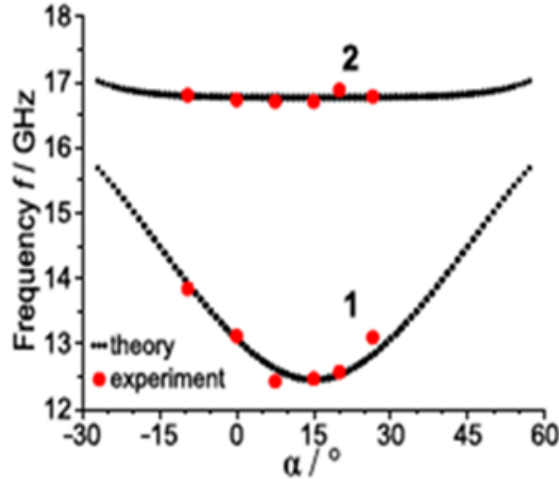
Figure 3.9. *The frequency of the low (1) and high (2) frequency modes are depicted as a function of the incident angle α for stack B. The scattering angle is kept fixed at 150˚.The experimental data is shown as red data points and the theoretical calculation is represented by the dotted lines.*

Figure 3.9 illustrates the low and high phonon frequencies of modes (1) and (2) respectively as function of the incidence angle α in stack B (at θ = 150°). It is observed that as α deviates from *(π − θ)/2* (which is 15° in this case), the low-frequency mode (1) approaches the high-frequency mode (2). As a result, a narrowing effect of the band gap is recorded. On the other hand, the high frequency mode (2) is unusually robust to the variation in the incidence angle. This is also in agreement with the theoretical calculations shown as dotted lines in Figure 3.9. A similar trend is predicted for stack A.

The independence of the high frequency mode (2) on α does not imply that it is not reliant on $q_\perp$ and $q_{//}$, since both frequency modes are dispersive. The minimum for the frequency of mode (1) occurs at the angle α = *(π − θ)/2* (=15˚) indicates perpendicular propagation involving only the longitudinal modes. When α deviates from this value, the longitudinal modes convert to transverse modes. [24] It has been confirmed from calculations that the high frequency mode (2) remains typically longitudinal with an almost constant frequency. However, the lower

frequency Bragg mode (1) involves a partial mixing of polarizations occurs. This is indicated by the variation of frequency of mode (1) with α only while the frequency of mode (2) remains unchanged. Another corroboration is seen in the fact that degeneracy is strongly lifted in the calculated dispersion at increased $q_{//}$ (when α deviates further from 15°), thereby leading to an increasing frequency (see Figure 3.9).
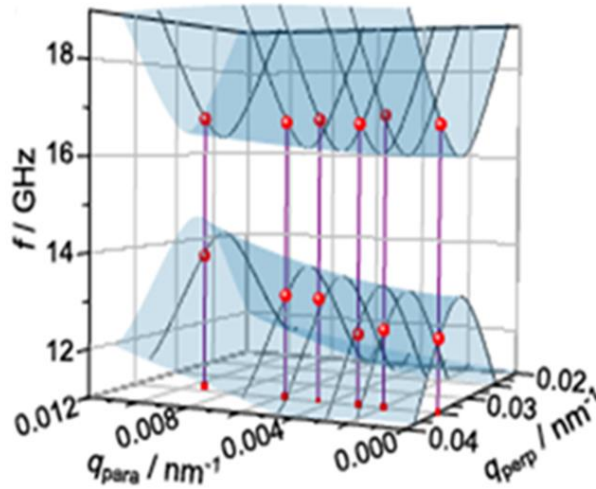
Figure 3.10. *A 3D surface schematic shows the theoretical dispersion relation $f(q_{\parallel}, q_{\perp})$ around the center of the longitudinal band gap for oblique incidence in stack B. The experimental data points at various α (fixed θ at 150˚) are shown in red and shaded if below the surface.*

A three-dimensional dispersion diagram is shown in Figure 3.10 indicating the locus of the high and low frequency modes (red data points for experiment). The theoretical dispersion relations (dotted lines) are also plotted as a function of both $q_{\perp}$ and $q_{//}$. It is observed that the experimental frequencies do not fall at the edge of the Brillouin zone. In addition, the band gap shows a narrowing effect with increasing $q_{//}$ or obliqueness. A significant advantage arising out of this experiment is the mixing of the longitudinal and transverse phonons since it allows an approximation of the shear moduli of the different layers.

The concept of oblique phonon propagation by using a different experimental geometry is depicted very well after a calculation of frequencies of modes (1) and (2) using the shear velocity, $c_{T,SiO2}$ (Table 3.1) as an adjustable parameter. It is noticeable from Figures 3.9 and 3.10 that a particular sample rotation is an advantageous and easy way to tune the band gap. This also allows a concurrent estimation of the shear moduli which are usually inaccessible for normal incidence wave propagation. It would be pertinent to mention here that oblique incidence for 1D phononics is far more complex than for 1D photonic structures. [22] The reason is in photonic lattices, the transverse electric (TE) and transverse magnetic (TM) modes are not coupled.

3.2.5. Estimation of Frequency Modes

In the present section, theoretical calculations are employed to predict modes near the edge of the Brillouin zone for an ideal 1-D phononic superlattice. These predicted modes are then compared with the experimentally observed doublet of the BLS spectrum obtained for stack A, as shown in Figure 3.11.
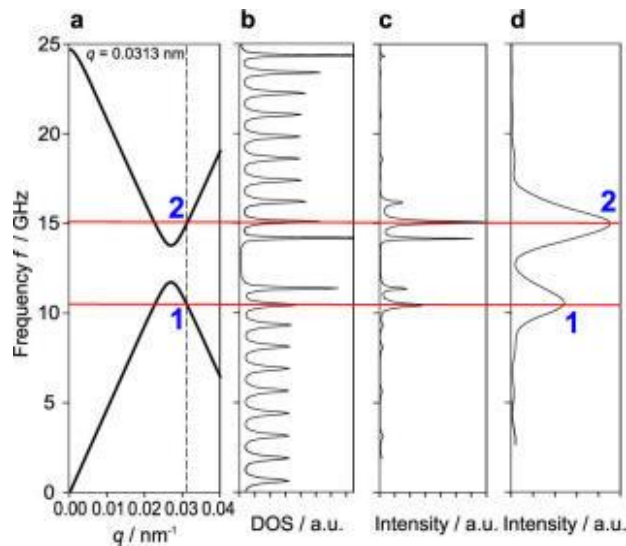
Figure 3.11. *(a) Dispersion curve at normal incidence is shown (b) DOS and (c, d) depict two modeled spectra of dissimilar resolutions at $q_\perp = 0.0313$ nm^{-1}. All calculations are done for stack A*

The density of state (DOS) calculations depicted in Figure 3.11 (b) shows 10 sharp peaks for each branch in the Brillouin zone. The peaks correspond to the number of periods in the phononic superlattice. The line width (fwhm) of the peaks is $\sim$0.25 GHz while the peak separation is around 1.25 GHz. The interaction of the discrete modes in the superlattice with the substrate continuum leads to an intrinsic broadening ($\Gamma^* \sim 0.25$ GHz) of the peaks in the DOS which is smaller within the band gap. This happens because the modes are also propagating within the substrate.

For a chosen $q_\perp$ value of 0.0313 nm^{-1} indicated by a dashed line in Figure 3.11 (a), the BLS spectrum is modeled and shown in Figure 3.11 (c). The computed spectrum shows a triplet spectral structure with a maxima occurring at the selected $q_\perp$ value (indicated by the red lines cutting across the four individual figures in Figure 3.11). The DOS calculations show that only the modes falling close to the frequencies at the selected $q_\perp$ contribute to the theoretical spectrum. The experimental doublet obtained in the BLS spectra (Figure 3.11 (d) and Figure 3.5) is achieved from the theoretical spectrum after convolution of the instrumental Gaussian function ($\Gamma \sim 2\Gamma^* \sim 0.53$ GHz). This prediction of the phononic modes for a single value of q is another indication of the close agreement of the theoretical and experimental data in the present work.

3.2.6. Effect of Structural Imperfections on Band Structure

The SEM images of the two Bragg stacks A and B shown in Figure 3.1 suggests the presence of some interfacial defects in the multilayered structure obtained from spin-coating. It is necessary to mention here that state-of-the-art hybrid (inorganic/polymer) spin coating cannot still compete with the well-established semiconductor fabrication techniques. Methods such as molecular beam epitaxy are more efficient in producing smooth interfaces and coherent structures. Despite this disadvantage, the degree of interfacial roughness in the multilayered stacks obtained from spin coating is much smaller than the layer thicknesses. The losses due to incoherent scattering resulting from surface roughness are suppressed by using phonon wavelengths in the sub-micrometer range. As a result, the probing phonons cannot resolve the small structural roughness and the band structure remains unaltered.

In this section, the influence of structural imperfections e.g., incoherent spacing on the phononic band structure is theoretically discussed. With this purpose in mind, the experimental BLS spectrum of stack A at a fixed $q_\perp = 0.0313$ nm^{-1} is considered. Figure 3.12 shows the experimental spectrum along with the computed spectrum specified by a solid line. The lattice spacing (*a*) is fixed at 117 nm while the thicknesses of the constituent layers are allowed to vary, thereby testing the sensitivity of this representative spectrum in the vicinity of the BZ to structural variations.
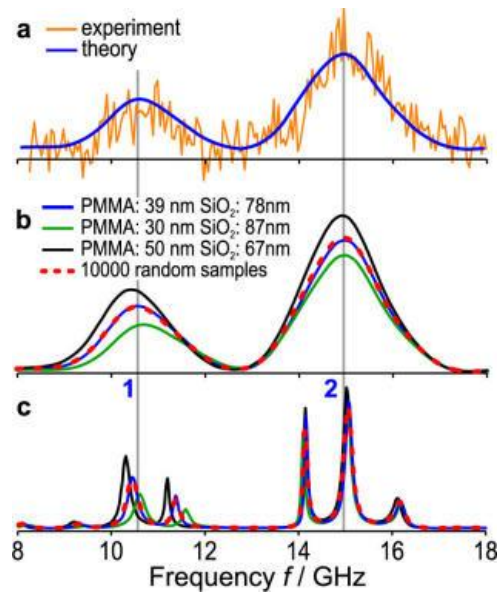
Figure 3.12. *Influence of structural imperfections on band structure (a) Experimental BLS spectrum of stack A at a fixed $q_\perp$ value of 0.0313 nm^{-1} along with the computed spectrum is shown ($d_{PMMA} = 38$ nm and $d_{SiO2} = 79$ nm). (b) The spacing is fixed at 117 nm but d_{PMMA} and d_{SiO2} are varied. The theoretical spectra with different thickness ratios are given. (c) Theoretical spectra of the four cases shown in (b) without instrumental broadening are given.*

Figure 3.12 (a) shows overlapping experimental and theoretical BLS spectra for stack A at a fixed $q_\perp$ value. Three thickness combinations are tested for the above spectrum keeping the lattice spacing fixed at 117 nm, as shown in Figure 3.12 (b). These combinations arise out of varying thickness of PMMA: SiO$_2$ layers and are given as (39: 78, 39: 87 and 50: 67) nm. The spectrum

is theoretically calculated for about 10,000 realizations with different d_{PMMA}/d_{SiO2} ratios. The idea behind this exercise is to find out if the thickness variations as observed from the SEM images influence the BLS spectrum. A large number of structures were simulated to investigate the influence of independent variation of each type of layer spacing. This was achieved by randomly varying the thickness of PMMA (34−44 nm) and SiO_2 (73−83 nm) layers with free lattice constant. The blue curve in Figure 3.12 (b) is the average spectrum obtained for all cases.

These theoretical investigations lead to the remarkable conclusion that the spectral doublet is robust. Only a slight blue shift in the lower frequency band (1) is seen with decreasing d_{PMMA}/d_{SiO2} leading to a narrowing in the band gap. This asymmetric shift of the two frequency peaks along with the band gap width is explained well from equations 3.11, 3.15 and 3.16. However, the greater number of samples considered (dashed line in Figure 3.12(b)) coincide with the average spectrum for $d_{PMMA}/d_{SiO2} = 0.5$ (∼39/78) indicated by the blue curve in Figure 3.12(b). The non-convoluted spectra in Figure 3.12 (c) show that the triplet spectra for both frequency bands (1) and (2) are smeared in Figure 3.12 (b). However, this smearing effect cannot only be attributed to structural inhomogeneity. The spectral widths of both the frequency bands are robust over 16% variation of the volume fraction of the p-SiO_2 layers (or about 20% for the PMMA layers). This corresponds to a para-crystalline lattice distortion parameter of 13 % for both stacks A and B obtained from the SEM images. It is thus safe to conclude here that the smearing due to structural imperfections is much less than the experimental resolution. A full study of effect due to disorders can be fully conducted if the instrumental resolution is considerably enhanced.

3.3. Conclusions

One-dimensional periodic Bragg stacks made of PMMA and p-SiO_2 serve as a model system for a full understanding of elastic wave propagation in nano-materials. A complete control of the phononic band diagram is reported using Brillouin light spectroscopy and theoretical calculations. The multilayered structures show the presence of a large and robust phononic "Bragg" gap for wave propagation along the periodicity direction. The width, the frequency at the

center of the gap, and the intensities of the lower and upper frequency modes are fully described theoretically.

The longitudinal sound velocity normal to the layers and density of component layers can be determined from the phonon dispersion and the amplitudes of the frequency modes. The unavoidable structural disorders introduced during fabrication process have been studied in detail. The thickness variations in constituent layers of the Bragg stacks lead to a smearing of the position of the lower Bragg mode. However, the width of the gap remains constant as indicated by the simulations.

A facile tuning of the band gap width is obtained by oblique incidence utilizing the vector nature of elastic wave propagation. The position and width of the band gap can be controlled by rotating the stack around the axis normal to the sagittal plane of the film. This experimental geometry allows a mixing with the in-plane sagittal modes and makes the estimation of the shear moduli of the individual layers at nano-scale possible. This is a significant advantage since access to both moduli allows an investigation into direction-dependent mechanical properties.

The detailed work on 1-D hypersonic phononics presented here including experimental phonon dispersion and simulations provides the necessary knowledge needed to engineer the band structure. The phonon band structure is a complex affair as compared to the photon and electronic band structures and reflects both structural and elastic properties of the components. In addition, the present work is one of its kind having utilized soft matter fabrication techniques in hypersonic phononics for the first time. The hybrid hypersonic structures created here possess many clear advantages over the conventional semi-conductor fabrication methods. The high-quality periodic structures produced at the nano scale allow an easy control over the elastic impedance contrast, making realization of large phononic band gaps possible. Additionally, there is a distinct possibility of strong interactions of hypersonic phonons with visible photons.

3.4. Instrumental Details

The fabricated Bragg-Stacks of PMMA and p-SiO$_2$ were characterized by SEM on a LEO Gemini 1530 microscope (Carl Zeiss AG, Oberkochen, Germany). The images were taken using

an acceleration voltage of 0.7 kV in secondary electrons InLens detection mode. The SEM pictures are used for estimating layer spacing and volume fraction of the constituent materials.

A confocal microscope (NanoFocus® µSurf®) was used to measure the total thickness of the Bragg stacks. During the experiment, the white light confocal measurement head is moved in z-direction. The multilayer films were dented near the position of BLS measurement and the total thickness of the stack is obtained from the z-difference between substrate and sample surface. The BLS instrumental set-up is described in detail in Section 2.5.1 of the preceding chapter.

Bibliography

1. R. Martinez-Sala, J. Sancho, J. V. Sanchez, V. Gomez, J. Llinares and F. Meseguer, *Nature.* **1995**, 378, 241.

2. M. Eichenfield, J. Chan, R. M. Camacho, K. J. Vahala and O. Painter, *Nature*. **2009**, 462, 78.

3. B. Liang, X. S. Guo, J. Tu, D. Zhang and J. C. Cheng, *Nature. Mat*. **2010**, 9, 989.

4. J. Page, *Nature. Mat*. **2011**, 10, 565.

5. Z. Liu, X. Zhang, Y. Mao, Y.Y. Zhu, Z. Yang, C. T. Chan and P. Sheng, *Science*. **2000**, 289, 1734.

6. T. Gorishnyy, M. Maldovan, C. Ullal and E. Thomas, *Phys. World.* **2005**, 18, 24.

7. W. Cheng, J. Wang, U. Jonas, G. Fytas and N. Stefanou, *Nature Mat*. **2006**, 5, 830.

8. C. Colvard, R. Merlin, M. V. Klein and A. C. Gossard, *Phys. Rev. Lett*. **1980**, 45, 298.

9. G. Saini, T. Pezeril, D. H. Torchinsky, J. Yoon, S. E. Kooi, E. L. Thomas and K. A. Nelson, *J. Mater. Res*. **2007**, 22, 719.

10. W. Cheng, N. Gomopoulos, G. Fytas, T. Gorishnyy, J. Walish, E. L. Thomas, A. Hiltner and E. Baer, *Nano Lett*. **2008**, 8, 1423.

11. I. E. Psarabos, N. Papanikolau, N. Stefanou, B. Djafari-Rouhani, B. Bonello and V. Laude, *Phys. Rev. B*. **2010**, 82, 174303.

12. L. C. Parsons and G. T. Andrews, *J. Appl. Phys*. **2012**, 111, 123521.

13. G. N. Aliev, B. Goller, D. Kovalev and P. A. Snow, *Appl. Phys. Lett*. **2010**, 96, 124101.

14. A. M. Urbas, E. L. Thomas, H. Kriegs, G. Gytas, R. S. Penciu and L. N. Economou, *Phys. Rev. Lett*. **2003**, 90, 108302-1.

15. N. Gomopoulos, D. Maschke, C. Y. Koh, E. L. Thomas, W. Tremel, H. –J. Butt and G. Fytas, *Nano Lett*. **2010**, 10, 980.

16. J. He, B. Djafari-Rouhani and J. Sapriel, *J. Phys. Rev. B*. **1988**, 37, 4086.

17. E. El Boudouti, B. Djafari-Rouhani, A. Akjouj and L. Dobrzynski, *Surf. Sci. Rep*. **2009**, 64, 471.

18. S. M. Rytov, *Sov. Phys. Acoust*. **1956**, 2, 68.

19. A. B. Wood, *A Textbook of Sound*; G. Bell & Sons Ltd, New York, **1930**.

20. B. Djafari-Rouhani, L. Dobrzynski, O. H. Duparc, R. E, Camley and A. A. Maradudin, *Phys. Rev. B*. **1983**, 28, 1711.

21. J. D. Joannopoulos, S. G. Johnson, J. N. Winn and R. D. Meade, *Photonic Crystals: Molding the Flow of Light*; Princeton University Press, Princeton, **2008**.

22. Y. Fink, J. N. Winn, S. Fan, C. Chen, J. Michel, J. D. Joannopoulos and E. L. Thomas, *Science.* **1998**, 282, 1679.

23. B. Jusserand, D. Paquet, F. Mollot, F. Alexander and G. Le Roux, *Phys. Rev. B*. **1987**, 35, 2808.

24. H. Kato, H. J. Maris and S. -i. Tamura, *Phys. Rev. B*. **1996**, 53, 7884.

4

Defects in Hybrid Hypersonic Superlattices

Corresponding Publication:

Dirk Schneider, <u>Faroha Liaqat</u>, El Houssaine El Boudouti, Ossama El Abouti, Wolfgang Tremel, Hans- Jürgen Butt, Bahram Djafari-Rouhani and George Fytas,
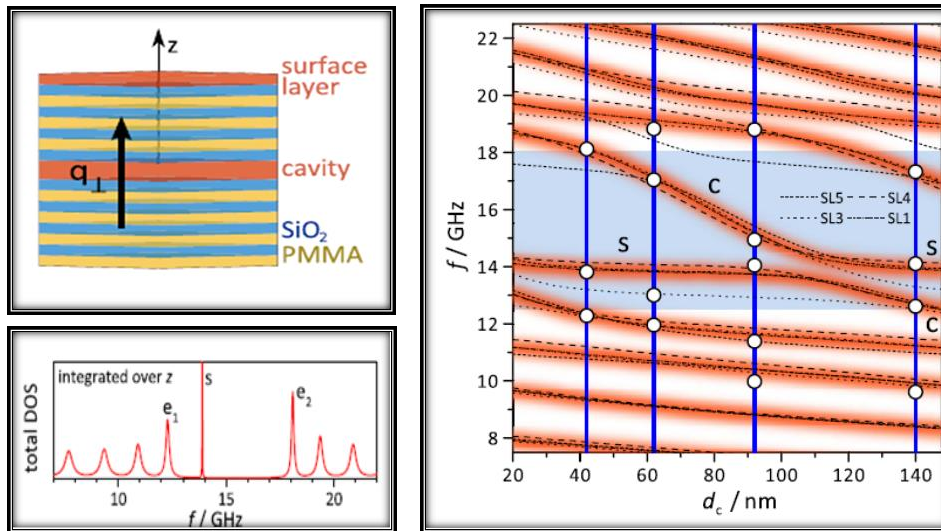
4.1. Introduction

One-dimensional phononic crystals also known as superlattices (*SLs*) are a recent subject of investigation among a variety of phononic nanostructures. The idea of phononic metamaterials was first proposed by Esaki [1] and since then, the unusual acoustic properties of these periodic structures have been subject to aggressive research. Selective transmission of elastic waves in superlattices produced from molecular beam epitaxy was first reported in 1979 and has subsequently led to the idea of phonon filtering by dielectric Bragg mirrors. [2] In 1987, periodic structures with an electromagnetic band gap were proposed by Yablonovitch, [3] thereby paving the way for the corresponding acoustic analogues. A detailed theoretical study of the full band structure of periodic nanostructures was carried out five years later for 3D phononic crystals. [4] The phononic effects are indebted to a significant acoustic impedance contrast in its constituent materials. This fact has been established by numerous theoretical studies for periodic phononic structures. [5-8] A number of experimental works on various phononic structures (crystalline, polymeric or silicon multilayers) have also been reported in recent years. [9-11]

Phononic superlattices offer many advantages in the study of elastic wave propagation since the complex vector nature of the elastic waves is greatly simplified in one-dimensional structures. Such systems offer easy fabrication and design along with simple theoretical calculations. It is therefore easier to manipulate the elastic wave propagation in periodic superlattices. The first evidence of folded acoustic phonons in a semi-conductor superlattice was reported by Colvard et al using Raman scattering. [12] Later on, further Raman studies were carried to demonstrate confinement of acoustical phonons in an optical cavity in semiconductors. [13]

The introduction of defects in a periodic lattice can lead to states within the phononic band gap, resulting in a partial or complete suppression of the band gap. [14] Raman and pump-probe experimental studies have been carried out to study defect modes in phononic structures. These modes can be either localized on the surface within the frequency gaps of folded phonons. [15-17] Additionally, surface-avoiding defect modes have also been reported showing wave vectors near the center or edge of the Brillouin zone. [18, 19] Structural defects in a phononic lattice also influence the shape and frequency of the peaks in the spectra as well affecting the width of the stop band. These factors, if controlled, can provide a way for successful band gap engineering. Introduction of controlled defects in a phononic superlattice has led to coherent phonon generation [20-22] with the high optical confinement

resulting in enhanced phonon detection. Tera-hertz sound amplification has also been reported by stimulated emission of phonons in a semi-conductor superlattice. [23] The interaction of acoustic phonons with light in phonon cavities is another application of introduced defects in phononic structures. [24] A concurrent modulation of light and sound is reported for "phoxonic" crystals: structures having both photonic and phononic band gaps. [25] Other examples of applications of structured defects in phononics include acoustic diodes [26] and reduction in thermal conductivity of semi-conductor superlattices. [27, 28]

However, the investigation of different type of defect states in phononic superlattices has been limited in general to semi-conductor materials. [29] The disadvantages associated with such systems involve a low contrast in elastic impedance and high optical absorption which makes experimental investigations far from the surface difficult. In addition, the fabrication of semi-conductor superlattices usually takes place by molecular beam epitaxy in a clean environment. It is therefore highly desirable to find an alternative phononic 1D system offering easy production with greater impedance contrast.

Superlattices composed of soft polymers and hard inorganic materials can be a possible substitute as they show the added advantages of a greater elastic impedance contrast giving rise to a large band gap. [30, 31] In the past chapter, a 1D hypersonic hybrid phononic system has been reported, built up from organic polymer and inorganic nanoparticles. [32] Such a superlattice offers the possibility of easy fabrication [33] and can be easily manipulated to allow simultaneous operation of hypersonic phonons and visible photons. Hence, an easy modification of these 1D systems may lead to phoxonic structures.

In this chapter, defect-controlled hypersound propagation in hybrid superlattices composed of poly (methyl methacrylate) (PMMA) and porous silica (p-SiO$_2$) is studied. Surface and cavity defects are carefully introduced to the standard Bragg stack described in the previous chapter. This is the first observation of surface and cavity modes in soft matter based phononic superlattices. Furthermore, the subsequent interaction between the surface and cavity defect modes is described in these systems. The introduction of defects in the phononic lattice is brought about by varying the material and thickness of the surface layer, as well as the thickness and position of the cavity layer. The current work also provides a complete theoretical description of the experimental phononic band structure and the Brillouin light scattering (BLS) spectra. The simulations are based on the Green's function method which allows a direct access to the density

of states (DOS). The details of the method are given in Sections 3.2.3 and 8.2. These theoretical studies are instrumental in identifying the modes inside and near the edges of the first Brillouin zone that are activated through breaking of the high symmetry of the periodic superlattice. In short, the current work aims to provide a detailed understanding of phonon propagation in periodic superlattices with structured defects.

4.2. Results and Discussion

4.2.1. Fabrication of Phononic Superlattices with Defects

Hybrid finite superlattices composed of alternating poly (methyl methacrylate) (*PMMA or P*) and porous silica (*p-SiO$_2$ or S*) layers were built up on a clean glass substrate by high speed spin coating. The details of the method are given in Sections 2.3 and 2.4 of this thesis. The constituent layers (except the defect layer) are coated from the respective stock solutions of 2.2% PMMA in toluene (*w/v*) and 3.4% aqueous dispersion of silica nanoparticles (LUDOX AS-30) containing aqueous ammonia and sodium dodecyl sulfate (SDS). The concentration of the stock solutions is adjusted to achieve a target thickness of 50 nm for each P or S layer. The superlattice starts always with the PMMA layer but the surface layer can either be of PMMA or p-SiO$_2$, depending on the type of surface defect desired. Heat treatment at 105 °C is an essential part of fabrication after each coating cycle. The important physical parameters such as the density and longitudinal sound velocity of PMMA are *ρ = 1190 kg/m^3* and *c_L = 2800 m/s* respectively while those for p-SiO$_2$ are *ρ = 1700 kg/m^3* and *c_L = 3150 m/s*, as determined from a previous study. [30]

To study the influence of anomalies in an otherwise perfect stack (*$d^P = d^S \cong 50$ nm*), two types of defected structures were considered; those having surface defects *(s)* only, and those having both surface and cavity *(c)* defects. The thickness of the cavity and surface defects is denoted by *d_c* or *d_s* respectively while the defect location relative to the glass substrate is indicated by N^P or N^S. (The superscript shows the type of layers i.e. PMMA (*P*) and silica (*S*) defect layers). The periodicity *(a)* of the superlattice is designed to be almost constant at 100 nm. The cavity defects are introduced in four samples having PMMA as the defect layer *(C)*. The cavity is introduced at the position of the 5th bilayer in the sequence [(PS)$_4$CS(PS)$_3$P]. The thickness of layer C was varied from 42 nm (SL1), 62nm (SL3), 92 nm (SL4) and 140 nm (SL5)

using different concentrations of casting solutions. In each of these superlattices, the surface layer is of PMMA which is a departure from the standard Bragg stack described in Chapter 3 that ends with the harder p-SiO$_2$ as the surface layer. The actual thickness d_c of each defect layer was determined from scanning electron microscopy (SEM); it is expected to be lower than the targeted thickness due to partial infiltration of PMMA through the porous silica layer.

The effect of the surface and cavity defects for some other experimental sequences was investigated on the superlattices SL2, SL6 and SL7. The design of these Bragg stacks is as follows: SL2 = (PS)$_8$C, SL6 = (PS)$_4$CS(PS)$_4$ and SL7 = (PS)$_9$CS(PS)$_9$. The architecture of these superlattices is described in Table 4.1.

Table 4.1. *Layer Sequence and Elastic Parameters of Hybrid Superlattices*

1D	d$_{PMMA, SiO2}$ (Layer sequence[a]) /nm	c$_L$(SiO$_2$) /ms^{-1}	ρ(SiO$_2$) /kgm^{-3}	c$_L$(PMMA) /ms^{-1}	ρ(PMMA) /kgm^{-3}
SL1	**42** *56* **42** *56* **42** *56* **42** *56* **42** *56* **42** *56* **42** *56* **42** *56* **57**	3150	1700	2800	1190
SL2	**45** *55* **45** *55* **45** *55* **45** *55* **45** *55* **45** *55* **45** *55* **45** *55* **80**	3200	1750	2800	1190
SL3	**42** *55* **42** *55* **42** *55* **42** *55* **62** *55* **42** *55* **42** *55* **42** *80* **54**	3150	1700	2800	1190
SL4	**42** *52* **42** *52* **42** *52* **42** *52* **92** *52* **42** *52* **42** *52* **42** *70* **44**	3150	1700	2800	1190
SL5	**42** *52* **42** *80* **42** *52* **42** *52* **140** *52* **42** *52* **42** *52* **42** *80* **45**	3150	1700	2800	1190
SL6	**41** *50* **41** *50* **41** *50* **41** *50* **95** *50* **41** *50* **41** *65* **41** *50* **41** *85*	3000	1420	2800	1190
SL7	**40** *100* (**40** *53*)$_8$ **85** *53* (**40** *53*)$_{10}$	3150	1700	2800	1190

[a] **Bold** (*italic*) numbers denote the thickness of PMMA(SiO$_2$) layers in nm.

As can be observed from Table 4.1, the values of sound velocity and density for PMMA are constant. However, these parameters for porous silica vary in different SLs, depending on the stock solution used for spin coating. Despite this disadvantage, the layer thicknesses show a good periodic reproducibility in all the superlattices. The values shown in Table

4.1 for $d_{PMMA, SiO2}$ are obtained from the SEM micrographs of the superlattices and are subsequently used in the theoretical calculations. The refractive indices of the constituent materials are n (*PMMA*) = 1.49, n (*SiO₂*) = 1.46, n (substrate) = 1.46 and n (air) = 1. An effective refractive index of 1.47 is assumed for simplifying the theoretical studies. The ratio of the photo-elastic constants was fixed to p_{PMMA}/p_{SiO2} = 2. It is assumed that the thickness of the SiO_2 layer beneath the surface PMMA layer is slightly larger so that an agreement with the experimental spectra can be attained. However, this assumption does not lead to additional modes in the region of the band gap at all.

The insertion of defects in the periodic superlattices can be achieved in a number of ways. The boundary conditions set for theoretical calculations depend on the choice of the surface layer and subsequently influence the band diagram. The SLs are terminated with either a hard SiO_2 or soft PMMA layer. Cavity layers can also be introduced in the superlattice at different positions and thicknesses. The present work focuses on these three ways of introducing defects; (i) Choice of surface layer (ii) Thickness of cavity layer and (iii) Position of cavity layer with respect to substrate. Table 4.2 presents the defected SLs exemplified by different architectures containing the surface and cavity layers of both constituent materials.

Table 4.2. *Structure of Hybrid Superlattices*

1D	a /nm	Cavity layer[a]		Surface layer[a]	
		d_c/nm	N^{mat}	d_s/nm	N^{mat}
SL1	98	-	-	57	17^P
SL2	100	-	-	80	17^P
SL3	97	62	9^P	54	17^P
SL4	94	92	9^P	44	17^P
SL5	94	140	9^P	45	17^P
SL6	91	85	9^P	85	18^S
SL7	93	100	2^S	-	-
		85	19^P	-	-

[a]The superscripts indicate the material i.e. PMMA (*P*) or Silica (*S*) layers while the numbers N indicate positioning of the layers relative to the substrate. The layer thicknesses may show an error of ± 5 %.

4.2.2. Experimental and Theoretical Studies

The work presented in Chapter 3 provides experimental evidence that hybrid superlattices with uniform lattice spacing show large band gaps for phonon propagation normal to the layers. [30, 32] The non-destructive technique of spontaneous Brillouin Light scattering (*BLS*) is used to record the phononic dispersion relation of GHz excitations at different scattering wave vectors *q*. BLS is a sensitive technique to study structural features in hybrid materials and thus very useful in the current work to detect phononic dispersion of defected superlattices.

The band structure of the hybrid superlattices is accessed near the edge of the 1st Brillouin zone since the periodicity and phonon wavelength are comparable to each other. The thickness fluctuations (~ 5%) do not greatly affect the BLS spectra after accommodating the instrumental width, as has been explained in Section 3.2.6. The theoretical spectra are convoluted with an instrumental function to embody the corresponding experimental BLS spectra. The simulations are based on a calculation of density of vibrational states (DOS) and photo-elastic coupling using the Green's method, which has been explained in detail in Section 3.2.3 of this thesis. The broadening of the peaks in the DOS and the BLS spectra is caused by acoustic attenuation, which can be defined in the theory by assigning complex sound velocities to each sublayer.

4.2.2.1. Effect of PMMA Surface Defect Layer

In this section, the effect of surface defects on the phononic band structure is investigated. In the Bragg stacks A and B discussed in Chapter 3, the surface layer was always p-SiO_2. However, this section highlights superlattices SL1 and SL2, each consisting of 8 bilayers (*BL)* capped with the soft PMMA layer. The thickness of the surface layer is 57 nm and 80 nm for SL1 and SL2 respectively (*Table 4.2*). The SEM image of SL1 and the corresponding dispersion relation is depicted in Figures 4.1 and 4.2, respectively.
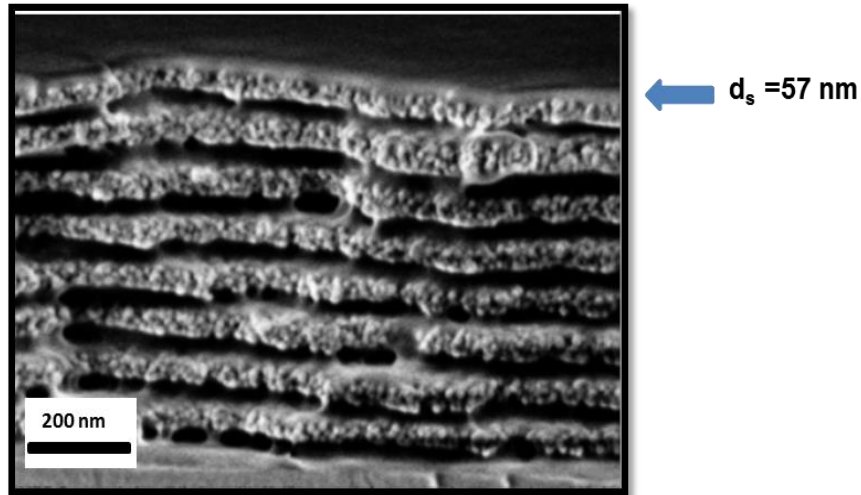
Figure 4.1. Cross-sectional SEM image of superlattice SL1 comprising of eight bilayers and capped with the soft PMMA layer of thickness 57 nm.
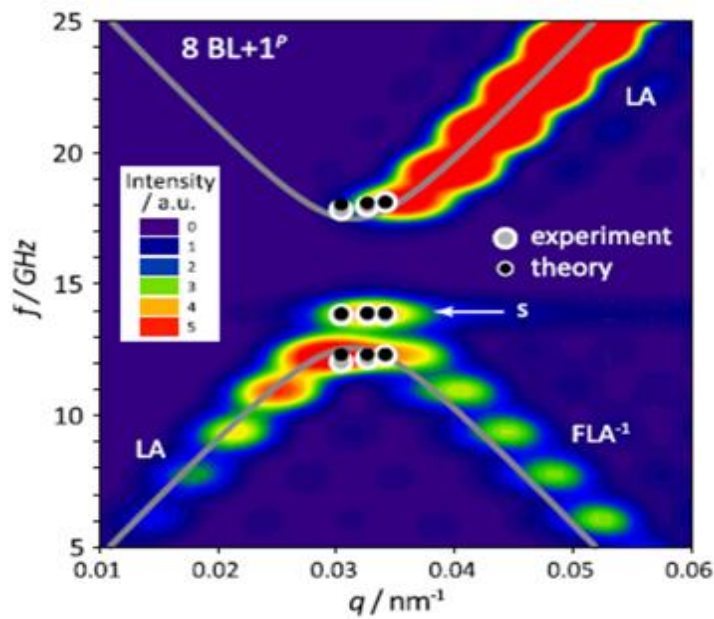
Figure 4.2. Dispersion relation for SL1 with eight bilayers and a PMMA surface layer. The peak positions of experimental and theoretical spectra are represented by white and black circles respectively. The color bar indicates the theoretical Brillouin intensity while the dispersion of the infinite SL is shown by the solid lines.

The superlattice SL1 in Figure 4.1 shows a smooth eight bilayer (8 BL) Bragg stack capped with an additional surface layer of soft PMMA of thickness 57 nm. The altered boundary conditions lead to a breaking of symmetry at the uppermost layer and this is reflected in the band diagram (shown in Figure 4.2) accumulated from the experimental and theoretical data points on the dispersion curve. The phononic band gap for SL1 is much larger (~5 GHz) compared to that observed in standard superlattices A and B discussed in Chapter 3.

An interesting new feature of the band diagram of SL1 (Figure 4.2) with the surface defect is the appearance of a new mode with frequency at ~14 GHz. This frequency mode falls inside the region of the band gap of an infinite defect free superlattice. [31, 32] The theoretical calculations for an infinite SL are represented by the solid lines in Figure 4.2. The computed Brillouin intensity is given as a color scale and it is observed from the contour plot that the modes along the longitudinal acoustic (*LA*) branch are much more intense than along the folded longitudinal acoustic (*FLA^{-1}*) branch. [32, 34] Selected *q* values have been selected for strong experimental detection represented by white circles.
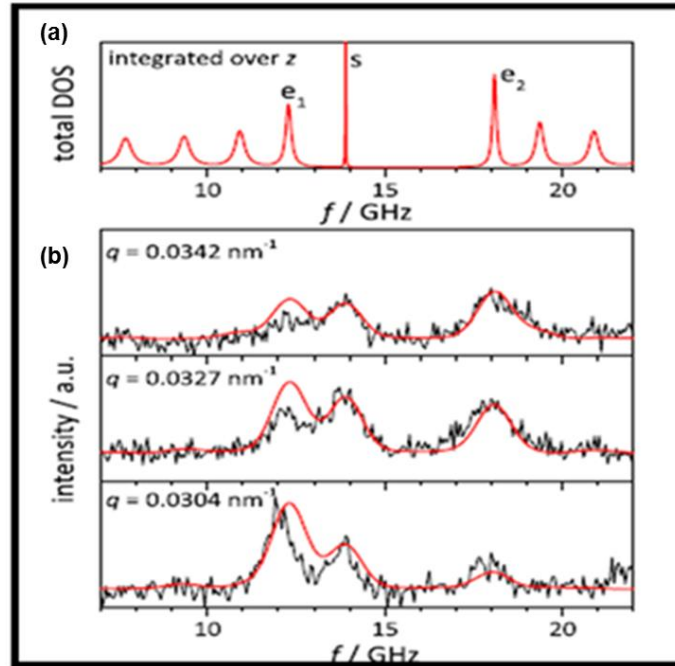
Figure 4.3. *Superlattice SL1 (a) Total density of states (DOS) is given indicating the surface and edge modes. (b) Experimental (black) and theoretical (red) BLS spectra at three $q_\perp$ values are shown.*

In order to identify the nature of the modes appearing in the experimental and theoretical band structure (Figure 4.2), the density of states (*DOS*) for SL1 are calculated using the theory of interface response and Green's method in the framework of the theory of elasticity. The total DOS is shown in Figure 4.3 (a) along with the experimental and theoretical BLS spectra (Figure 4.3 (b)) in black and red colors respectively. Three main contributions are revealed in the DOS for SL1 which are identified as the lower (e_2) and upper (e_1) edge modes and the surface mode (*s*). The lower and upper edge modes appear at 12.5 GHz and 18 GHz respectively while the surface mode appears at 14 GHz, confirmed from the DOS as well as the dispersion relation in Figure 4.2. The resolution of the modes in the BLS spectrum (Figure 4.3 (b)) becomes possible due to the small thickness of SL1. This is due to the fact that the separation between the three modes in DOS exceeds the instrumental width (~ 0.5 GHz).
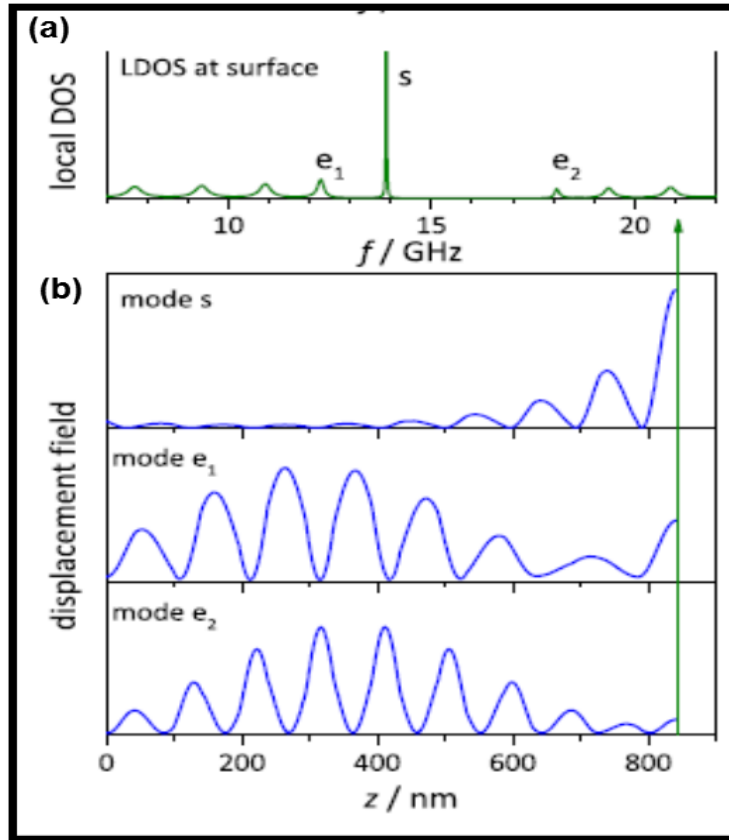
Figure 4.4. *Superlattice SL1. (a) Local DOS at the surface indicating the edge ($e_{1, 2}$) and surface (s) modes is shown. (b) Displacement fields of the modes.*

The local DOS modes for SL1 are shown in Figure 4.4 (a) depicting the significance of the surface mode (*s*). The nature of the modes is identified from their displacement fields (Figure 4.4 (b)). It is seen that the *s* mode increases in intensity near the surface and is hence characterized as the surface mode. In contrast, the *e* modes have their maximum displacement in the middle of the superlattice and are designated as the edge modes. The function of the displacement field for mode e_2 decreases in intensity as it reaches the surface and almost disappears at the top. Hence, the e_2 mode can be described as a *surface avoiding mode* (*SAM*) which has recently been reported for semiconductor superlattices. [19, 35]

4.2.2.1.1. Variation with Thickness of Superlattice

In this section, the effect of thickness of the surface defect layer of PMMA on the band diagram in phononic superlattices will be discussed. A comparison between thinner superlattices (*5 BL*) and thicker superlattices (*20 BL*) is also drawn in Figure 4.5. Naturally, the BLS signal is reduced for the 5 BL superlattice and the quality of the dispersion relation is adversely affected. On the other hand, the separation between individual modes will be greatly reduced for a thicker superlattice of 20 BL, thus making the experimental resolution difficult. The peak in the DOS attributed to the surface mode in the DOS narrows with the increasing number of bilayers in a SL. The strength of the *s* mode coupling with the substrate modes is weakened by the increasing surface-substrate distance. As a result, it becomes very difficult to document this surface mode in the BLS spectrum after convolution with the experimental function. This can be seen from the intensity contour plots for the thin (5BL) and thick (20BL) superlattices (shown in Figure 4.5). The arrow indicates suppression of the *s* modes with the increasing SL thickness.

The finite size calculations for these kind of superlattices have been reported earlier by El Boudouti et al., in 2009. [7] A few of these modes have also been described earlier by elucidation of small satellite lines in Raman spectra. [36, 37] However, the work discussed in this chapter constitutes the first instance of experimentally documented facts highlighting the advantages of employing BLS to elucidate band structure in hybrid phononic superlattices.
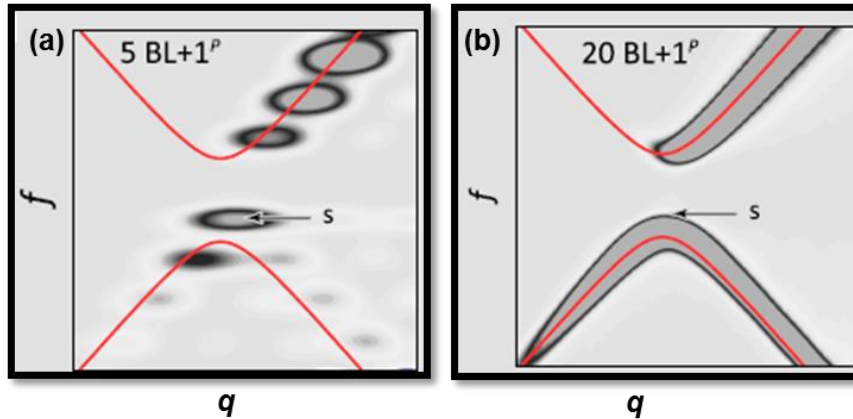
Figure 4.5. *The mode separation and strength of the surface mode (s) in superlattices of different thickness is shown in (a) thin SL (5BL) and (b) thick SL (20 BL). The s mode can hardly be distinguished in the thicker SL as indicated by the arrow indicating the surface mode in (b).*

4.2.2.1.2. Influence of Surface Layer Thickness

In this section, the effect of the thickness of the surface defect layer on the band structure of hybrid SLs is discussed. Two superlattices, SL1 (Figure 4.1) and SL2 (Figure 4.6) are considered having a PMMA defect layer at the surface of thickness 57 and 80 nm, respectively (Table 4.2). Apart from the identification of the surface mode from its displacement field, further evidence is obtained from its reliance on the thickness of the surface layer. [7, 38] It has been theoretically predicted that the frequency of the *s* mode decreases with the thickness of the surface layer (d_s). Eventually, the *s* mode must be tuned inside the band gap with increasing d_s. This theory is tested and experimentally proven in this work by comparing superlattices SL1 and SL2. The dispersion relation for SL2 is shown in Figure 4.7 in which the solid lines indicate the band gap for the infinite superlattice and the color indicates the intensity of the frequency modes.
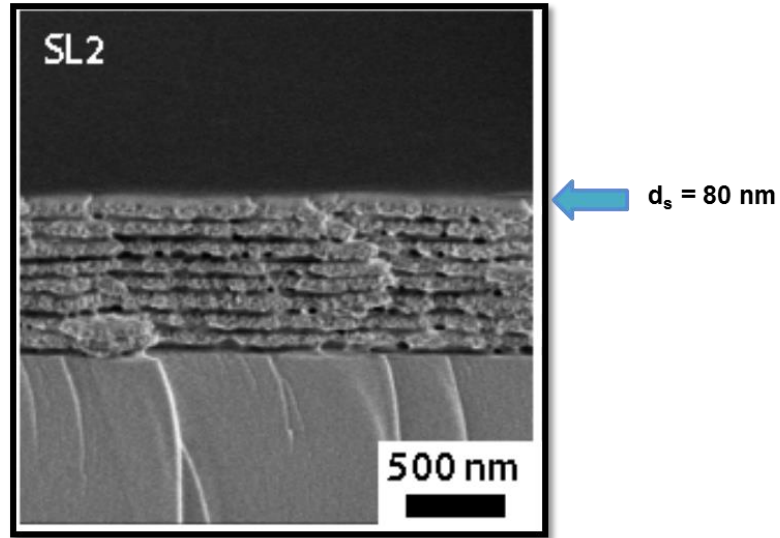
Figure 4.6. *SEM image of superlattice SL2 consisting of eight bilayers capped with a surface defect layer of PMMA. The thickness of the defect layer (indicated by the arrow) is 80 nm.*
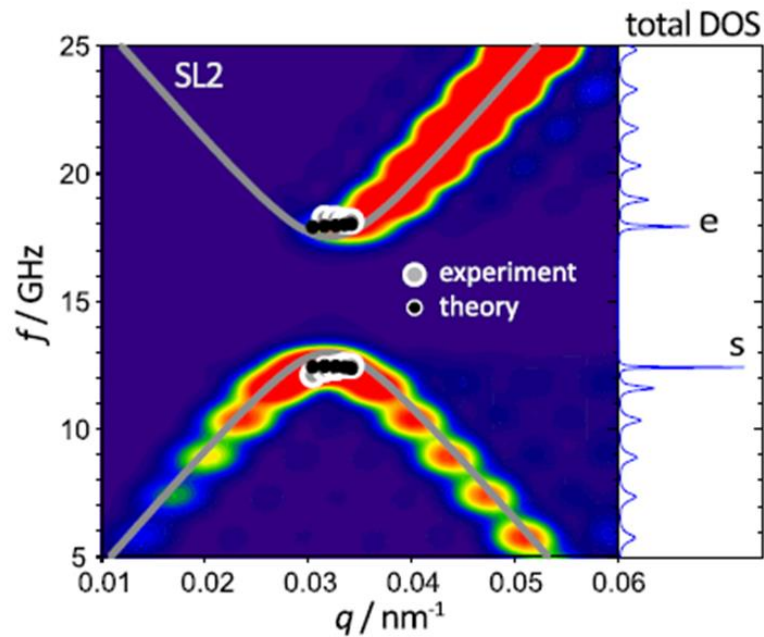
Figure 4.7. *Dispersion relation for superlattice SL2 is shown, with the solid lines indicating the band gap and the white (dark) circles represent the experimental (theoretical) data points. The total DOS shows the appearance of the edge mode and surface mode, which is tuned inside the band gap.*

It is evident from Figure 4.7 that the theoretical studies predicting correlation between *s* mode and surface layer thickness [7] finds good agreement with the experimental results presented in this section. The total DOS shows the appearance of the edge mode (*e*) along with the surface mode (*s*). However, the surface mode in SL2 shifts to 13 GHz as compared to 14 GHz for SL1 and almost overlaps the edge mode (*e$_2$*) as in SL1. This result is in accordance with the theoretically predicted decrease in the frequency of the *s* mode with increasing d_s. The displacement fields of the edge and surface modes are shown in Figure 4.8 (a).
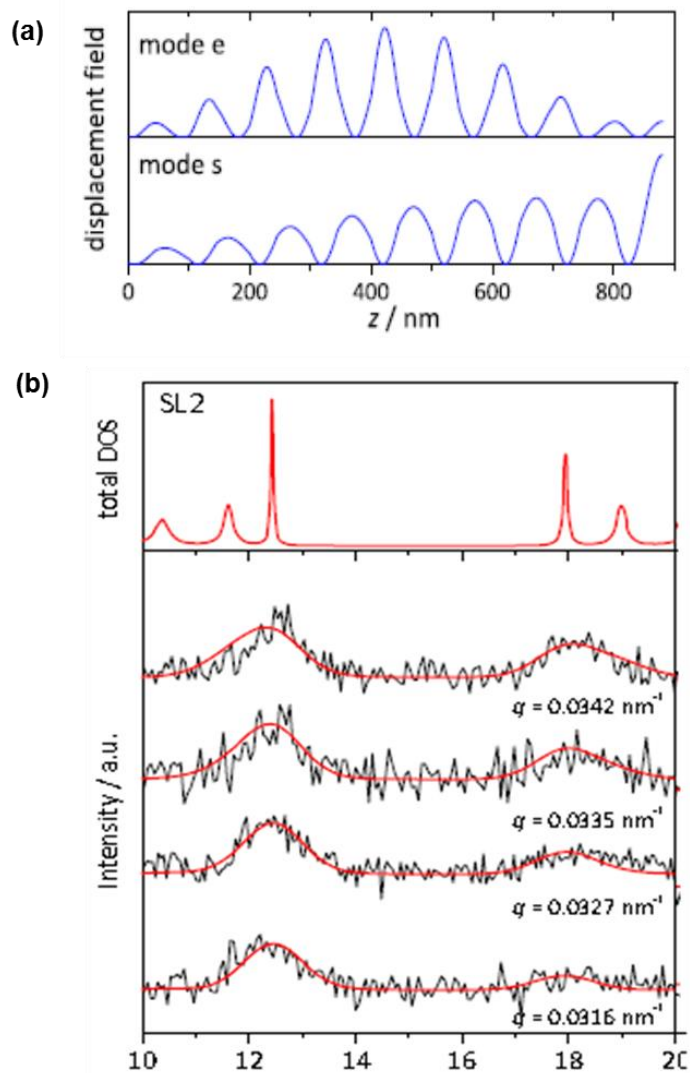
Figure 4.8. *(a) The displacement fields for the edge (e) and the surface mode (s) in SL2 are shown. (b) Total DOS and experimental BLS spectra for four q$_\perp$ values for SL2.*

The displacement fields shown in Figure 4.8 (a) indicate the nature of the two frequency modes in SL2. The upper edge mode (*e*) behaves as a surface avoiding mode (*SAM*) as its amplitude decreases greatly at the surface. On the other hand, the mode at 13 GHz is identified as the surface mode (*s*) as it shows maximum amplitude at the surface. The lower band edge mode is merged with the surface mode in SL2 and slowly decays into the superlattice. The frequency modes are also indicated by the peaks in the BLS spectra at four *q* values shown in Figure 4.8 (b).

4.2.2.2. Interaction of Cavity and Surface Modes

In this section, the presence of cavity defects on the phononic band structure in hybrid superlattices is discussed in detail. Cavity defect layers in a SL represent another class of defects directly affecting the band diagram, in addition to the surface layer defects. Superlattices containing a cavity defect (whether it arises from a new material or a constituent layer of the SL with a distinctly different thickness from the other layers) give rise to a cavity mode (*c*) in the band structure which can interact with the surface mode (*s*).

One of the objectives of this work is to analyze the interaction between the cavity and surface modes which has been theoretically predicted in earlier works. [7] To find experimental evidence, four superlattices consisting of 8 BL of PMMA/SiO$_2$ capped with a surface layer of PMMA are considered. In addition, superlattices SL3, SL4 and SL5 (Table 4.2) possess a cavity defect layer of PMMA with increasing thickness (*d$_c$ ~ 62, 92 and 140 nm*) respectively while SL1 has a usual PMMA layer (*d~ 42 nm*). The thickness of the surface layer is kept constant at *d$_s$ ~ 50 nm*. The cavity layer was introduced at the position of the 9th layer in the superlattice. A schematic of the designed superlattice and the SEM micrographs of the four SLs with defects are shown in Figure 4.9.
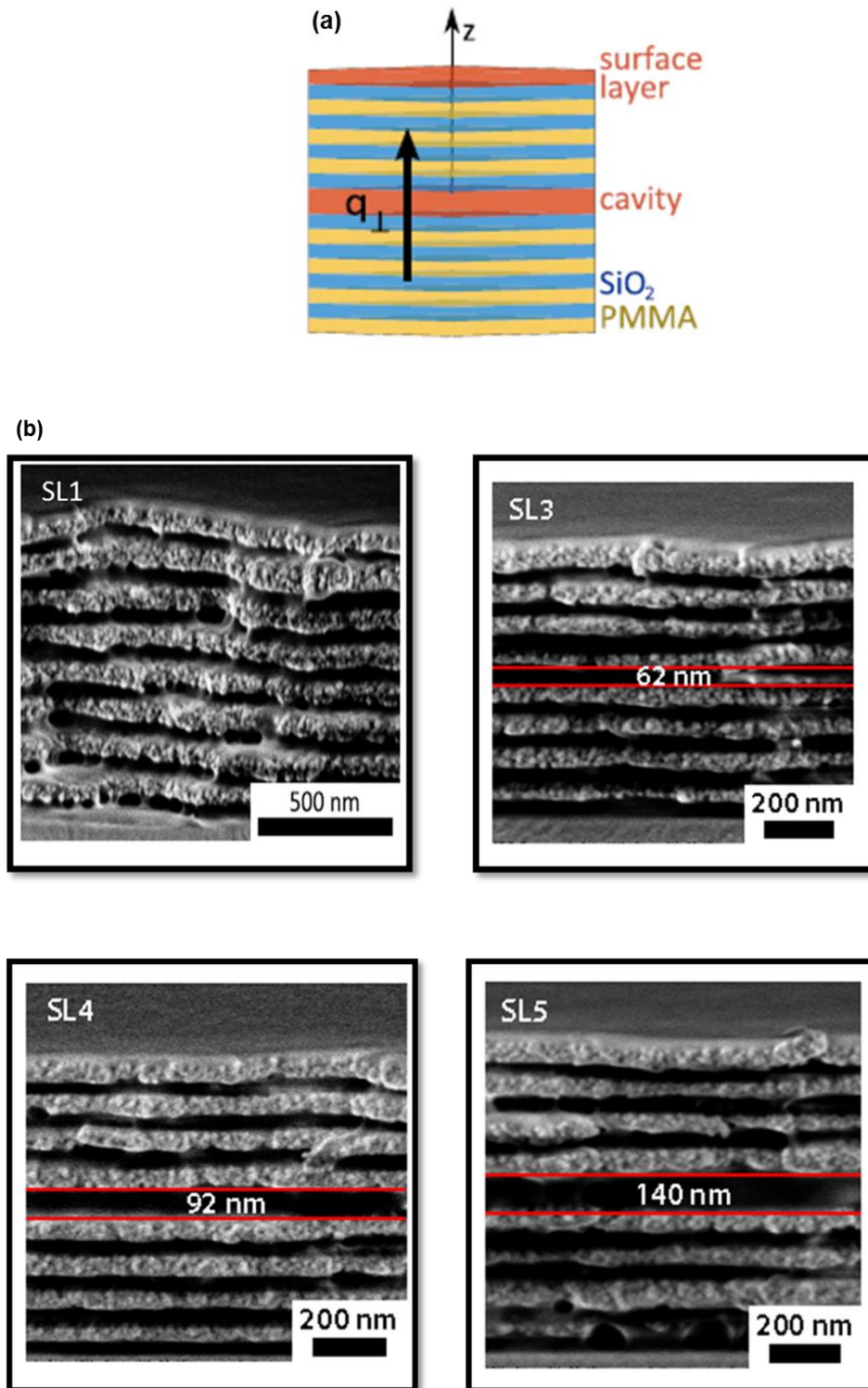
Figure 4.9. *(a) Schematic of a superlattice with cavity and surface defects. (b) SEM images of SL1, SL3, SL4 and SL5 with varying d_c (PMMA) indicated by the red lines.*
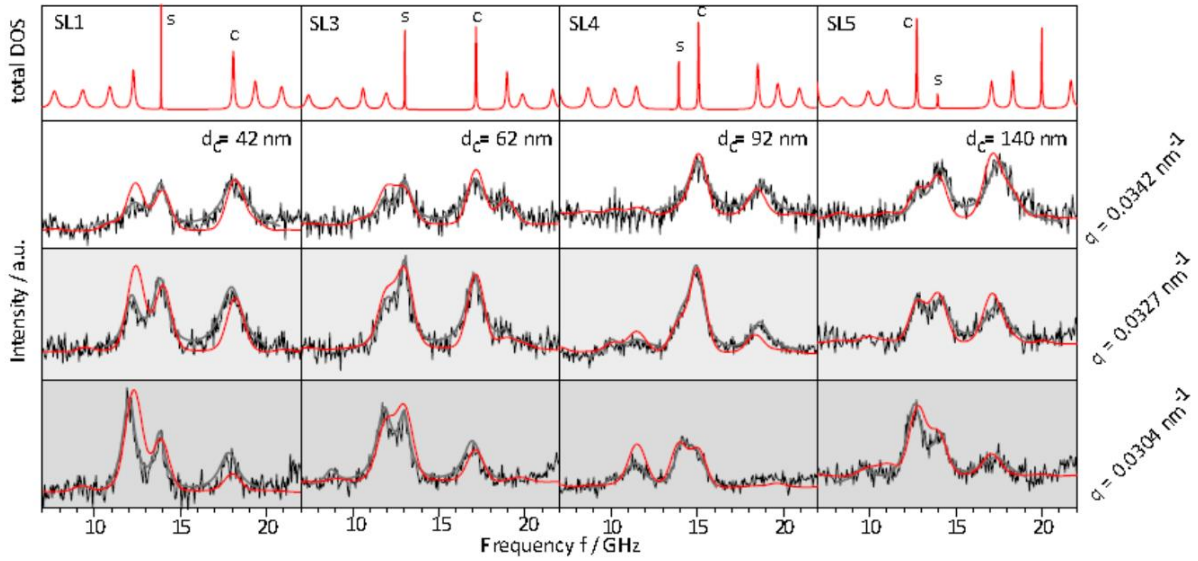
Figure 4.10*. The experimental (theoretical) BLS spectra for the four superlattices SL1, SL3, SL4 and SL5 are shown in black (red) color respectively at three $q_\perp$ values. Only the anti-Stokes wings of the BLS spectra are shown. The density of states is also indicated, depicting the surface and cavity modes.*

The elastic parameters given in Table 4.1 are used to compute the theoretical spectra for four superlattices shown in red in Figure 4.10 while the experimental spectra are in black. It is observed that the experimental and theoretical data show good agreement with each other. The total DOS indicates the position of the surface (*s*) and cavity mode (*c*) which corresponds to ~13 GHz and ~18 GHz respectively for SL3. However, the surface and cavity modes shift closer to each other when d_c is increased to 92 nm in SL4. The cavity mode anti-crosses the surface mode at large cavity thickness ($d_c \sim 140\ nm$) as observed in superlattice SL5. It is evident from Figure 4.10 that the frequency of the *s mode* remains mostly independent of the cavity thickness. On the other hand, the frequency of the *c mode* decreases with increasing d_c and anti-crossing between the two modes occur at large cavity thickness. This phenomenon can be observed clearly in Figure 4.11.
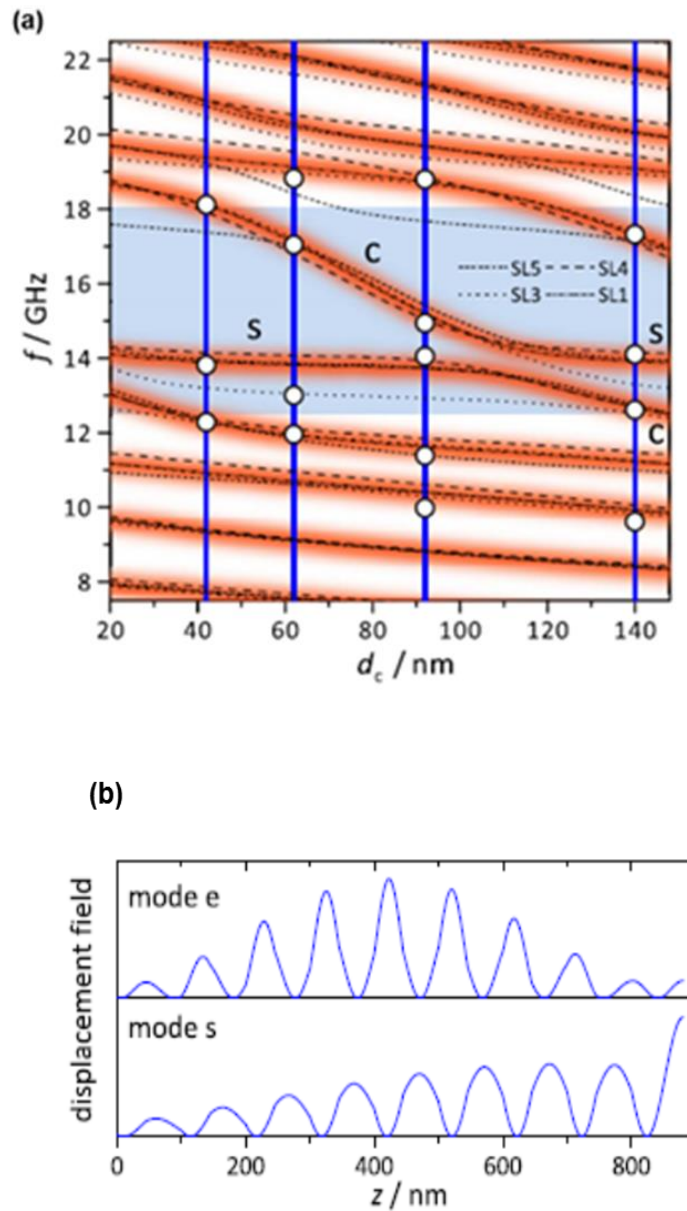
Figure 4.11. *(a) Dispersion of frequency modes around the Bragg gap as a function of the cavity layer thickness, d_c is depicted. The experimental data is indicated by the white circles while the blue shaded portion indicates the band gap area of SL1. The anti-crossing of the s and c modes is clearly observed at large d_c. (b) The displacement fields for the c and s modes indicate the nature of the mode.*

The dependence of the frequency modes s and c on the thickness of the cavity layer (d_c) in superlattices of eight bilayers capped with a PMMA surface layer is shown in Figure 4.11 (a). It is observed that the cavity mode shifts inside the band gap as the thickness of the PMMA cavity in the middle of the superlattice is gradually increased (from SL1 to SL5). The cavity and surface modes come closer at $d_c = 92\ nm$ (in SL4); as a result, there is an interaction between their evanescent fields. This phenomenon eventually leads to an anti-crossing of the two modes (at large $d_c = 140\ nm$ for SL5). Despite the anti-crossing, the two modes retain their distinct character as can be seen from their displacement fields (Figure 4.11 (b)). The cavity mode has its highest amplitude at the center of the SL and acts as a surface avoiding mode (SAM) while the s mode shows a maximum at the surface. These results confirm the earlier predicted theoretical work on the interaction between surface and cavity modes. [7]

4.2.2.3. Effect of High Impedance Surface Layer

Earlier in this thesis, the influence of a PMMA surface defect layer on the phononic band structure in superlattices has been investigated. The PMMA layer has lower elastic impedance compared to the p-SiO$_2$ layer. It has been earlier observed that superlattices capped with a high elastic impedance layer do not show any surface modes. [10, 32] However, surface modes appear for the low impedance layer capped superlattices such as in SL1 and SL2. In this section, experimental evidence of the existence of surface modes in SLs capped with a high impedance p-SiO$_2$ layer is given, provided some conditions are met. The observation of surface mode in such SLs is subject to the condition that the high impedance surface layer is significantly thicker than the standard layers inside the superlattice. In the event of this condition being met, the surface supports a localized mode.

The superlattice considered in this section is SL6 (*Table 4.2*) having a surface SiO$_2$ layer of thickness twice that of the ones present in the SL ($d_s \sim 2\ d_{SiO2}$). The SEM image and the band diagram with associated density of states for SL6 are given in Figure 4.12 (a) and (b).

(a)

(b)
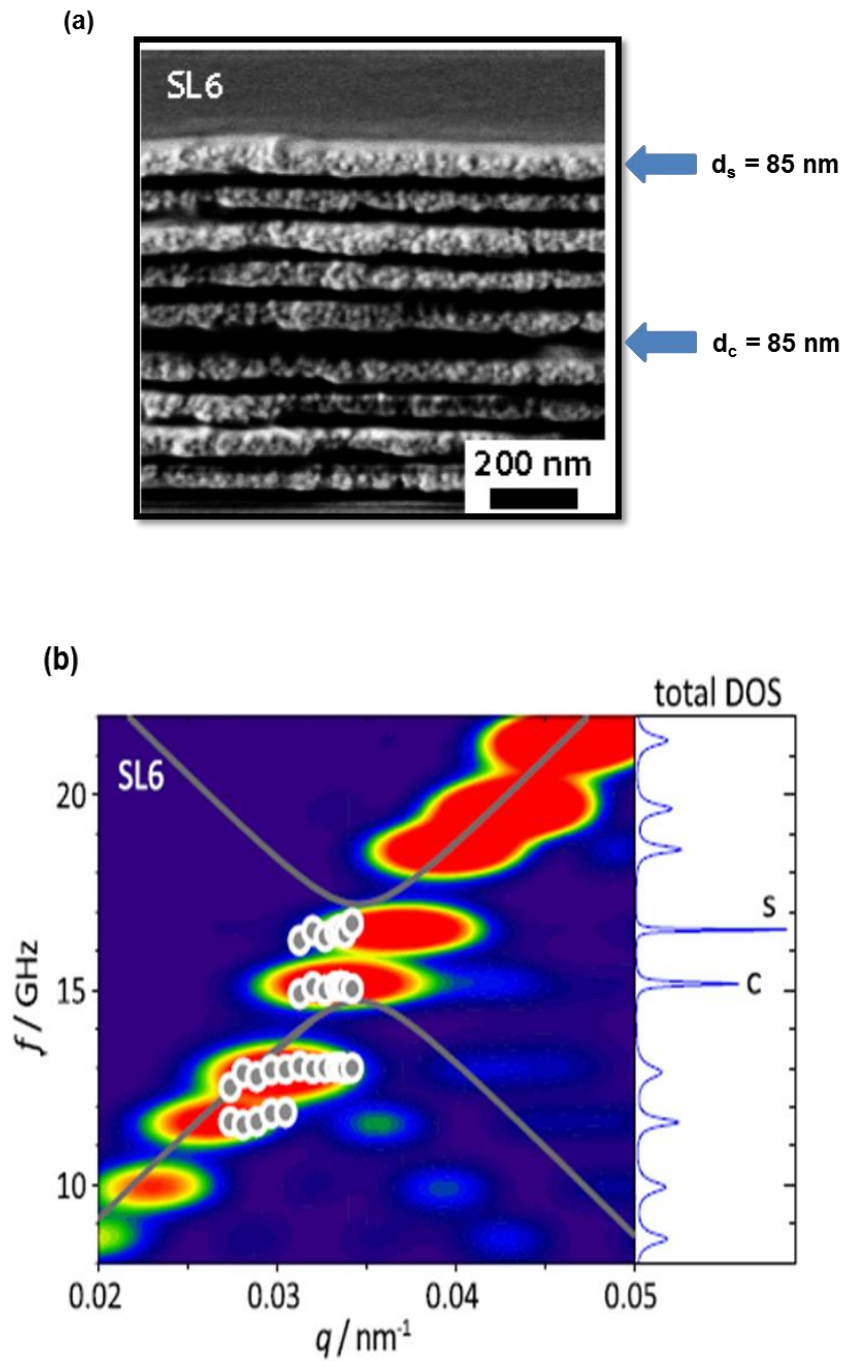
Figure 4.12. *(a) SEM micrograph of SL6 containing a high impedance surface layer of p-SiO$_2$ (d_s ~ 85 nm) is shown. The superlattice also contains a PMMA cavity defect of 85 nm thickness at the 9th layer. (b) Dispersion relation for SL6 showing well-separated s and c modes in the band gap region (confirmed by DOS). Experimental data is shown by white circles.*

The superlattice SL6 supports a cavity layer of PMMA of 85 nm thickness and is capped with a thick high impedance surface layer of p-SiO_2. This makes SL6 different from the previously studied systems that were capped with the PMMA layer. It is observed from Figure 4.12 (b) that despite early studies showing no surface modes for high impedance layers, [32] superlattice SL6 presents two well-defined and separated modes inside the band gap and in the total DOS. The mode at ~ 16.5 GHz is recognized as the surface mode(s) while the cavity mode (c) occurs at ~15 GHz; both modes are identified from their displacement fields. The c mode arises due to the presence of the large PMMA cavity in the middle of SL6.
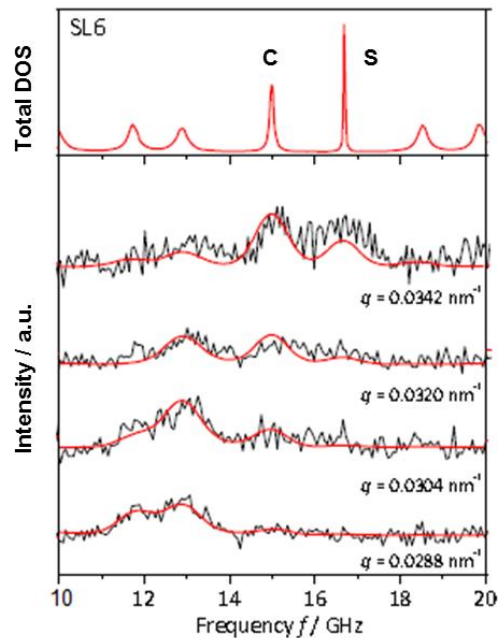
Figure 4.13. *Experimental and theoretical BLS spectra for SL6 are shown in black and red color respectively at four $q_\perp$ values. The total DOS indicates two distinct modes.*

The results obtained from Figure 4.12 (b) present clear evidence of the existence of surface modes for high impedance capped SLs. This also proves the theoretically presented idea [38] that the observation of surface modes relies on the thickness as well as the material of the surface layer. In this case, the surface modes appear only when the thickness of the surface layer is increased greatly from the constituent layers in the SL. Since SL6 contains both the s and c modes, their interaction can also take place,

provided the thickness of the cavity layer is varied sufficiently to allow interaction of theevanescent fields.

4.2.2.4. Semi-Infinite Superlattice

The effect of thickness of a superlattice on the appearance of surface modes in the band diagram has already been discussed in Section 4.2.2.1.1. In this section, the influence of cavity modes on the band structure in thick SLs is discussed to support theoretical predictions. For this purpose, a semi-infinite superlattice SL7 is considered (Tables 4.1 and 4.2) consisting of 20 bilayers with two cavity layers. The cavity layer of p-SiO$_2$ near the glass substrate is 100 nm thick while a PMMA cavity layer is also present in the middle of the SL with a thickness of 85 nm (Figure 4.14).
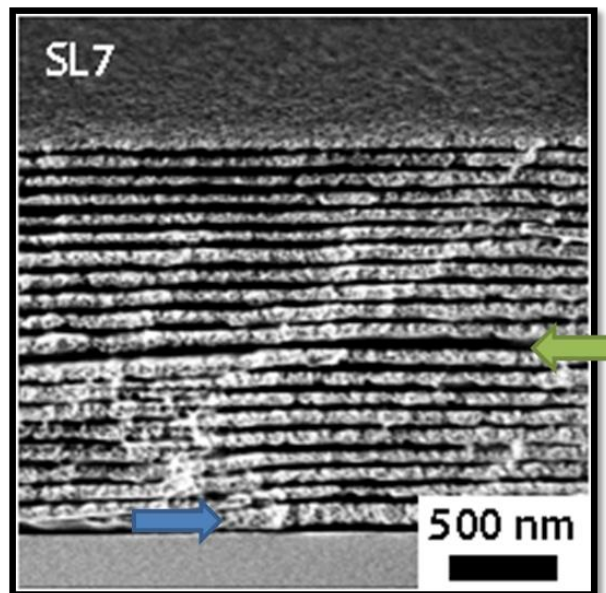
Figure 4.14. *Scanning Electron Micrograph of the semi-infinite superlattice SL7. The silica cavity layer (d_{c1} ~ 100 nm) near the substrate is indicated by the blue arrow while the PMMA cavity layer (d_{c2} ~ 85 nm) is shown by the green arrow in the middle of the SL.*

The elastic parameters of the constituent layers are provided in Table 4.1. This superlattice possesses more than one cavity layers and the effect of the presence of different cavity modes is apparent from the dispersion relation shown in Figure 4.15. The surface layer is of porous silica similar to the standard Bragg stacks A and B described in Chapter 3.
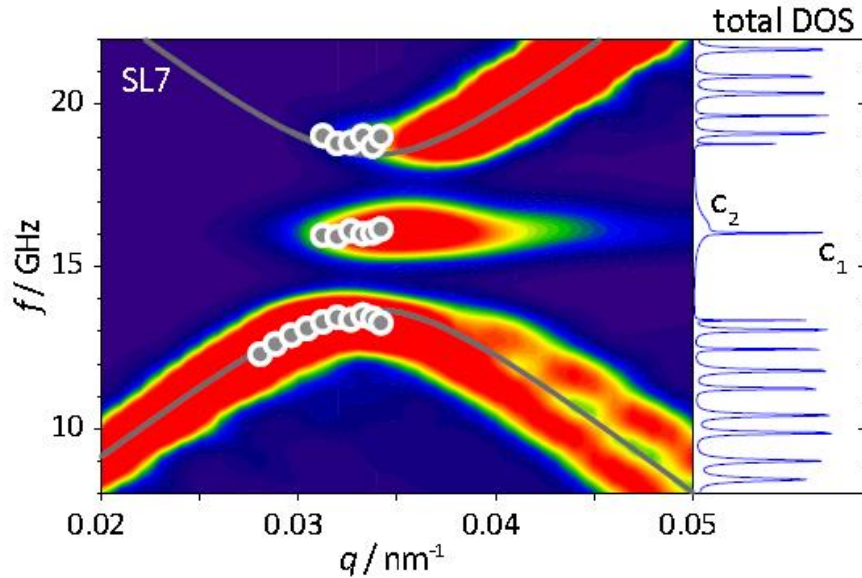
Figure 4.15. Dispersion relation of superlattice SL7, with the colors indicating the intensity of the modes. The DOS also shows the two cavity modes (c_1 and c_2) overlapping each other.

It is observed from Figure 4.15 that the experimental BLS peaks in the 20 BL superlattice SL7 represent the sum of different SL modes since all modes are close to each other as indicated by the DOS. Thus, the band diagram appears to be that of an infinite superlattice having no boundary conditions. The large longitudinal Bragg gap for normal incidence is indicated by the solid grey lines (theoretical) while the white circles show the experimental dispersion. Additionally, a flat mode is seen inside the band gap which is the defect mode. However, the defect mode at 16 GHz is not due to the presence of a surface layer but owes its existence to the cavity layers in the SL. The fine structure due to the PMMA cavity layer (*mode c_1*) is independent of the thickness of the superlattice. DOS shows the presence of a second cavity mode (c_2) due to the silica defect close to the substrate. This c_2 mode couples with the substrate modes resulting from its proximity to the substrate and hence broadens.
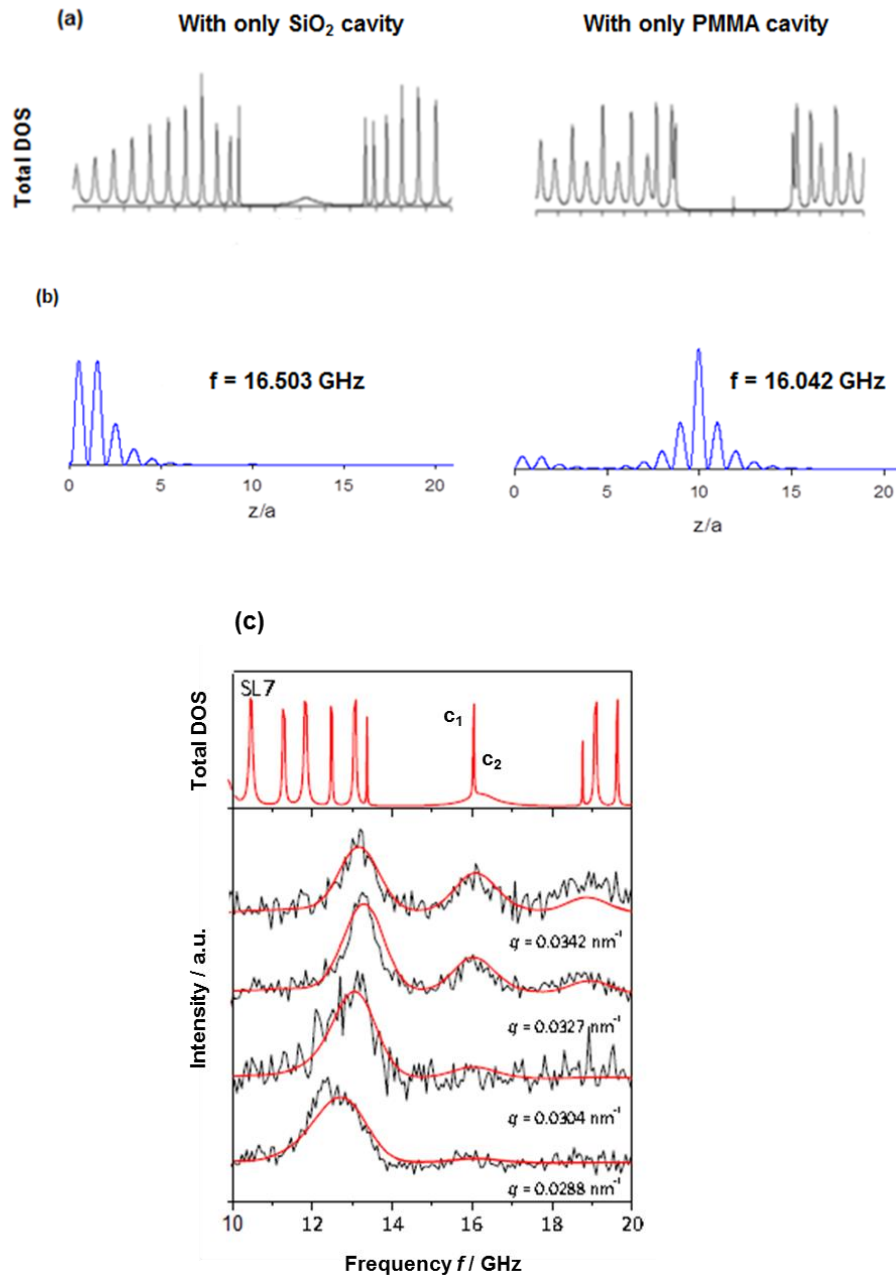
Figure 4.16. *(a) Total DOS calculated theoretically for a SL with only one cavity (SiO_2 or PMMA). The defect mode obtained is not similar to the one obtained in SL7 containing both cavities. (b) The displacement fields of the two cavity modes are shown. The silica cavity is near the substrate while the PMMA cavity is in the middle of the SL. (c) The experimental (theoretical) BLS spectra of SL7 are shown in black (red) at four q values.*

Figure 4.16 (a) assumes a hypothetical scenario for a 20 BL superlattice containing only a silica cavity near the substrate or a PMMA cavity in the middle of the SL. It is observed that in either of the cases, the DOS obtained is not similar to the one for SL7 (shown in Figure 4.16 (c)) that shows two overlapping cavity modes. The displacement fields identify the two distinct cavity modes from each other. It is therefore concluded that in SL7, the flat mode arising at ~ 16 GHz in the band diagram is due to the superposition of the two cavity modes c_1 and c_2. The total intensity of this defect mode requires contributions from both cavity modes.

4.2.3. Evidence of Optical Stop-band

It has been earlier discussed that the phoxonic crystals boast of a photonic band gap as well as a phononic gap. In this section, optical transmission of the superlattices with defects is considered. The Bragg stacks in this study can be considered as phoxonic crystals as they show theoretically presence of an optical band gap at around 290 nm (for SL1). The superlattice is mostly transparent for the optical waves, keeping in mind the small contrast in refractive indices of PMMA and silica. However in a small region around 300 nm, there is a break in transmission corresponding to a photonic band gap. The optical contrast between the substrate, air and the layers of the SL leads to the qualification of this stop band in the defected SLs as an optical cavity (Figure 4.17). The light-matter interaction in these soft matter SLs can, therefore be greatly enhanced.
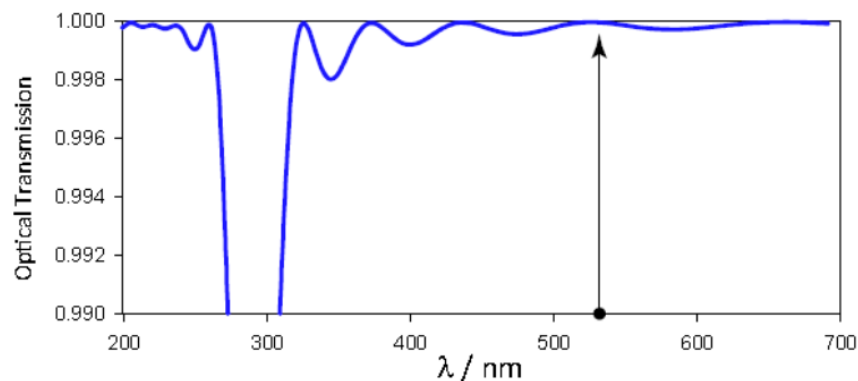
Figure 4.17. *Computed optical transmission in SL1 depicting a photonic band gap at 290 nm. The penetrating wavelength in this experiment is 532 nm, i.e., at a maximum of transmission and is indicated by a black arrow.*

4.3. Conclusions

In this chapter, phonon propagation in hybrid superlattices containing different type of defects has been discussed. The ensuing experimental and theoretical observations have proven that the phononic band structure of hybrid SLs is very sensitive to changes in periodicity. The breaking of high symmetry in the SLs by the introduction of defect layers greatly influences the phonon dispersion and is clearly depicted in an altered BLS spectrum. In this work, the first clear experimental evidence of the existence of surface and cavity modes has been presented, supported by theoretical calculations. The interaction between surface and cavity modes is also clearly documented. A striking effect is the closing of the band gap due to cavity modes inside the band gap which allow transmission. A strong response to layer thickness and sequence is also observed which can lead to phononic devices based on soft matter. Another possible application can come from a dynamic tuning of cavity modes and their interaction with other defect modes under external stimuli. These may involve phase transformation using thermo- or chemi-responsive layers which could be used for detection applications.

Hybrid SLs with defects have been shown to behave as phoxonic structures because of high acoustic and optical contrast in the constituent materials. Therefore, the hybrid soft matter SLs belong to a new class of dual phononic-photonic (or phoxonic) structures that allow for a simultaneous tuning of acoustic transmission in the GHz range and optical transmission in the visible region. These designed superlattices can provide a suitable platform to study acousto-optic interactions.

4.4. Instrumentation

The BLS instrumental set-up is described in detail in Section 2.5.1. The designed superlattices containing defects were imaged on a LEO Gemini 1530 Scanning Electron Microscope (Carl Zeiss AG, Oberkochen, Germany) using an acceleration voltage of 0.7 kV in secondary electrons InLens detection mode. The images were later analyzed using software to determine the layer thickness, periodicity and volume fraction of individual layers. All the measurements were carried out on the same spot on the glass substrate where the laser beam is focused in BLS.

Bibliography

1. L. Esaki and R. Tsu, *IBM J. Res. Dev*. **1970**, 14, 61.

2. V. Narayanamurti, H. L. Störmer, M. A. Chin, A. C. Gossard and W. Wiegmann, *Phys. Rev. Lett*. **1979**, 43, 2012.

3. E. Yablonovitch, *Phys. Rev. Lett*. **1987**, 58, 2059.

4. M. S. Kushwaha, P. Halevi, L. Dobrzynski and B. Djafari-Rouhani, *Phys. Rev. Lett*. **1993**, 71, 2022.

5. J. Sapriel and B. Djafari-Rouhani, *Surf. Sci. Rep*. **1989**, 10, 189.

6. R. Martinez-Salazar, J. Sancho, J. V. Sanchez, V.Gomez, J. Llinares and F. Meseguer, *Nature*. **1995**, 378, 241.

7. E. H. El Boudouti, B. Djafari-Rouhani, A. Akjouj and L. Dobrzynski, *Surf. Sci. Rep*. **2009**, 64, 471.

8. Y. Pennec, J. O. Vasseur, B. Djafari- Rouhani, L. Dobrzynski, *Surf. Sci. Rep*. **2010**, 65, 229.

9. T. Gorishnyy, C. K. Ullal, M. Maldovan, G. Fytas and E. L. Thomas, *Phys. Rev. Lett*. **2005**, 94, 115501.

10. L. C. Parsons and G. T. Andrews, *J. Appl. Phys*. **2012**, 111, 123521.

11. W. Cheng, N. Gomopoulos, G. Fytas, T. Gorishnyy, J. Walish, E. L. Thomas, A. Hiltner and E. Baer, *Nano. Lett*. **2008**, 8, 1423.

12. C. Colvard, R. Merlin, M. V. Klein and A. C. Gossard, *Phys. Rev. Lett*. **1980**, 45, 298.

13. M. Trigo, A. Bruchhausen, A. Fainstein, B. Jusserand and V. Thierry-Mieg, *Phys. Rev. Lett.* **2002**, 89, 227402.

14. W. Cheng, J. Wang, U. Jonas, G. Fytas and N. Stefanou, *Nat. Mat*. **2006**, 5, 830.

15. H. T. Grahn, H. J. Maris, J. Tauc and B. Abeles, *Phys. Rev. B*. **1988**, 38, 6066.

16. H. J. Trodahl, P.V. Santos, G.V. M. Williams and A. Bittar, *Phys. Rev. B*. **1989**, 40, 8577.

17. V. Lemos, O. Pilla, M. Montagna and C. de Souza, *Superlattices Microstruct*. **1995,** 17, 51.

18. N.-W. Pu and J. Bokor, *Phys. Rev. Lett*. **2003**, 91, 076101.

19. M. Trigo, T. A. Eckhause, M. Reason, R. S. Goldman and R. Merlin, *Phys. Rev. Lett.* **2006**, 97, 124301.

20. Y. Ezzahri, S. Grauby, J.M. Rampnoux, H. Michel, G. Pernot, W. Claeys, S. Dilhaire, C. Rossignol, G. Zeng and A. Shakouri, *Phys. Rev. B*. **2007**, 75, 195309.

21. L. Belliard, A. Huynh, B. Perrin, A. Michel, G. Abadias and C. Jaouen, *Phys. Rev. B*. **2009**, 80, 155424.

22. N. D. Lanzillotti-Kimura, A. Fainstein, A. Huynh, B. Perrin, B. Jusserand, A. Miard and A. Lemaitre, *Phys. Rev. Lett*. **2007**, 99, 217405.

23. R. P. Beardsley, A.V. Akimov, M. Henini and A. J. Kent, *Phys. Rev. Lett.* **2010**, 104, 085501.

24. P. Lacharmoise, A. Fainstein, B. Jusserand and V. Thierry-Mieg, *Appl. Phys. Lett*. **2004**, 84, 3274.

25. M. Maldovan and E. L. Thomas, *Appl. Phys. Lett*. **2006**, 88, 251907.

26. B. Liang, X. S. Guo, J. Tu, D. Zhang, and J. C. Cheng, *Nat. Mater*. **2010**, 9, 989.

27. S.-M. Lee, D. G. Cahill and R. Venkatasubramanian, *Appl. Phys. Lett*. **1997**, 70, 2957.

28. Y. K. Koh, Y. Cao, D. G. Cahill and D. Jena, *Adv. Funct. Mater*. **2009**, 19, 610.

29. S. P. Hepplestone and G. P. Srivastava, *J. Appl. Phys*. **2010**, 107, 043504.

30. N. Gomopoulos, D. Maschke, C.Y. Koh, E. L. Thomas, W. Tremel, H. -J. Butt and G. Fytas, *Nano Lett*. **2010**, 10, 980.

31. P. M. Walker, J. S. Sharp, A.V. Akimov and A. J. Kent, *Appl. Phys. Lett*. **2010**, 97, 073106.

32. D. Schneider, F. Liaqat, E. H. El Boudouti, Y. El Hassouani, B. Djafari-Rouhani, W. Tremel, H.-J. Butt and G. Fytas, *Nano Lett*. **2012**, 12, 3101.

33. L. M. Goldenberg, V. Lisinetskii and S. Schrader, *Laser Phys. Lett*. **2013**, 10, 055808.

34. J. He, B. Djafari-Rouhani and J. Sapriel, *Phys. Rev. B*. **1988**, 37, 4086.

35. N. Combe, J. R. Huntzinger and J. Morillo, *Eur. Phys. J. B*. **2009**, 68, 47.

36. P. X. Zhang, D. J. Lockwood, H. J. Labbe and J. -M. Baribeau, *Phys. Rev. B*. **1992**, 46, 9881.

37. M. Trigo, A. Fainstein, B. Jusserand and V. Thierry-Mieg, *Phys. Rev. B*. **2002**, 66, 125311.

38. E. H. El Boudouti, B. Djafari-Rouhani, E. M. Khourdifi and L. Dobrzynski, *Phys. Rev. B.* **1993**, 48, 10987.

5

A Bio-inspired Design of Ultrastrong Multilayers

Corresponding Publication:

Faroha Liaqat, Muhammad Nawaz Tahir, Michael Kappl, Günter K. Auernhammer, Dirk Schneider, Kookheon Char, George Fytas, Hans-Jürgen Butt and Wolfgang Tremel,

bioinspired Fe$_3$O$_4$ NPs/mussel polymer composite
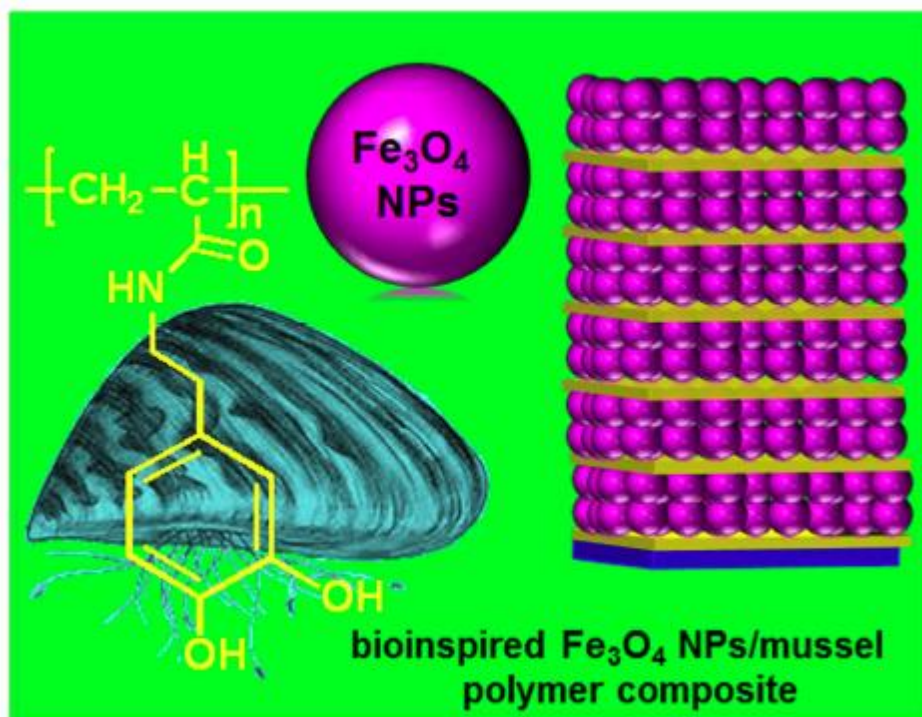
5.1. Introduction

Nature offers a variety of exemplary materials noted for a significant structural hierarchy [1] on different length scales. Structural biomaterials show a tendency to utilize hard and soft basic components in a design that gives multifunctional characteristics to the whole system. The order and sophisticated structures found in biological materials is one of the fundamental reason behind the exceptional characteristics regularly observed in living organisms. Many materials in nature combine disparate properties such as exceptional strength, toughness and extensibility, mutability and a functionality that is unmatched by most man-made materials. [2-5] Unique properties in biomaterials emerge often from the intelligent use of simple and abundant constituents which possess adaptability for changing environmental conditions through various feedback loops.

There are many examples of natural systems composed of relatively weak constituents. In contrast, the current artificial materials exhibit an inferiority in properties that arises out of a scarcity of material quality and availability as well as energy. Many composite biological materials make the most of the properties of their constituents from their elaborate structures. Nacre from seashells is a textbook example showing how evolution can lead to a high performance material from relatively weak constituents. [6] It has a high mineral content (~95%) and 5 % proteins in a brick and mortar structure that possesses high values of elastic modulus (from 40-70 GPa). This phenomenon of an efficient design coming from a combination of hard and soft building blocks to form a multi-level hierarchical structure makes the biological materials excellent performers. A hard mineral component serves as the reinforcing part and the soft biopolymer allows for dissipation of energy. The morphology of the mineral blocks and the interactions holding together the components provides a physico-chemical basis for stiffness and flexibility at multiple scales, leading to an increased robustness against catastrophic materials failure. [7, 8]

Structural materials in nature which make extensive use of the structure-property relationship to boost their strength, extensibility and load-bearing capability include bone, teeth, nacre, beetle cuticles and sea-sponge exoskeletons. [2, 9, 10] Figure 5.1 cites some examples of some hierarchy in biological materials found in nature.
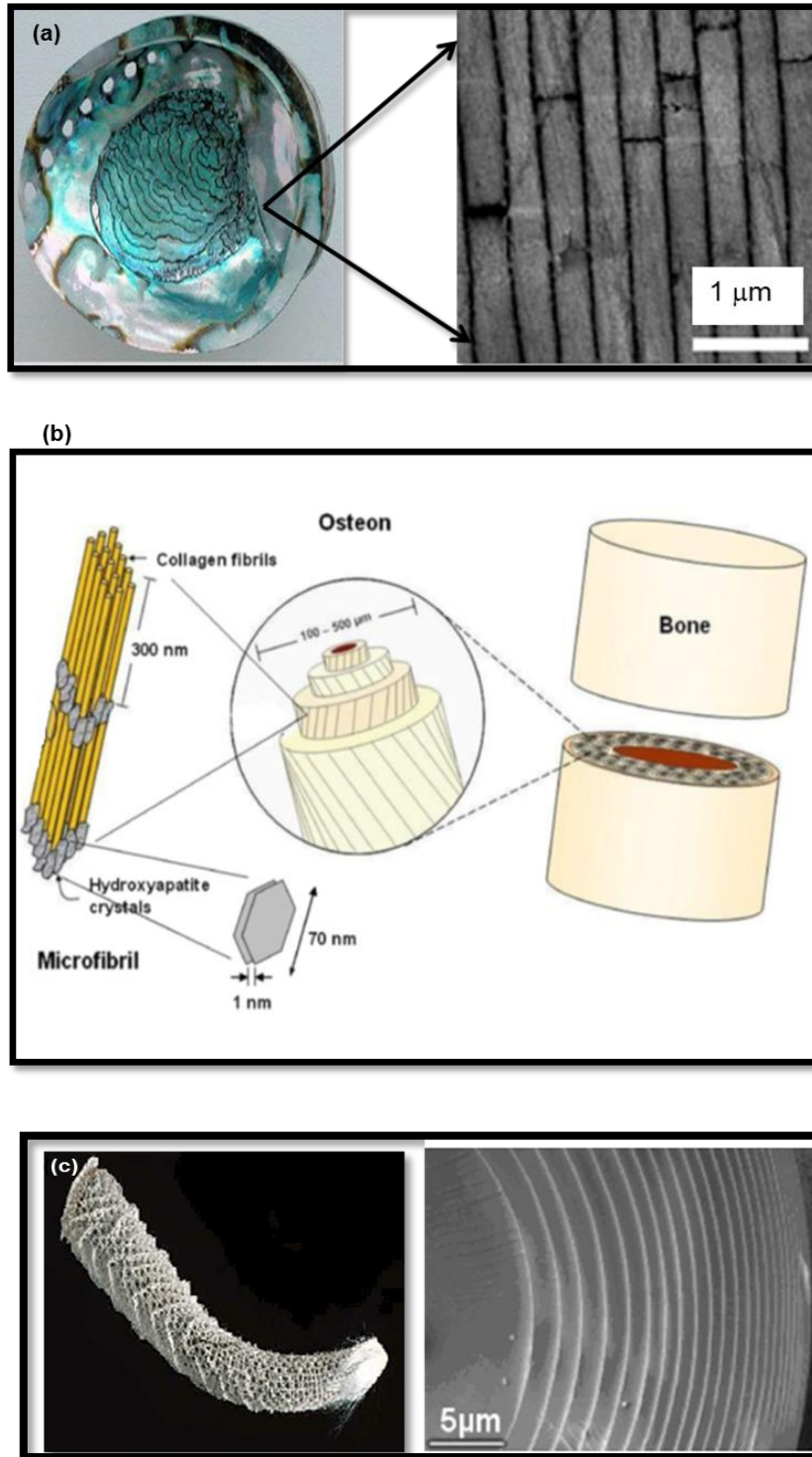
Figure 5.1. (a) The brick and mortar structure of nacre in the abalone shell. The aragonite tablets are held together by thin bio-polymer and mineral bridges. (b) Hierarchy in bone [9] (c) Structural analysis of a spicule in Euplectella sponge [10]

The hybrid materials involved in the sophisticated designof many natural organisms can serve as models for artificial materials with multifunctional properties. The idea of mimicking biological tough structures has stimulated research to replicate the complex designs found in nature and modify them to produce functional materials with exceptional properties. Several attempts have been made to emulate nature in the fabrication and morphology of synthetic bio-nanomaterials. [11-13] The creation of artificial materials with their intricate microstructure is a challenge that requires both the design of optimum microstructures and the development of fabrication procedures to implement these designs.

The methods employed to achieve biomimetic strong hybrids have been numerous; for instance, atomic layer deposition (*ALD*) has been used to infiltrate the inner protein structures of biomaterials (such as spider silk) with metals to obtain greater toughness. [14] Low temperature chemical bath deposition of titania and poly-electrolytes has been a method employed to yield laminates mimicking nacre's tough hierarchical structure. [15] An effective way to build sophisticated bio-inspired architectures has been freeze-casting which produces porous layered materials filled in afterwards to form a tough nano-composite. [16] Apart from ice-templating, [17] other approaches to obtain nacre-mimic structures include single-step electrophoretic co-deposition [18] as well as self-assembly induced by electric field to obtain nano-composites. [19] However, these synthetic engineering techniques are mostly time-consuming, expensive and plagued with problems of agglomeration of nanoparticles and complex fabrication. Other sequential deposition techniques involve ordered multilayered organic/inorganic composite structures obtained via a simple dip-coating approach. [20]

Layer-by-layer (*LbL*) assembly of alternating hard and soft components has also been frequently employed [11, 15, 21, 22] to obtain composites such as the ones based on calcium carbonate through repeated calcium carbonate crystallization onto a film of charged molecules. Although LbL techniques have been extensively used to obtain hybrid materials, they have the disadvantage of requiring long time periods for the deposition of a large number of layers. It is therefore imperative to devise a method that has the ability to form hierarchical structures in a short time with a high degree of control. As the earlier part of this thesis demonstrates, hybrid superlattices with controlled layer thicknesses and minimum surface roughness have been fabricated by high speed spin-coating. The current chapter focuses on using a similar method to produce multi-

layered stacks of hard and soft components, designed to show high strength similar to bio-materials.

In bio-materials like nacre which show exceptional strength, the hierarchical structure consists of a soft polymer matrix and a hard mineral part, arranged in a sophisticated assembly. The inorganic hard component of the hybrid provides the strength while the polymer acts as an adhesive that binds the inorganic components together and accounts for energy dissipation. Keeping this model in mind for the multilayered system described in this thesis, the choice of the right components required to improve mechanical properties of the hybrid becomes crucial.

The structural and physical properties of the composites can be modified by varying the polymer [23] or the mineral components. In order to have an efficient and stable assembly of nanoparticles in a polymer matrix, it is important for the polymer to have functional groups that bind to the nanoparticle surface. [24] Nature provides inspiration for such binding groups; marine mussels are able to stick to wet surfaces with the aid of specialized adhesion proteins with a high content of the catecholic amino acid 3, 4-dihydroxyphenylalanine (DOPA). [25-26] (Figure 5.2) These mussel adhesive proteins act as cement to attach the animals to the surfaces and scientists have exploited this property of DOPA to make synthetic adhesive coatings. [27-28] DOPA has been extensively used in combination with several functionalized nano-materials to produce functional materials, with special focus on its ability to coordinate to transition metal ions such as Fe^{3+}. [29-30]
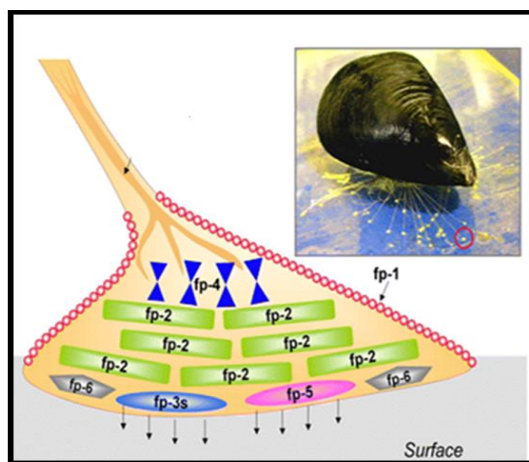
Figure 5.2. A mussel attached to a mica sheet is shown. The enlarged schematic drawing describes protein distribution in the byssal threads of marine mussels. [31]

In this work, two types of materials from nature act as inspiration; the hierarchical structure of nacre composed of soft and hard components and the adhesive character of DOPA derived from mussel foot proteins. Nanoparticles and DOPA-polymers represent suitable candidates for designing multilayered hybrid structures based on inspiration from nature. Iron oxide nanoparticles have been selected as the hard inorganic component in the multilayers based on the affinity of DOPA to Fe^{3+}, whereas a DOPA based polymer has been used as the matrix to cement the nanoparticles. This multi-layered system of DOPA and Fe_3O_4 nanoparticles serves as a model for strong and adhesive hybrid superlattices. The polymer-nanoparticle assembly of this designed Bragg stack has promising applications in hard and adhesive coatings based on its unique structure-property relationship.

5.2. Results and Discussion

5.2.1. Fabrication of Hybrid Multilayers

This section describes in detail the procedure of building up multilayers of iron oxide (*Fe₃O₄*) nanoparticles (*NPs*) and a DOPA based polymer (*P*). The iron oxide nanoparticles were synthesized with some small alterations to the synthesis reported by Sun et al. [32] Briefly, iron acetyl acetonate (2 mmol) was mixed in benzyl ether (20 mL) with 1,2-hexadecanediol (10 mmol), oleic acid (6 mmol), and oleylamine (6 mmol) under argon atmosphere and heated to 200 °C with heating rate of 5°C/min. The reaction contents were stirred at this temperature for 30 min followed by increasing the temperature to reflux at 280 ˚C for another 30 min. The dark brown mixture was cooled to room temperature and later precipitated from the solution using ethanol. The magnetite nanoparticles thus produced have a size of 4 nm and are monodisperse, as confirmed from images taken using tunneling electron microscopy (TEM) (Figure 5.3(a)).

The soft component in the multilayered stacks is a DOPA containing polymer which is responsible for strong adhesion to surfaces and the magnetite NPs using its catechol functional groups. The DOPA containing polymer (*P*) was synthesized by method previously reported by Tahir et al., [33] and explained in Schemes 5.1 and 5.2. It is based on a pre-polymer obtained by free radical polymerisation and contains active ester side groups (*Scheme 5.1*). [34] The active ester polymers based on pentafluoro-phenylacrylates were used due to their high solubility and reactivity. Gel permeation chromatography (*GPC*) analysis of the obtained polymer (tetrahydrofuran, light scattering detection) gave the following values: Number average molar mass, Mn = 16,390 g/mol, with a poly dispersity index, PDI = 1.39, having 70 repeating units on average. This pre-polymer was used for the synthesis of multifunctional poly (acrylamide).
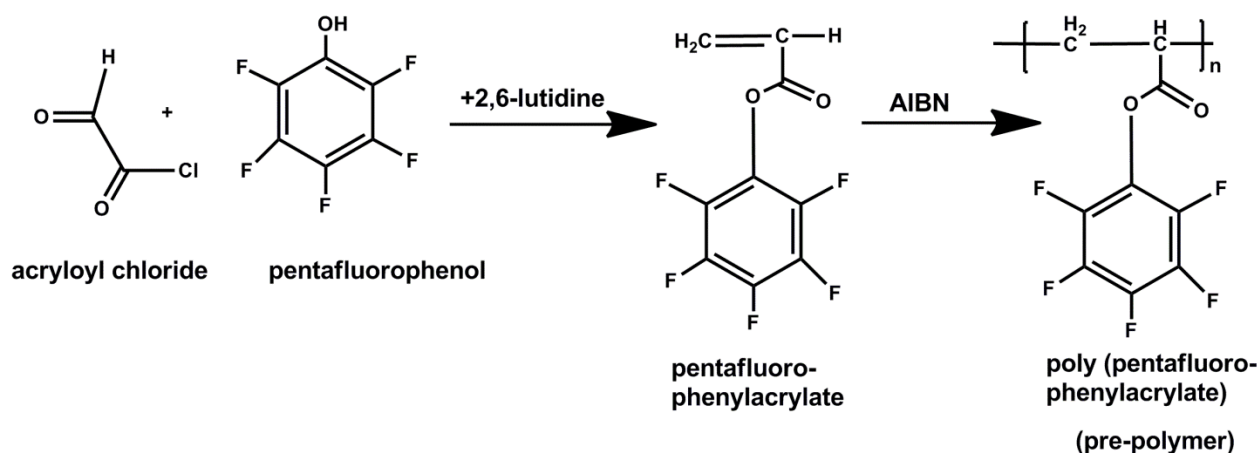
Scheme 5.1. *Synthesis of the poly (active ester) poly (pentafluoro-phenylacrylate) (PFA).*

This pre-polymer was then transformed into the DOPA polymer by a 100% replacement of the active ester groups with 3-hydroxytyramine anchor groups. [33] The poly(active ester) PFA (700 mg, 2.94 mmol repeating units) was dissolved in a mixture of 12 mL of dry dimethylformamide (DMF) and 0.5 mL of triethylamine. The next step was adding 3- hydroxytyramine hydrochloride (555 mg) dissolved in 3 mL of DMF and 0.5 mL of triethylamine to the mixture and the final contents were stirred for 6 hours at 50°C. The solvent was evaporated using rotary evaporator and product was re-dissolved in about 3 mL acetone: water (3:1) and precipitated in water as illustrated in Scheme 5.2. The precipitated polymer was re-dissolved in a mixture of acetone (3 ml) and methanol (1 ml) and again precipitated in excess of water. The precipitated polymer was centrifuged (9000 rpm, 10 min and room temperature) and the solvent was decanted. The process was repeated until 800 mg of colourless solid polymer was obtained on drying.

poly (pentafluoro-phenylacrylate)
(pre-polymer)

i) 3-hydroxytyramine
ii) triethylamine
iii) 50°C
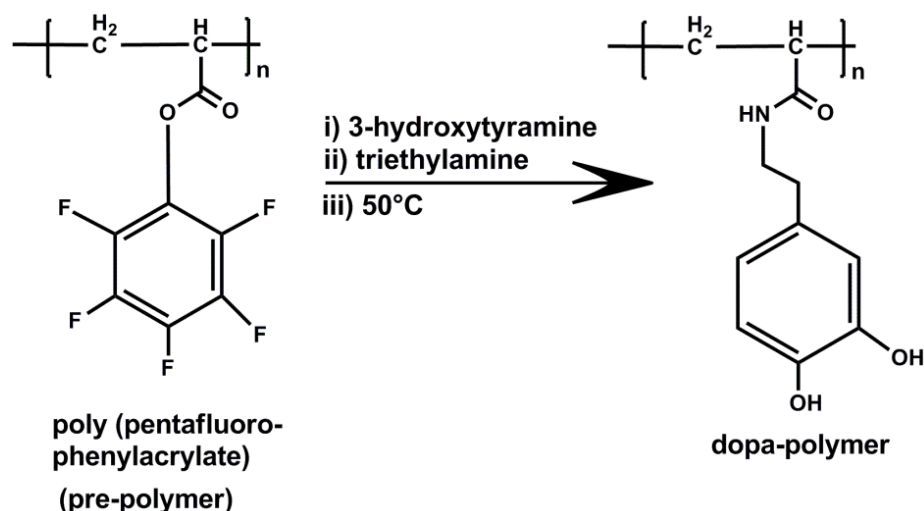
dopa-polymer

Scheme 5.2. Synthesis of the DOPA Polymer (P)

The polymer poly (pentafluorophenyl acrylate) and the catechol polymer were characterized using ^{1}H and ^{19}F NMR spectroscopy (Figures 8.2 and 8.3 in the Appendix). It has been shown that the functionality of this polymer can be tuned and the influence of binding site density has been investigating proving its adhesive character. [35] The catechol groups in the polymer have been investigated extensively for affinity to 3d transition metals and their crucial role in marine mussel adhesion. [36, 37]
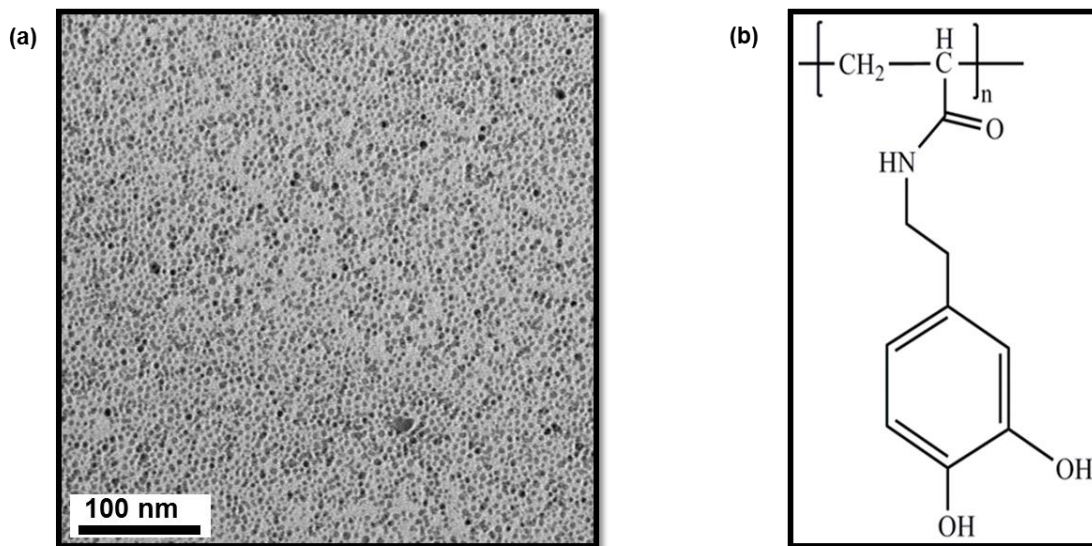
Figure 5.3. *(a) Tunneling Electron Micrograph (TEM) of iron oxide nanoparticles indicating mondisperse Fe_3O_4 NPs of ~4 nm in diameter. (b) The structure of the DOPA containing polymer is shown. The weight average molar mass of the polymer is 16 Kg/mol.*

The preparation of hybrid Bragg stacks of DOPA-polymer and Fe_3O_4 nanoparticles involves a high speed spin-coating procedure similar to the one employed in fabricating 1-D phononic crystals. The multi-layers are assembled on a glass substrate or silicon wafer pre-cleaned in acidic piranha solution of concentrated sulphuric acid (H_2SO_4) and hydrogen peroxide in a volume ratio of 2:1 by consecutive spin coating of the catechol-polymer solution in dimethylacetamide (DMA) and Fe_3O_4 NPs dispersion in hexane, starting from the catechol-polymer layer due to its high affinity and adhesion to the substrate. The thickness of the layers is controlled by optimizing the concentration of the solutions to be spin-casted while the optimized spin-coating parameters are:

Speed: 5000 rpm

Acceleration: 5040 rpm/s

Time: 10 s

An important factor to be considered during fabrication is a solvent mismatch between the organic and inorganic layers. Miscible solvents do not facilitate phase-separated layers but lead to a composite. Therefore, the nanoparticles are dispersed in a low-boiling solvent such as hexane that is immiscible with DMA, which is the solvent required for a clear polymer solution.

The fabrication scheme describing the spin coating process is shown in Figure 5.4. Since the concept of this work is inspired from the structure of nacre, the multilayers were designed to contain a lower organic content compared to the inorganic component. A 2 % polymer solution in DMA was used for spin-coating (Figure 5.4 (A)) while the alternating iron oxide layers are casted from a dispersion of 600 mg of nanoparticles in hexane (Figure 5.4 (B)). The catechol-polymer strongly binds itself to the metal oxide nanoparticles due to the under-coordinated surface atoms because the redox-active behavior of 1, 2-dioxolene groups and the resulting covalency cause high affinity of catechol groups to the Fe surface sites. [38] As subsequent cycles of spin coating take place, the polymer seeps through the porous iron oxide NPs layer (Figure 5.4 (C)) and the catechol groups present in the polymer form a cross-linked network with the Fe_3O_4 particles, thereby cementing the composite structure.

In this work, a multilayered structure of 12 alternating layers of polymer and Fe_3O_4 NPs (Figure 5.4 (D)) is considered for structural characterization and nanoindentation experiments. During the process of assembling the stacks, each layer was subjected to heat treatment at 120 °C for 15 minutes. This is an essential feature of the fabrication process as it has been observed that the process does not yield multilayers without any repetitive heat treatment but rather yields a blend. Additionally, fast heating or high temperatures lead to the formation of cracks and non-uniform structural films. These parameters are carefully optimized to ensure and sustain the multilayered structure. The multilayers show structural color due to multilayer interference (Figure 5.5).
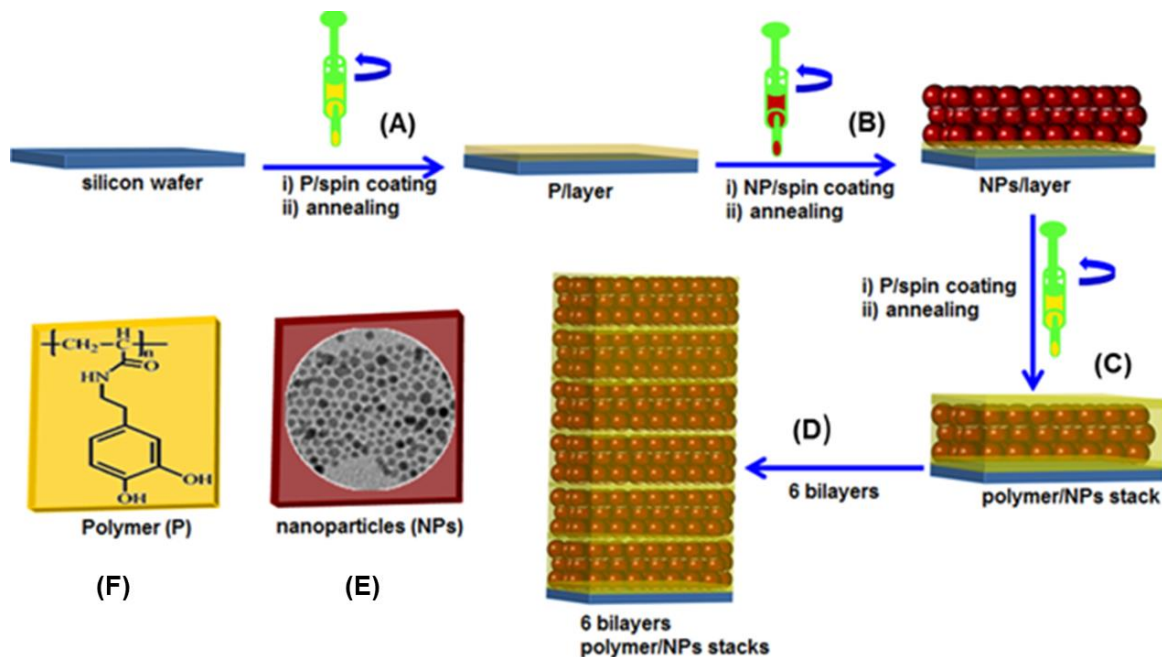
Figure 5.4. *Scheme of fabrication. The DOPA-polymer and the metal oxide nanoparticles are assembled on a silicon wafer by consecutive spin-coating of a dilute polymer solution and nanoparticle dispersion (Steps A and B). The polymer infiltrates the vacancies of the close-packed nanoparticle layers and cross-links the metal oxide nanoparticles to form a strongly interconnected network (C). Twelve subsequent spin casting cycles of the polymer (F) and the nanoparticles (E) were performed in order to build up polymer/nanoparticle multilayers (D).*
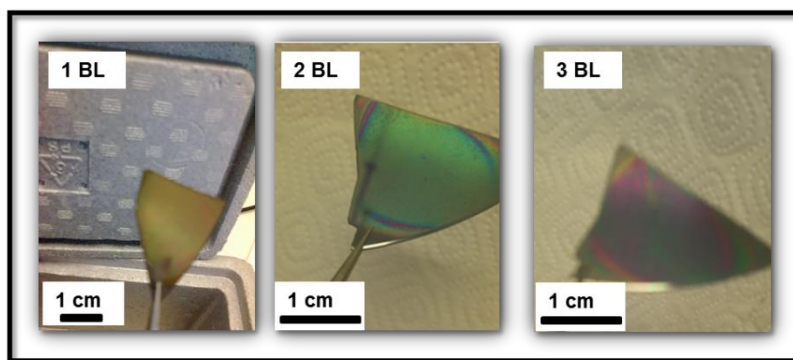
Figure 5.5. *Structural color changes are observed on increasing the number of bilayers (BL) during spin-coating of polymer/Fe_3O_4 superlattice.*

The multilayers of DOPA based polymer and iron oxide nanoparticles assembled by the method described in Figure 5.4 are stable over a large time period (~ 8 months) and can be built up on a variety of substrates such as silicon wafer, glass substrate, quartz or poly (dimethylsiloxane) (PDMS). This is in part due to the ability of DOPA to bind to chemically different surfaces through a variety of interactions. [39]

5.2.2. Characterization

Superlattices of DOPA polymer and iron oxide nanoparticles, (DOPA-polymer/Fe_3O_4)$_6$ are used for physical characterization and determination of mechanical properties where the subscript (6) signifies the number of bilayers. The foot proteins in marine mussels are rich in DOPA content and plays the role of cement in adhesion of animals to wet surfaces. In this work, the DOPA rich polymer plays a similar role, as it seeps through the porous iron oxide layers during repeated spin coating cycles. As a result, the polymer layer reduces in thickness to ~4 nm (Figure 5.10), as the penetrated polymer cross-links the Fe_3O_4 nanoparticles. This can also be seen clearly in the TEM image (Figure 5.6) that shows a highly cross-linked network of iron oxide nanoparticles embedded in the polymer matrix. Long range ordering is also observed in the hybrid which contributes effectively to the remarkable mechanical properties of these structures, as described later in the chapter.

As reported before, the complexing ability of DOPA greatly enhances the mechanical properties and strength of the hybrids. [25] The choice of Fe_3O_4 nanoparticles as the inorganic medium in these hybrid multilayers is a further strength booster, as the coordination of iron ions with DOPA is well-documented. [40] The extent of coordination also depends on the pH of the medium, as well as the amount of iron present. [41] At basic pH values, the oxidation of DOPA is possible leading to self-cross-linking. In this case, the experiments are performed at a pH value of 8.0.
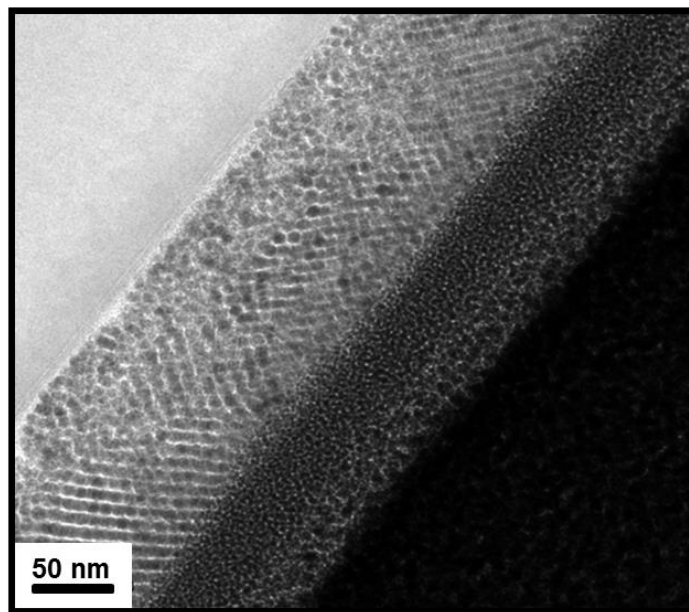
Figure 5.6. *The TEM image of the DOPA polymer/Fe₃O₄ nanocomposite shows a highly cross-linked network, formed due to penetration of the polymer into the nanoparticle framework. The scale bar is 50 nm.*

The cross-linking observed in Figure 5.6 highlights the fact that the iron oxide nanoparticles are closely packed and DOPA acts as an anchor to the NPs as well as linking polymer chains. For a polymer chain containing approximately 80 monomer units and particles of 4 nm in diameter, each metal oxide nanoparticle will be bound to several hundred catechol anchor groups. Ultimately, the bonding at the interface and subsequent infiltration of the polymer in the nanoparticle layers leads to the formation of a tough oxide hybrid structure with the polymer acting as glue, as demonstrated by the mechanical properties of these hybrids (described later in this chapter). A wide range of multicomponent morphologies are feasible due to the facile processibility of the method.

The Energy Dispersive X-ray (*EDX*) spectroscopy of the multilayered DOPA polymer/Fe₃O₄ Bragg stack reveals high iron content (~400 counts) as shown in Figure 5.7 (b). The associated TEM image of the multilayers depicted in Figure 5.7 (a) indicates the two points on which the

EDX analysis was carried out. Figure 5.7 (b) describes the EDX analysis of the multilayers, showing point 1 rich in iron content while point 2 indicates a high platinum (Pt) content due to the Pt coating involved in making a lamella for the analysis. The TEM image clearly depicts the long range ordering present within the hybrid structure.
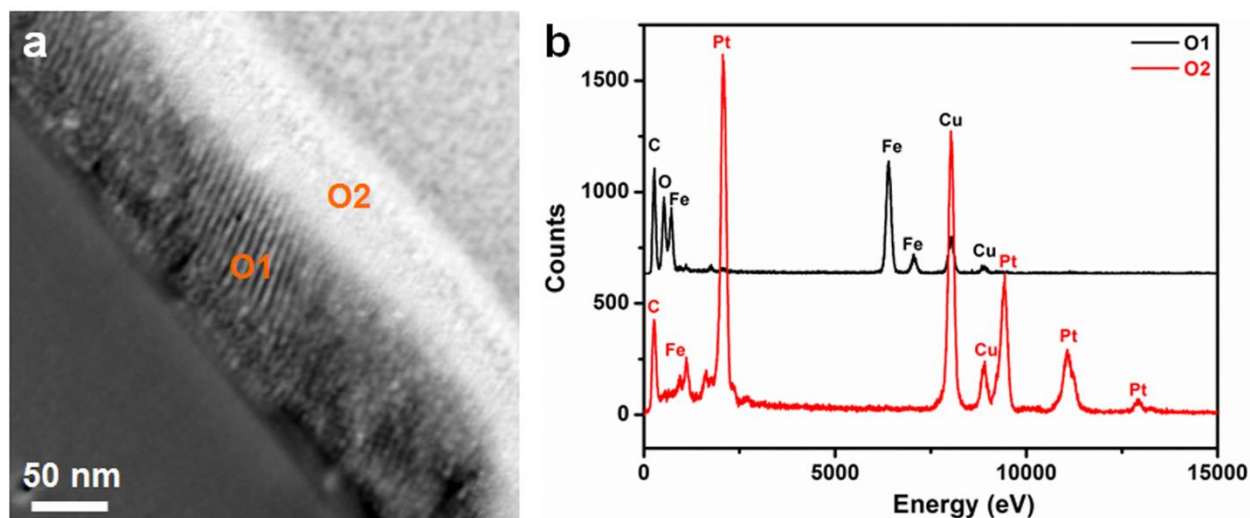
Figure 5.7 *(a). TEM image of the hybrid DOPA/Fe$_3$O$_4$ multilayers. The two points (1 and 2) indicate the position of EDX analysis given in (b). High iron content is observed at point 1 within the cross-linked network while the point 2 represents the platinum coating done to prepare the sample for EDX analysis. The scale bar for the TEM image is 50 nm.*
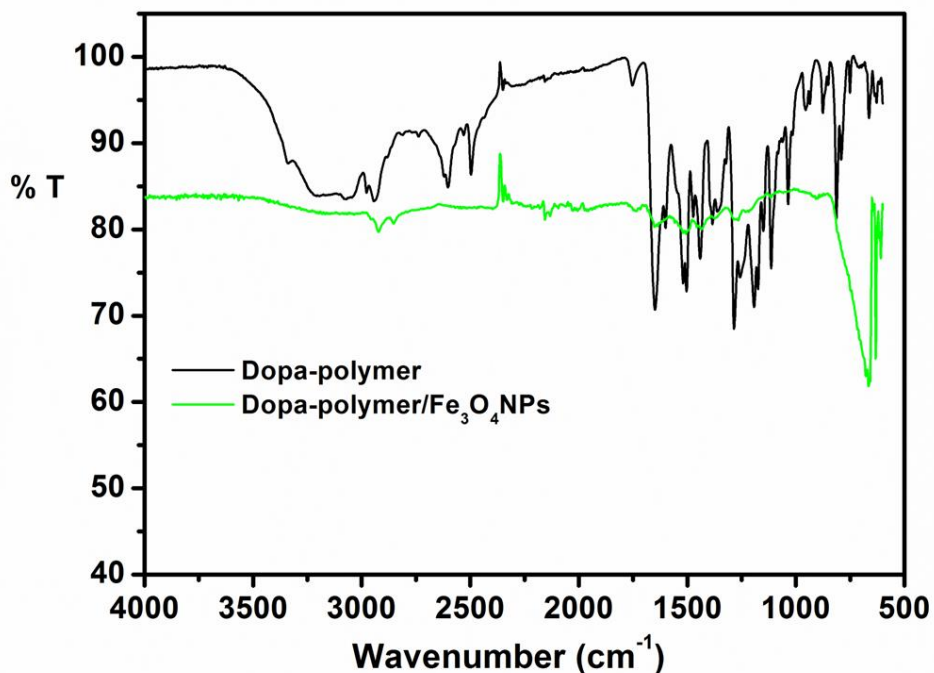
Figure 5.8. *Comparison of the FTIR spectra of pure DOPA-polymer (black) and its hybrid with Fe3O4 NPs (green). The binding between the polymer and iron oxide NPs is evident from the absence of the phenolic –OH stretching in the polymer-nanoparticles hybrid.*

The DOPA polymer /iron oxide nanoparticles hybrid is analyzed by Fourier Transformtaion Infrared (*FTIR*) spectroscopy, after sample preparation by a simple experimental procedure. The FTIR spectra of the pure polymer (black) and the hybrid (green) are shown in Figure 5.8, clearly depicting the binding of the catechol groups of the polymer to the iron oxide NPs. The FTIR spectrum of the hybrid films shows almost all prominent bands; in particular, the C-O vibrations are slightly shifted to lower wavenumbers. The binding of the –OH groups of the polymer to the metal oxide nanoparticles can be traced to the absence of the hydroxyl group stretch in the hybrid (broad band extending upto 3600 cm^{-1} and 1320 cm^{-1} in the pure polymer). A strong band centered at 664 cm^{-1} confirms the formation of complex between the iron center and catechol groups of the polymer.

The Raman spectra of the unbound DOPA-polymer (black) and the hybrid films (red) are shown in Figure 5.9. The multilayers coated on glass substrate are used to measure the Raman spectra for the hybrid. Raman studies of the multilayers confirm the binding of the catechol units to the metal oxide DOPA-iron coordination as the major factor responsible for the strength of the hybrids.
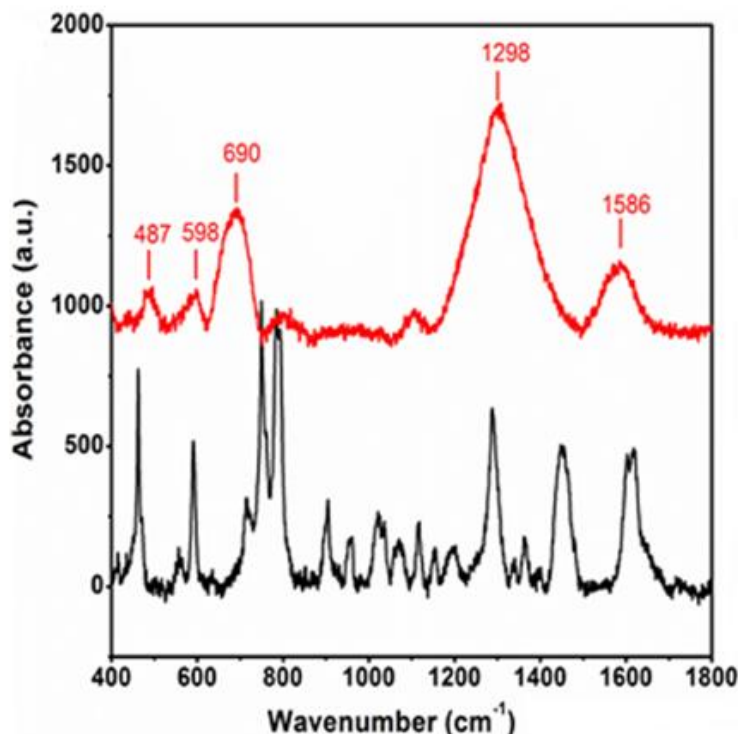
Figure 5.9. *Raman spectra of pure DOPA-polymer (black) and the multilayer hybrid films (red) of polymer/Fe$_3$O$_4$. The most prominent bands at 470-700 cm^{-1} and 1298 cm^{-1} are assigned to DOPA-iron coordination and the vibrations of the carbon atoms of the catechol ring, respectively.*

The Raman spectrum of the as-prepared polymer displays a strong band at 1629 cm^{-1} due to OH deformation modes of the hydroxyl groups and weak bands at 1752 cm^{-1} and 1600 cm^{-1} due to C=O and N-H bending vibrations of the amide bond of the polymeric ligand. [42] Moreover, bands at 852 cm^{-1}, 814 cm^{-1}, 791 cm^{-1} are assigned to the C-O groups of 1,2,4 tri-substituted aromatic rings while the C=C ring stretch appears at 1503 cm^{-1}. The Fe$_3$O$_4$/polymer multilayered films show ν (O−H) stretching modes between 470-700 cm^{-1} for catechol-iron coordination. [31]

These most prominent bands are assigned to the interaction of the transition metal atoms with the phenolic oxygen atoms of the catechol. [43] The bands at 487, 598 cm^{-1} and 690 cm^{-1} are assigned specifically to bi-dentate chelation of the metal ion by the phenolic oxygen atoms of catechol. Moreover, a strong broad band centered at 1298 cm^{-1} confirms the catechol iron complexation further, depicting most of the vibrations of the aromatic ring.
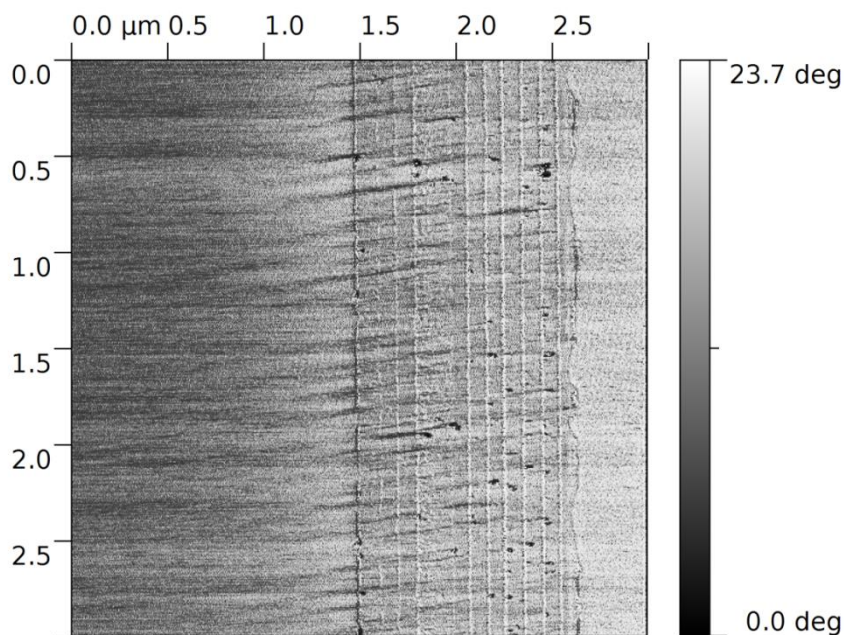
Figure 5.10. *AFM phase image of cross-section of the multilayered polymer/Fe$_3$O$_4$ films. The organic layers appear narrow as bright region bands with a thickness of ≈ 4 nm, while the inorganic layers appear as dark broader regions with a thickness of ≈ 35 nm. All films are coated on silicon substrates.*

Atomic Force Microscopy (*AFM*) images of the multilayered polymer/Fe$_3$O$_4$ films are shown in Figure 5.10; all images are taken on silicon wafers. The AFM image shows the presence of uniform periodic layers of the organic (light) and inorganic layers (dark). The thickness of the polymer layer is ~ 4 nm while the iron oxide layers are ~35 nm in thickness. The cross-linked composite films show high uniformity and strength as indicated by the nanoindentation results.

5.2.2.1. Nanoindentation on Hybrid Films

Many biological materials show a high degree of toughness, damage tolerance and increased hardness owing to their structural hierarchy and constituent materials. [2, 44] Most of these materials are hybrids involving weak constituents that combine in an organized way to produce a tough structure, the unusual hardness exhibited by nacre being a case in point. [3] Coordination based crosslinking in some biological materials is an important factor contributing towards the increased hardness. This is evidently the case in marine mussel cuticles that are rich in DOPA and inorganic metal ions, where a high degree of cross-linking due to stable iron-catechol complexes is responsible for increased hardness. The absence of mineralization in cuticles means that the complexation between the Fe^{3+} ions and catechol groups of DOPA is responsible for the crosslinking that leads to extra hardness, as proved by earlier studies. [30] Keeping this factor in mind, the multilayers of DOPA-polymer/Fe_3O_4 prepared by spin coating are characterized with a view to manipulate the mechanical properties of these hybrids.

The Young's modulus (E) and hardness (H) of the multilayers of DOPA-polymer/Fe_3O_4 nanoparticles are measured by nanoindentation. The method involves applying a load to the indenter which is in contact with the sample. The depth of indentation is measured as the load is applied and the area of contact (A) is calculated. The details of the method can be found in Section 8.4 of the Appendix.

Each series of indentations is carried out on a grid of 2x6 indents on a 90x90 μm^2 area at three different positions on the sample. This means that a total of 36 indents per series were carried out on the multilayers. The Young's moduli and hardness are calculated by fitting the indentation curves according to the Oliver-Pharr method [45] using the analysis software of the nanoindenter. The Young's modulus is obtained as the *elastic* response of the sample upon unloading, i.e., from the slope of the onset of the unloading curve. The hardness of the material is obtained as the ratio of maximum applied load (P_{max}) divided by the indenter contact area at that load and is indicative of the *resistance* of the material against plastic deformation.

The catechol-polymer/Fe_3O_4 multilayer films show extraordinary mechanical strength with a Young's modulus of $E = 17 \pm 3$ GPa and a hardness of $H = 1.3 \pm 0.4$ GPa. Compared to earlier works on bio-inspired hard materials, [11, 46] the modulus shown by these hybrid films is high.

The force-indentation curves of the multilayered films are shown in Figure 5.11. The substrate effect is observed for maximum applied loads higher than 100 μN (represented by black data points). To eliminate any contribution from the underlying substrate, only maximum applied forces under 100 μN are considered (represented by red and blue data points).
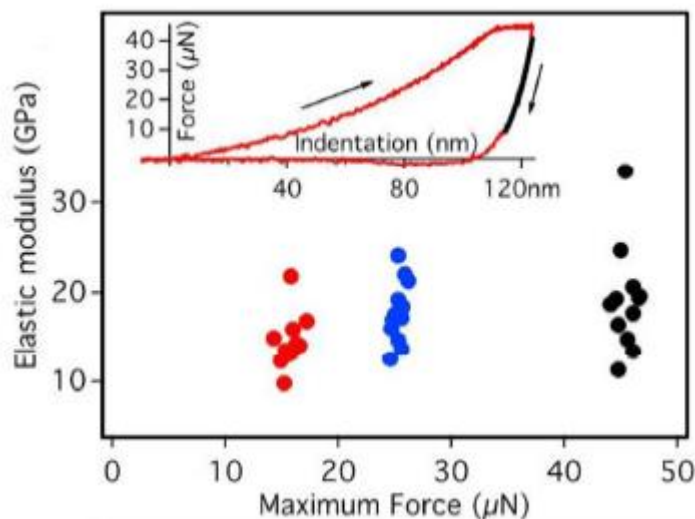
Figure 5.11. Young's modulus for nanocomposites from multilayered dopamine modified polymer/metal oxide (Fe$_3$O$_4$)nanoparticles as obtained by nanoindentation at different maximum forces. The red, blue and black data points indicate nominal forces of 15, 25 and 45 μN respectively. No measurable effect of the underlying silicon is observed in this force range. The inset on the upper left shows a typical force versus indentation curve with a maximum load of 40 μN. The red line is the measured force curve while the black line is the fit to the data. The arrows mark the indentation and retraction part of the curves.

It should be mentioned that the estimation of *E* required the knowledge of the Poisson ratio (υ), the value of which is assumed to be ~0.3. However, a variation of υ in the range of 0.2 to 0.4 had only a negligible effect (about 5%) of the absolute value) on the elastic modulus and hardness.

Dip-Coated Multilayers:

The multilayers of catechol polymer/ Fe$_3$O$_4$ nanoparticles prepared by dip-coating are measured by nanoindentation. Pre-cleaned silicon wafers are used for dip-coating of multilayers made of catechol-polymer and iron oxide nanoparticles. The wafer is dipped vertically in 2% polymer

dispersion in DMA for an (optimized) time and dried in a stream of nitrogen before annealing at 120 °C for 20 min. The process is repeated for coating the nanoparticle layer by dip-coating the wafer in Fe_3O_4 dispersion in hexane (1200 mg in 16mL) for a selected time duration followed by heat treatment. The process is repeated to obtain 12 bilayers of catechol-polymer and iron oxide nanoparticles. The final multilayered structure is characterized by nanoindentation (Figure 5.12) to compare its mechanical properties to those of the spin-coated multilayers.
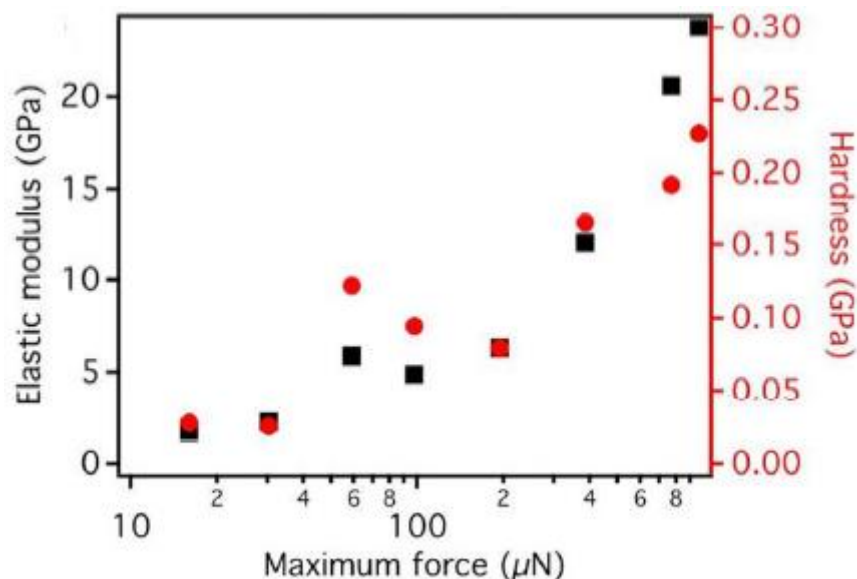
Figure 5.12. *Young's modulus (black squares) and hardness (red circles) for thin films prepared by dip-coating of a premixed nanoparticle/dopamine modified polymer dispersion are shown.*

The dip-coated multilayers show a much lower elastic modulus of E ~ 2 GPa compared to the spin-coated multilayers due to unavoidable defects introduced during fabrication. This concept is discussed in detail later in this chapter.

Role of Dopamine-modified Polymer in Polymer-Particle Interactions:

In order to clarify the role of the dopamine-modified polymer in the polymer-particle interactions, a series of control experiments are conducted with a composite film containing a polymer with a similar structure but without dopamine groups to compare the mechanical properties. To this end,

analogous samples are prepared using only iron oxide (Fe_3O_4) nanoparticles and iron oxide (Fe_3O_4) nanoparticles witm PMMA (a polymer without any reactive sites) to see the effect of catechol binding. After drying the sample, the PMMA is in a glassy state. A series of indentation experiments are performed on this PMMA/Fe_3O_4 nanoparticle sample, varying the load systematically (from ~10N to 80 N) and time scale of indentation (from 0.1 s to 10 s). Upon indentation, the PMMA based sample show a strong creeping behavior irrespective of the indenter shape (cube corner or Berkovich). This implies that even the smallest loads possible are beyond the yield stress of the PMMA-based sample. In the resulting force curves, no hint for the onset of the creeping behavior is found i.e. the onset of creeping vanished in the noise of the instrument.

The Secret of Strength:

A model depicting nano-indentation of the multilayered polymer/Fe_3O_4 hybrid films is shown in Figure 5.13. The strong crosslinking between the Fe_3O_4 nanoparticles and the multi-dentate polymer ligand helps the matrix to resist deformation and make the composites harder and stronger.
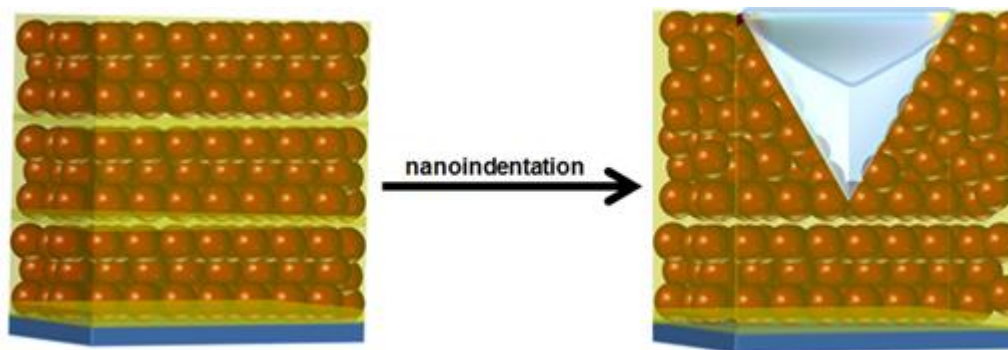
Figure 5.13. *Nano-indentation of a multilayer Fe_3O_4/DOPA polymer composite is shown. This model illustrates the cohesive role of the DOPA polymer in the multilayers.*

Several factors may explain the high mechanical strength of the catechol-polymer/ Fe_3O_4 composites. The high values of modulus could be a direct result of the strong covalent interactions between catechol groups of the DOPA polymer and iron oxide nanoparticles. It is a well-established fact that the catechol groups in the catechol-polymer form stable complexes with iron in natural environment, with the degree of crosslinking varying with the catechol and Fe^{3+} content

and pH. [47, 48] Oxidation of catechol groups of DOPA at alkaline pH leads to crosslinking between neighboring polymer chains [39] because catechols are oxidized to quinones at temperatures > 90 °C, which then undergo a Michael-type addition with adjacent catechol groups. At ambient temperature, catechols do not exhibit strong chemical reactivity. Crosslinking between DOPA and metal ions greatly contributes to the strength of the hybrid. [25] It is worth mentioning that the multidentate nature of the polymeric ligand, intermolecular interactions like π-π, and H-bonding of the same polymer cementing different nanoparticle surfaces play a major role for enhanced mechanical properties of the stacks. The possible intermolecular interactions of the polymeric ligand upon heating are also indicated by measuring the solubility of the polymeric ligand annealed under a similar set of conditions. The polymer is insoluble in DMA even after long time ultrasonication and heating, as shown in Figure 5.14.
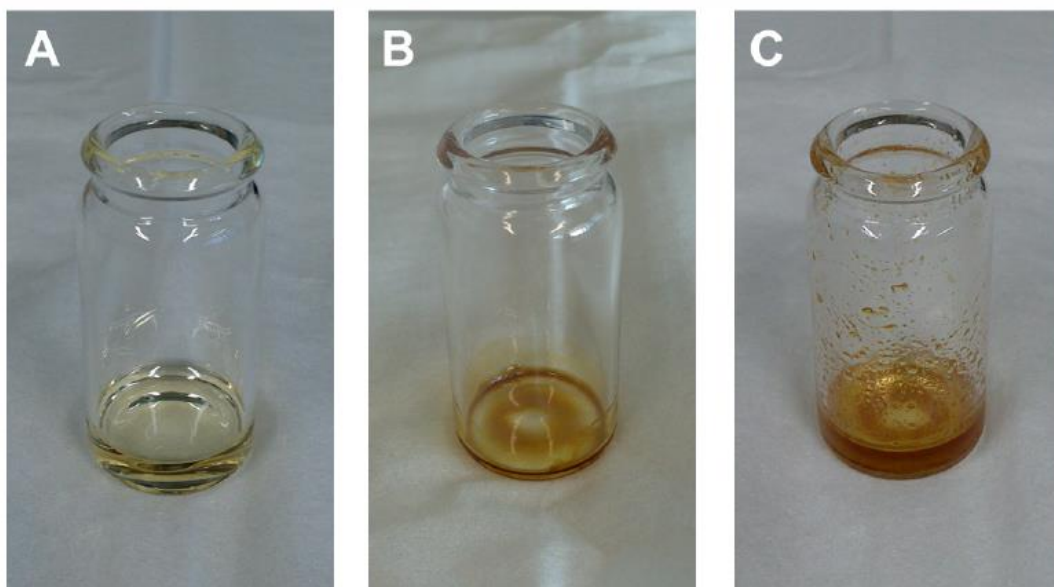
Figure 5.14. Digital photographs (A) As prepared dopamine-modified polymer solution in DMA (B) After heating the solution at 120C for 20 min (C) Dissolution in DMA using ultrasonication for several hours.

A scheme illustrating the possible role of the polymeric ligand and surface of nanoparticles in enhanced mechanical properties is shown in Figure 5.15. Hydrogen binding is assumed to play a minor role because all samples are prepared under non-aqueous conditions.
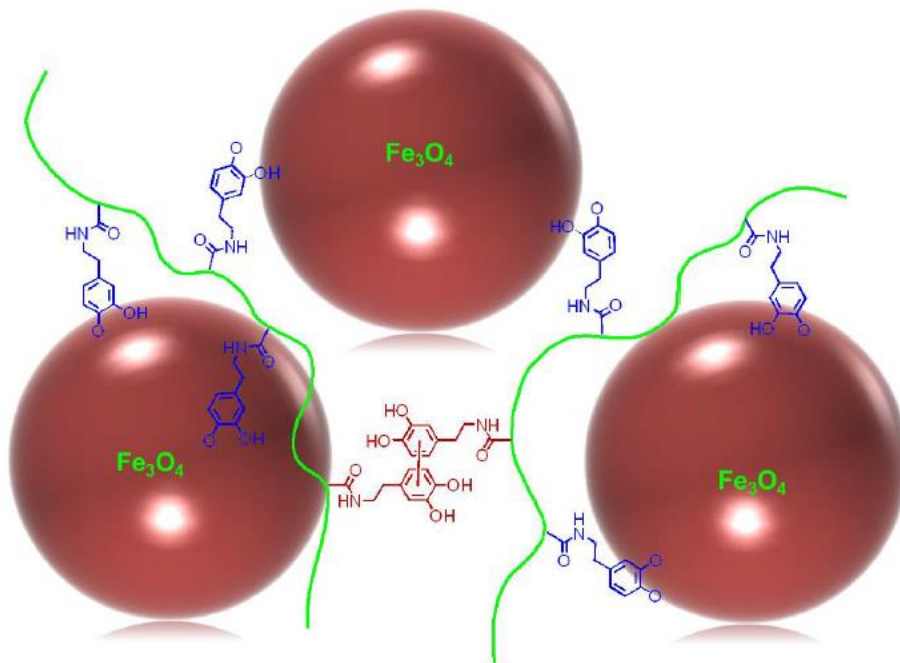
Figure 5.15. *Sketch of the connectivity of Fe₃O₄ nanoparticles through the dopamine modified polymer.*

The high stability constant of the iron-catecholato complex appears to be an important factor in describing the mechanical behavior of these composites. It has been reported that the tris and bis catechalato complexes with iron ions in marine mussels above pH 7.5 are extremely stable. [49] The binding constant of the catechol-Fe^{3+} complexes have been reported to be as high as ~ 10^{49} [50] and the high value indicates the stability of the iron-catechalato complexes, further explaining the strong mechanical behavior of mussel cuticles rich in the catechol-containing amino acid, catechol and Fe^{3+} ions. [51, 52] The iron oxide nanoparticles have a particle diameter of 4 nm (Figure 5.3), so each Fe_3O_4 particle has a surface area of 5000 $Å^2$. If a surface segment of 25 $Å^2$ per catechol anchor group, a 100% side group substitution of the polymer and full surface coverage is assumed, each particle will be bound to ~ 200 catechol groups of different polymer chains. The bonding at the interface and subsequent infiltration of the polymer into the nanoparticle layers leads to the formation of a tough Fe_3O_4/dopamine modified polymer composite with the polymer acting as "glue".

The dense and well-ordered packing of the nanoparticles in the nanocomposites (as confirmed by TEM image) is another important structural parameter that affects their mechanical properties, similar as described for nacre. [13] In the nanocomposite, the iron oxide nanoparticles are close packed (Figure 5.6) and the individual polymer chains can directly cross-link neighboring particles, thereby directly boosting the strength of the nanocomposite. Since it has already been established that the absence of Fe^{3+} ions greatly reduces the hardness of mussel cuticles, [30] it may be pointed here that the high value of modulus observed in the multilayered polymer/Fe_3O_4 hybrids is due to the strong crosslinking. The hardness i.e. the resistance of a material against plastic deformation, is strongly enhanced if there is direct bridging between individual nanoparticles by the polymer. Such a configuration imposes the necessity to break many of the strong iron-catechol bonds (or the backbone of the polymer chain itself) to allow for plastic deformation as the indenter penetrates into the surface of the hybrid Bragg stacks (Figure 5.13).

In an earlier report, Mammeri et al., [53] have underlined the important factors determining the mechanical properties of inorganic-organic hybrids as (i) the choice of solvent, (ii) the number of anchor groups and (iii) the nature of the interaction between the inorganic and organic components. The same factors account for the increased hardness and Young's modulus of the polymer/Fe_3O_4 composite films. Additionally, the high packing density of the particular nanostructure, (Figure 5.6) which can be assumed as close packed, makes an important contribution to the mechanical properties of the hybrid films.

Role of Structure, Defects and Morphology:

To examine whether the strong interfacial bonding of the infiltrated close packed Fe_3O_4 nanoparticle layers is sufficient to account for the extraordinary strength of the 6BL nanocomposite, the role of defects and morphology is addressed in this section. The number of layers is increased and hence the defect probability, while for the exemplification of the latter a dopamine modified polymer/ Fe_3O_4 blend of similar composition is considered.

For a thicker nanocomposite of 16 BL, nanoindentation yields a much lower E = 11 ± 5 GPa using υ in the range of 0.2-0.3. For this thicker stack, Brillouin light scattering (BLS) is employed to directly obtain the longitudinal modulus (*M*), which is related to E via the Poisson ratio. [54] BLS,

A non-destructive and non-contact optical technique, directly measures the frequency (*f*) of the thermally activated acoustic phonons due to inelastic scattering of photons. From the BLS spectra (inset to Figure 5.16), recorded at different phonon wave vectors (*q*), the dispersion *f(q)* for homogenous samples is linear and leads to the phase sound velocity, *c = 2πf/q*. [55] Since the refractive index enters in the calculation of q_{perp} only, the linear dispersion applies with n_{eff} = 1.92 for the 16 BL stack. Due to the inevitable infiltration of dopamine modified polymer in the much thicker Fe_3O_4 layers, the volume fraction of Fe_3O_4 is estimated from a linear composition dependence of n_{eff} to be φ ~ 0.43 (*n $_{Fe3O4}$ = 2.42, $n_{dopamine}$ = 1.55*).
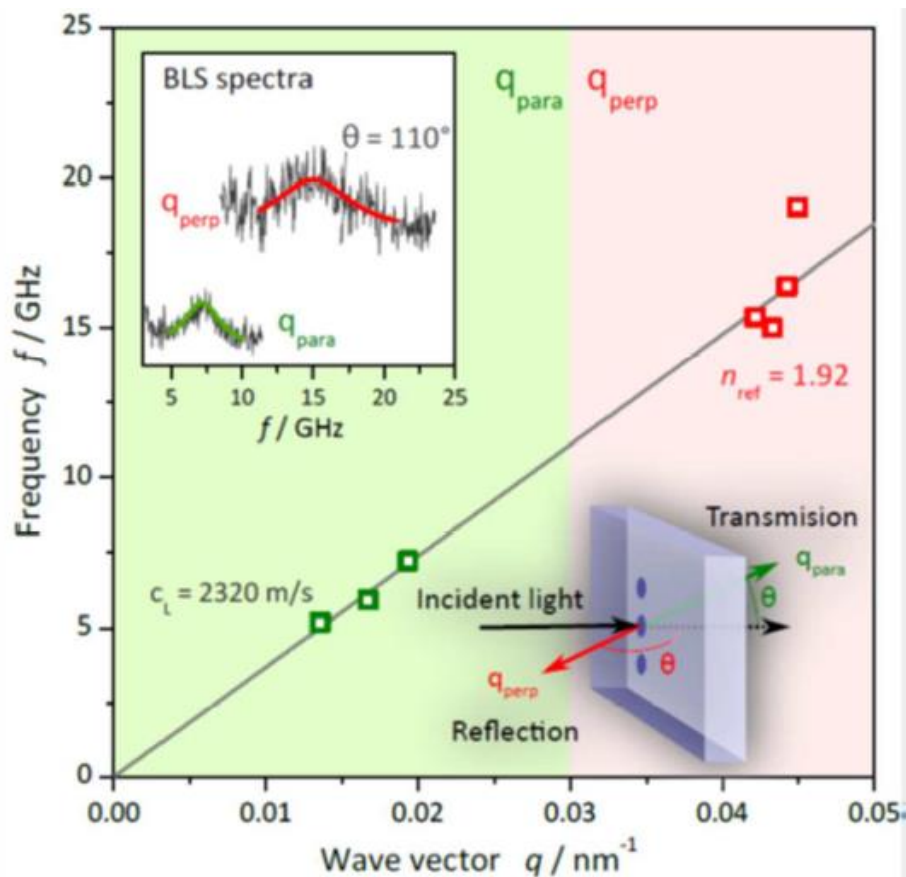
Figure 5.16. *Brillouin spectroscopy of the multilayer nanocomposite. Frequency of the longitudinal acoustic phonon as a function of its wave vector in – (q_{para}) and out-of- (q_{perp}) of the film (lower inset) obtained from Brillouin light spectra (upper inset) recorded in transmission (q_{para}) and reflection (q_{perp} out of plane of the film) as shown schematically in the lower inset. The displayed spectra was recorded for the same scattering angle (Θ = 110°) but correspond to two different q values (q_{para}, q_{perp}).*

For longitudinal polarization, the corresponding modulus is given by

$$M = \rho \, c_L{}^2 \tag{5.1}$$

which comes out as **M = 15 ± 2 GPa** for a density, ρ = 2.8 g/cm3 (ρ_{Fe3O4} = 5.1 g/cm^3 and $\rho_{dopamine}$ = 1 g/cm^3). The two moduli, *M* and *E* from two different techniques are consistent for a Poisson's ratio $\upsilon \sim 0.3$. Using the latter value, the computed longitudinal modulus for the 6 BL film (E = 24 GPa) corresponds to M = 32 GPa.

The 16 BL sample shows the presence of large defects as the number of bilayers increase, as can be seen from the TEM images shown in Figure 5.17 (A). This is an expected phenomenon cooroborated by the lower value of moduli (E = 11 ± 5 GPa) obtained from nanoindentation and M = 15 ± 2 GPa as obtained from Brillouin Light Scattering.
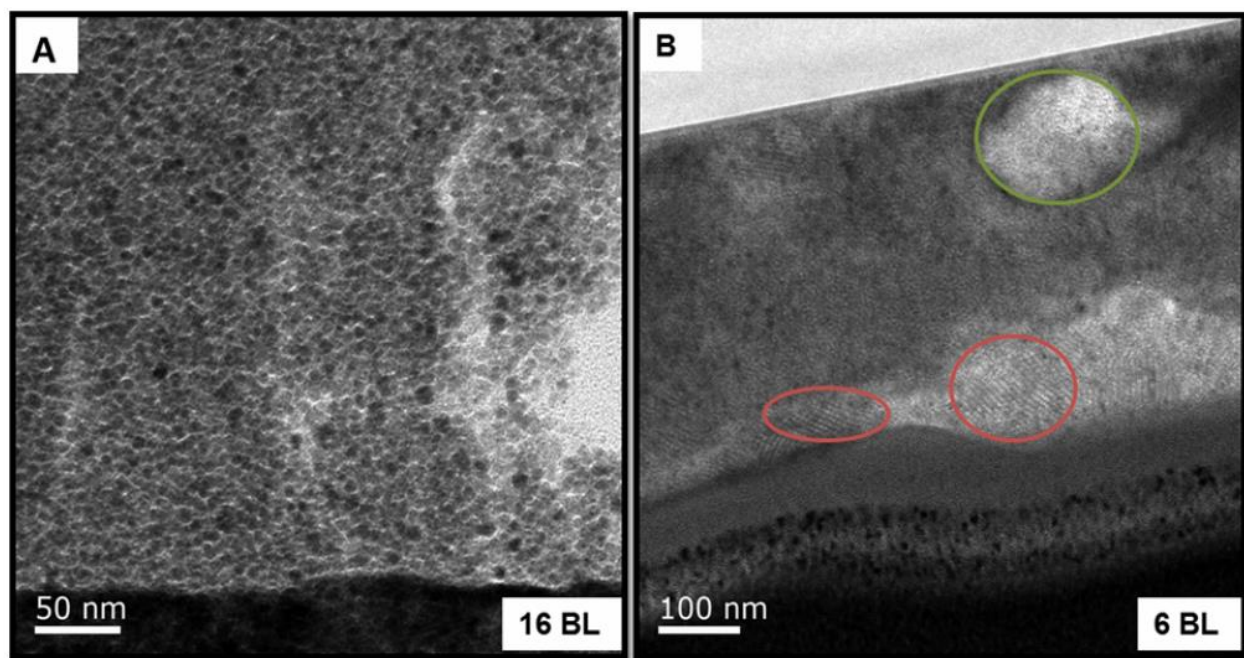
Figure 5.17. TEM images of different samples of dopamine modified polymer/ Fe₃O₄ nanoparticles consisting of a varying number of multilayers (A) A sample prepared by 32 spin-coating cycles shows the existence of large defected regions as the number of multilayers increase. (B) On the other hand, a sample prepared by 12 dip-coating cycles reveal the existence of ordered (red circles) and defected (green circle) regions in addition to a regular cross-linked network.

As seen from Figure 5.17 (B), the 6 BL sample prepared from dip-coating shows the existence of ordered (red circles) and defected (green circle) while the rest of the sample shows a cross-linked network. This result highlights the superior nature of spin-coating compared to the dip-coating procedure, as also reflected in the lower value of modulus (E ~ 2GPa) for the dip-coated multilayers.

To address the role of structure, the elastic E and M in a dopamine modified polymer/ Fe_3O_4 mixture with a deliberately high particle filling ratio (0.6) is prepared by drop-casting. For this dispersion, E = 12 ± 3 GPa assumes clearly a much lower value than in the 6BL periodic structure (E = 17 ± 3 GPa). A BLS experiment on the same homogenous dispersion leads to a single c_L = 2210 m/s and M = 18 ± 1 GPa being consistent with the E modulus using υ ~ 0.3. Apparently, strong binding is necessary but not sufficient to boost the mechanical properties of polymer nanocomposites, and a defect-free structure should be present as well.

In dispersion strengthened composites, the matrix is the major load-bearing component and therefore carries most of the load while deformation occurs by slip and dislocation movement. The added particles strengthen the material by impeding slip and dislocation while remaining unreactive to the matrix material. On the other hand in particle reinforced composites, the particle size is of the order of a few microns and the particles support a major portion of the load. The particles are used to increase the modulus and decrease the ductility of the matrix, but in general particle-matrix interactions are of minor importance. [56] However, our approach to infiltrate a meso-crystal of hard metal oxide nanoparticles with "sticky" polymers results in cementing of the nanoparticles via the organic biopolymer. Many metal-catechol bonds have to be broken prior to mechanical failure and the individual nanoparticles are too small and strong to break. In essence, the specific crosslinking between the nanoparticles and the multi-dentate polymer ligand helps the matrix resist deformation and makes the composite harder and stronger.

5.3. Conclusions

In summary, by utilizing the strong surface complexation of Fe_3O_4 nanoparticles by a catechol-polymer, hard multi-layered coatings with excellent mechanical properties have been fabricated with greatly enhanced and unprecedented mechanical properties. To date and to the best of our

knowledge, Young's modulus of 17 ± 3 GPa and a hardness of 1.3 ± 0.4 GPa measured for catechol polymer/Fe_3O_4 nanocomposites are among the highest values reported so far for inorganic nanoparticle/polymer composites. [11, 12, 16, 20] The multi-lamellar films may be used as robust, hard coatings with a high degree of flexibility depending on the polymeric template. This approach is widely applicable for different types of polymers and a large variety of inorganic building blocks and paves the way to a new family of bio-inspired materials. Besides making another step towards ex-vivo replication of the biological tissues, the multilayers can be used as a convenient model to understand fundamental molecular processes responsible for mechanical properties of composites predicted theoretically. This may allow the rational design of new smart materials equally desirable for diverse industries from aviation to medicine.

5.4. Instrumentation

The DOPA polymer/Fe_3O_4 hybrid multilayers are spin-coated using a Laurell WS-400-6NPP-LITE spin-coater. The size of the metal oxide nanoparticles is determined by Transmission Electron Microscopy (TEM) on a Phillips EM-420 equipped with a slow scan CCD detector ($1k \times 1k$) and a LaB6 electron gun operated with an acceleration voltage of 120 kV. The TEM images are processed with the Gnu Image Manipulation Program GIMP Version 2.6.8 or with Image J Version 1.43u. The TEM imaging of the hybrid multilayers of DOPA polymer/Fe_3O_4 is performed by preparing a lamella using Focused Ion Beam (FIB) instrument (FEI Nova 600 Nanolab FIB instrument). The lamella is fixed on TEM grid and eventually analyzed by electron energy-dispersive X-ray analysis (EDX) using Transmission Electron Microscope (Technai G2 F20; FEI/Philips) equipped with an EDX detector. A Horiba Jobin Y LabRAM HR Spectrometer with a frequency doubled Nd:YAG-laser is used for performing Raman spectroscopy. The sample is prepared by cutting a small portion (1 cm x 1 cm) of the multilayers prepared on glass slide.

The AFM images are captured using a commercial AFM instrument (Multimode,Nanoscope IIIa controller, Veeco, California, USA) in tapping mode. A piezoelectric scanner allows a maximum x, y-scan size of 17 μm and a maximum z-extension of 3.9 μm. All topography and phase contrast images were taken at room temperature under ambient conditions. The Young's modulus and hardness of the multilayer films is determined by nanoindentation using a MFP Nanoindenter (Asylum Research, Santa Barbara, CA) equipped with a diamond Berkovich indenter.

The 16 BL of catechol polymer/ Fe_3O_4 coated on glass substrate are analyzed by Brillouin Light Scattering (BLS). The details of the technique have been described earlier in this dissertation (Section 2.5).

Bibliography

1. R. Lakes, *Nature.* **1993**, 361, 511.

2. M. A. Meyers, J. McKittrick and P. -Y. Chen, *Science*. **2013**, 339, 773.

3. G. Mayer, *Science.* **2005**, 310, 1144.

4. P. Fratzl and R. Weinkamer, *Prog. Mat. Sci*. **2007**, 52, 1263.

5. P.-Y. Chen, J. McKittrick and M. A. Meyers, *Prog. Mat. Sci*. **2012**, 57, 1492.

6. F. Barthelat, *Bioinsp. Biomim*. **2010**, 5, 035001.

7. H. D. Espinosa, J. E. Rim, F. Barthelat and M. J. Buehler. *Prog. Mat. Sci.* 2009, **54,** 1059.

8. M. J. Buehler and S. Keten, *Rev. Mod. Phys*. **2010**, 82, 1459.

9. M. A. Meyers, P.-Y. Chen, A. Y. Lin and Y. Seki, *Prog. Mater. Sci*. **2008**, 53, 1.

10. J. Aizenberg, J. C. Weaver, M. S. Thanawala, V. C. Sundar, D. E. Morse and P. Fratzl, *Science*. **2005**, 309, 275.

11. Z. Tang, N. A. Kotov, S. Maganov and B. Ozturk, *Nat. Mater*. **2003**, 2, 413.

12. A. Walther, I. Bjurhager, J.-M. Malho, J. Ruokalainen and L. Berglund, *Angew. Chem. Int. Ed.* **2010**, 49, 6448.

13. A. Finnemore, P. Cunha, T. Shean, S. Vignolini, S. Guldin, M. Oyen and U. Steiner, *Nature Commun*. **2012**, 3, 1.

14. S.-M. Lee, E. Pippel, U. Gösele, C. Dresbach, Y. Qin, C. Vinod Chandran, T. Bräuniger, G. Hause and M. Knez, *Science*. **2009**, 324, 488.

15. Z. Burghard, L. Zini, V. Srot, P. Bellina, P. A. van Aken and J. Bill, *Nano Lett*. **2009**, 9, 4103.

16. S. Deville, E. Saiz, R. K. Nalla and A. P. Tomsia, *Science*. **2006**, 311, 515.

17. E. Munch, M. E. Launey, D. H. Alsem, E. Saiz, A. P. Tomsia and R. O. Ritchie, *Science*. **2008**, 322, 1516.

18. T. Lin, W. Huang, I. Jun and P. Jiang. *Bioinspired Assembly of Inorganic Nanoplatelets for Reinforced Polymer Nanocomposites: Advances in Biomimetics*, M. Cavrak (ed.), ISBN: 978-953-307-191-6, **2011**.

19. T. Lin, W. Huang, I. Jun and P. Jiang, *Chem. Mater*. **2009**, 21, 2039.

20. A. Sellinger, P. M. Weiss, A. Nguyen, Y. F. Lu, R. A. Assink, W. L. Gong and J. Brinker, *Nature*. **1998**, 394, 256.

21. L. J. Bonderer, A. R. Studart and L. J. Gaukler, *Science*. **2008**, 319, 1069.

22. P. Podsiadlo, S. Paterne, J.-M. Rouillard, Z. Zhang, J. Lee, J.-W. Lee, E. Gulari and N. A. Kotov, *Langmuir*. **2005**, 21, 11915.

23. F. Natalio, T. Coralles, M. Panthöfer, I. Lieberwirth, D. Schollmeyer, W.E.G. Müller, M. Kappl, H.-J. Butt and W. Tremel, *Science*. **2013**, 339, 1298.

24. R. H. Holm, P. Kennepohl and E. I. Solomon, *Chem. Rev*. **1996**, 96, 2239.

25. P. Podsiadlo, Z. Lin, D. Paterson, P. B. Messersmith and N. A. Kotov, *Adv. Mater*. **2007**, 19, 949.

26. B. P. Lee, P. B. Messersmith, J. N. Israelachvili and J. H. Waite, *Annu. Rev. Mater. Res*. **2011**, 41, 99.

27. H. Lee, S. M. Dellatore, W. M. Miller and P. B. Messersmith, *Science.* **2007**, 318, 426.

28. A. Rai and C. C. Perry, *J. Mater. Chem*. **2012**, 22, 4790.

29. E. Karabulut, T. Pettersson, M. Ankerfors and L. Wagberg, *ACS Nano*. **2012**, 6, 4731.

30. M. J. Harrington, A. Masic, N. Holten-Andersen, J. H. Waite and P. Fratzl, *Science.* **2010**, 328, 216.

31. D. S. Hwang, H. Zeng, A. Masic, M. J. Harrington, J. N. Israelachvili and J. H. Waite, *J. Biol. Chem*. **2010**, 285, 25850.

32. S. Sun and H. Zeng, *J. Am. Chem. Soc*. **2002**, 124, 8204.

33. M. N. Tahir, M. Eberhardt, P. Theato, S. Faiß, A. Janshoff, T. Gorelik, U. Kolb and W. Tremel, *Angew. Chem. Int. Ed*. **2006**, 45, 908.

34. M. Eberhardt, R. Mruk, R. Zentel and P. Theato, *Eur. Polym. J*. **2005**, 41, 1569.

35. J. Wang, M. N. Tahir, M. Kappl, W. Tremel, N. Metz, M. Barz, P. Theato and H. J. Butt, *Adv. Mater*. **2008**, 20, 3872.

36. H. G. Silverman and F. F. Roberto, *Mar. Biotechnol*. **2007**, 9, 661.

37. M. I. Shukoor, F. Natoli, N. Glube, M. N. Tahir, H. A. Therese, V. Ksenofontov, N. Metz, P. Theato, P. Langguth, J.-P. Boissel, H.-C. Schröder, W. E. G. Müller and W. Tremel, *Angew. Chem. Int. Ed*. **2008**, 47, 4748.

38. C. G. Pierpont and C. W. Lange, *Prog. Inorg. Chem*. **1994**, 41, 381.

39. H. Lee, N. F. Scherer and P. B. Messersmith, *Proc. Natl. Acad. Sci*. **2006**, 103, 12999.

40. M. J. Sever, J. T. Weisser, J. Monahan, S. Srinivasana and J. J. Wilker, *Angew. Chem. Int. Ed*. **2004**, 43, 448.

41. M. J. Sever and J. J. Wilker, *Dalton. Trans*. **2006**, 813.

42. A. A. Ooka and R. L. Garell, *Biopolymers*. **2000**, 57, 92.

43. N. –H. Anderson et al., *Proc. Natl. Acad. Sci*. **2011**,108, 2651.

44. J. C. Weaver, G. W. Milliron, A. Miserez, K. –E. Lutterodt, S. Herrera, I. Gallana, W. J. Mershon, B. Swanson, P. Zavattieri, E. DiMasi and D. Kisailus, *Science*. **2012**, 336, 1275.

45. W. C. Oliver and G. M. Pharr, *J. Mater. Res*. **1992**, 7, 1564.

46. A. Walther, I. Bjurhager, J.-M. Malho, J. Ruokalainen and L. Berglund, *Angew. Chem. Int. Ed*. **2010**, 49, 6448.

47. D. G. Barrett, D. E. Fullenkamp, L. He, N.-H. Andersen, K. Y. C. Lee and P. B. Messersmith, *Adv. Funct. Mater*. **2013**, 23, 1111.

48. S. W. Taylor, D. B. Chase, M. H. Emptage, M. J. Nelson and J. H. Waite, *Inorg. Chem*. **1996**, 35, 7572.

49. H. Zeng, D. S. Hwang, J. N. Israelachvili and J. H. Waite. *Proc. Natl. Acad. Sci*. **2010**, 107, 12850.

50. L. D. Loomis, K. N. Raymond, *Inorg. Chem*. **1991**, 30, 906.

51. N.-H. Andersen, T. E. Mates, M. S. Toprak, G. D. Stucky, F. W. Zok and J. H. Waite, *Langmuir*, **2009**, 25, 3323.

52. M. J. Sever and J. J. Wilker, *Dalton. Trans*. **2006**, 813.

53. F. Mammeri, E. L. Bourhis, L. Rozes and C. Sanchez, *J. Mater. Chem*. **2005**, 15, 3787.

54. T. Still, M. Oudich, G. K. Auerhammer, D. Vlassopoulos, B. Djafari-Rouhani, G. Fytas and P. Sheng, *Phys. Rev*. **2013**, B88, 094102.

55. K. L. Kearns, T. Still, G. Fytas and M.D. Ediger, *Adv. Mater*. **2010**, 22, 39.

56. N. Chawla and Y.-L. Shen, *Adv. Engg. Mat*. **2001**, 3, 357.

6

Structural Ordering in Magnetic Hybrid Multilayers

Faroha Liaqat, Sergi Shylin, Muhammad Nawaz Tahir, Vadim Ksenofontov and Wolfgang Tremel,

"Collective Behavior in Assemblies of Iron Oxide Nanoparticles Imbedded in a Sticky Polymer Matrix Observed by Mössbauer Spectroscopy"

In progress
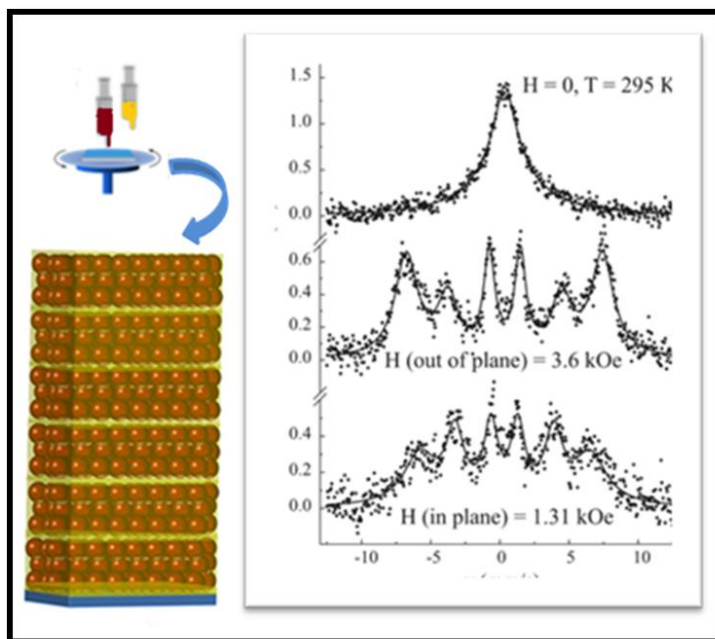
6.1. Introduction

Various techniques have been employed to study anisotropy stemming from aligned magnetic domains in thin films. Anisotropy can arise from either aggregation of particles or crystallites, their shapes or aligned crystalline defects. [1] In particular, multilayers have shown remarkable anisotropic properties along with other interesting phenomenon as found by magnetic studies. It has been shown that the magnetic properties depend on the materials constituting the multilayers, the fabrication procedure and the orientation of the film and the substrate. [2] Studies of magnetic properties in composites of nanoparticles of iron oxide and polymers have also been receiving attention from researchers. [3, 4] The nanocomposites may contain encapsulated iron oxide nanoparticles in a polymer matrix or in some instances, in an inorganic oxide matrix such as silica. [5] Such methods enable an extensive utilization of the unique magnetic properties of the magnetic nanoparticles while limiting particle growth at the same time.

Mössbauer spectroscopy is an excellent tool to study iron containing hybrids. It makes use of the Mössbauer effect (first observed in 1957) which is based on the observation that nuclei in solid materials can absorb and emit γ-rays without recoil. Valuable information on the electronic and magnetic properties of iron species in hybrid structures can be obtained from Mössbauer measurements. The method probes small energy changes in the nucleus of an atom with reference to its environment and is a useful technique that gives an insight into the interactions of the different nuclei present, the valence states and information about the surrounding environment. Additionally, a magnetically split Mössbauer spectrum is an indication of magnetic ordering within the material under consideration. [6]

The study of iron oxide nanoparticles interconnected by a polymer or embedded in a polymer or inorganic matrix becomes greatly simplified by using Mössbauer spectroscopy as a means of scientific investigation about the hybrids. The use of this technique has recently been boosted by the variant Conversion Electron Mössbauer Spectroscopy (*CEMS*) for studying surface/interface magnetism. Although there have been a number of Mössbauer studies on multilayers containing iron in combination with other metals, as well as composites containing iron oxides, [5, 6] research has mostly focused on conventional methods of preparation. [7-9] A number of factors come into play during the preparation of multilayer films and not all have been taken into account in previous studies. There is a small amount of literature available

on hybrid inorganic-organic multilayers, studied by Mössbauer spectroscopy and it served as a motivation for this work. The multilayers of DOPA containing polymer and iron oxide nanoparticles (*Fe₃O₄*) prepared by high speed spin coating (described earlier in Chapter 5 of this thesis) have been characterized by Mössbauer spectroscopy. This chapter attempts to analyze the results keeping in mind the structural ordering present within the multilayers. The motivation of this work lies in studying the magnetic interactions between iron oxide nanoparticles in an ordered hybrid nanostructure and to examine the influence of the polymer matrix on these interactions. This is an ongoing preliminary study and this chapter takes into account the initial results only. The optical transparency of the multilayered films of DOPA-polymer/Fe_3O_4 can be used in applications, such as opto-magnetic devices and recording media.

6.2. Results and Discussion

6.2.1 Fabrication

This section describes the preparation of hybrid multilayers consisting of a DOPA-rich polymer (*P*) and iron oxide (Fe_3O_4) nanoparticles (*NPs*). The details of the method have been described earlier in Section 5.2.1 of this thesis. The iron oxide nanoparticles are synthesized with some alterations to a method reported by Sun et al. [10] The magnetic nanoparticles thus produced have a size of 4 nm, as determined from TEM images and are monodisperse (Figure 6.1 (D)). The DOPA-polymer constituting the organic layers in the superlattice, is rich in catechol groups and prepared from free radical polymerization leading to a pre-polymer. The pre-polymer is rich in active ester groups, which are replaced by 3-hydroxytyramine anchor groups in a second step. [11-12] The synthesis has been described in detail in Section 5.2.1.

The multilayers are coated on a glass substrate or silicon wafer which has been pre-cleaned in acidic piranha solution of concentrated sulphuric acid (H_2SO_4) and hydrogen peroxide (H_2O_2) in a volume ratio of 2:1. The multilayers are assembled by consecutive spin coating of a 2% DOPA polymer solution in dimethylacetamide (DMA) and Fe_3O_4 NPs dispersion (600 mg) in hexane, starting from the DOPA-polymer layer due to its high affinity to the substrate and adhesive character.

Spin coating is performed at a speed of 5000 rpm with an acceleration of 5040 rpm/s for 10 s. Each layer is annealed at 120 ˚C for 15 min prior to the next coating. As the subsequent spin coating cycles are performed, the polymer seeps through the pores of the inorganic nanoparticles and forms a crosslinked hybrid (Figure 6.1 (F). Figure 6.1 shows the fabrication scheme. Superlattices consisting of 16 bilayers are considered for Mössbauer studies.
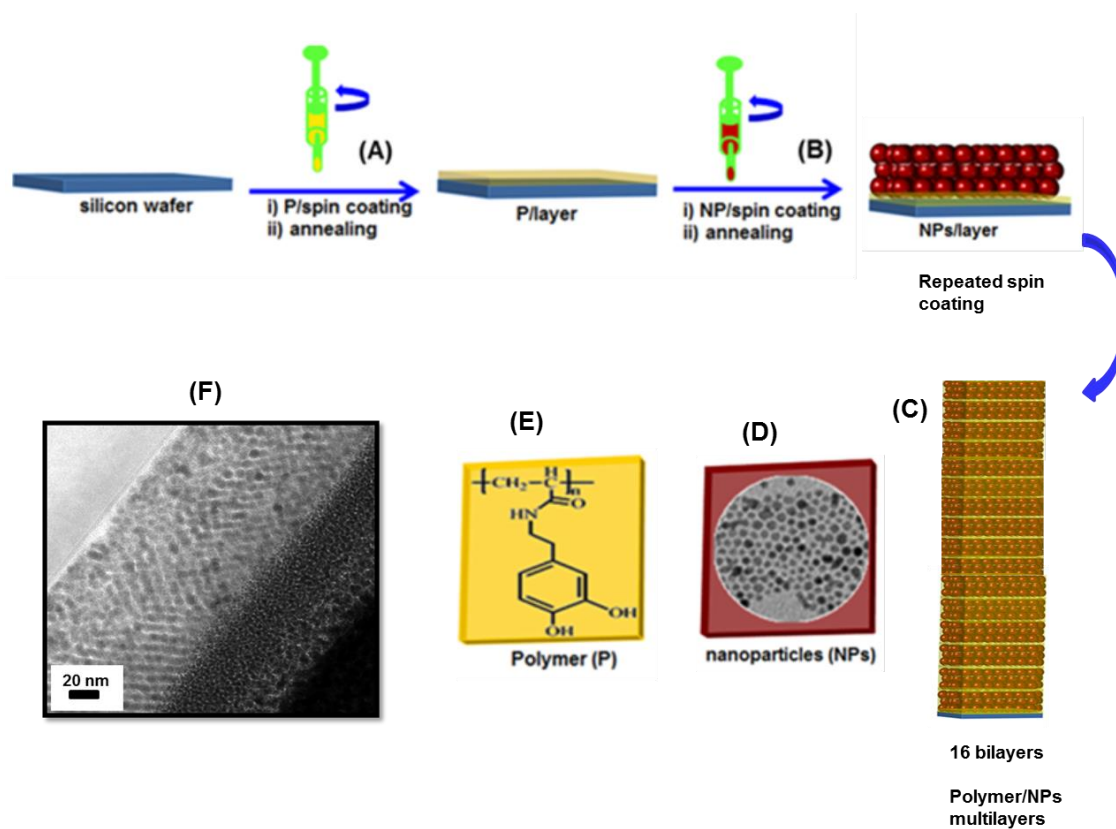
Figure 6.1. *Multilayers of DOPA-polymer (E) and the iron oxide nanoparticles (D) are assembled on a silicon wafer by consecutive spin-coating of dilute polymer solution and nanoparticle dispersion (A and B). Thirty two subsequent spin casting cycles of the polymer and the nanoparticles are performed to build up a 16 bilayers of polymer/nanoparticles (C). The TEM image of the DOPA polymer/Fe₃O₄ hybrid reveals a highly cross-linked network due to penetration of polymer inside the nanoparticle framework. The scale bar is 20 nm.*

6.2.2. Mössbauer Studies on Hybrid Multilayers

Mössbauer studies of the multilayers of DOPA polymer/Fe_3O_4 bilayers are carried out at room temperature. Bragg stacks consisting of 16 bilayers are considered for the measurements.
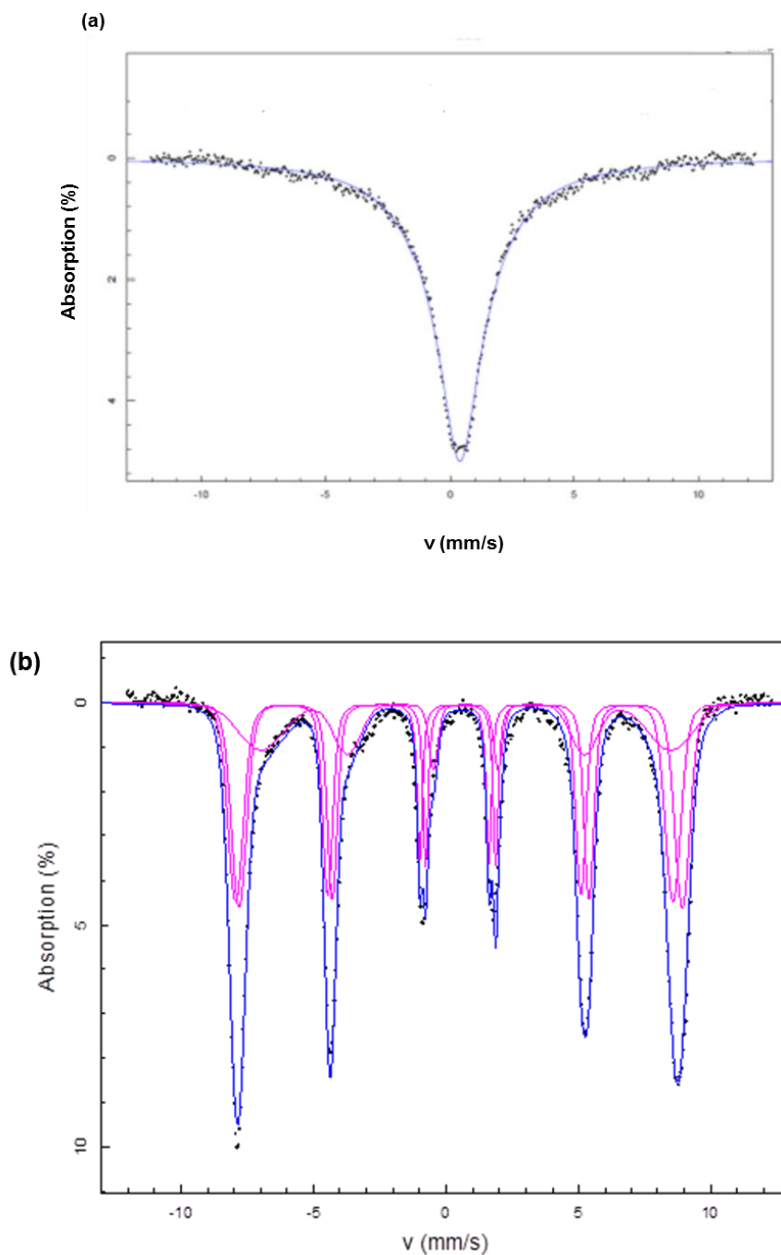
Figure 6.2. ^{57}*Fe Mössbauer spectra of iron oxide nanoparticles recorded at (a) 295 K (b) 5.9 K*

Figure 6.2 depicts the Mössbauer spectra of the precursor iron oxide nanoparticles. The measurements carried out without magnetic field demonstrate a superparamagnetic (dynamic) behavior, typical for nanoparticles with an average size of ~ 4-5 nm. The observed chemical shift, δ for the precursor iron oxide nanoparticles is 0.386 mm/s. Figure 6.2 (a) shows a typical spectrum of relaxation at room temperature and it is observed that relaxation can be achieved with magnetic field, H = 518 kOe, giving the fluctuation factor, f = 300 MHz). At low temperature (5.9 K), the iron oxide nanoparticles show a typical magnetic spectrum composed of sextets. A close inspection of the spectra in Figure 6.2 (b) indicates that the iron oxide nanoparticles are a mixture of magnetite (Fe_3O_4) and maghemite (Fe_2O_3). [13]

Maghemite is considered as an allotropic form of magnetite deficient in Fe (II) and is represented by Fe^{3+} $[Fe^{3+}_{5/3} \square_{1/3}]$ O_4 where $\square$ represents the vacancies. Magnetite, on the other hand, has both Fe^{2+} and Fe^{3+} distributed between octahedral and tetrahedral site and is commonly represented as Fe^{3+} $[Fe^{2+} Fe^{3+}]O_4$. The Mössbauer spectrum of magnetite at room temperature comprises of two superimposed patterns due to Fe^{3+} in tetrahedral sites and $Fe^{2.5+}$ in octahedral sites. [14] The site population for Fe^{2+} from Figure 6.2 (b) is found to be 28%, therefore the site population for Fe^{3+} is calculated to be 72%. These results lead to the conclusion that the iron oxide nanoparticles are composed of about 72% magnetite (28 %Fe^{2+} and 48 % Fe^{3+}) and 28 % maghemite. The calculations are based on the fact that the Mössbauer spectrum of magnetite, below Verwey temperature, consists of two magnetic sub-spectra, corresponding to Fe^{2+} and Fe^{3+} with intensity ratio 2:1.

The Mössbauer studies of the thin films consisting of 16 DOPA polymer/iron oxide bilayers are carried out at room temperature. Figure 6.3 depicts the Mössbauer spectra in the presence and absence of magnetic field. The external magnetic field is applied in two different orientations, perpendicular to the thin film surface (Figure 6.3 (b)) and parallel to the surface of the film (Figure 6.3 (c)). The results are summarized in Figure 6.3.
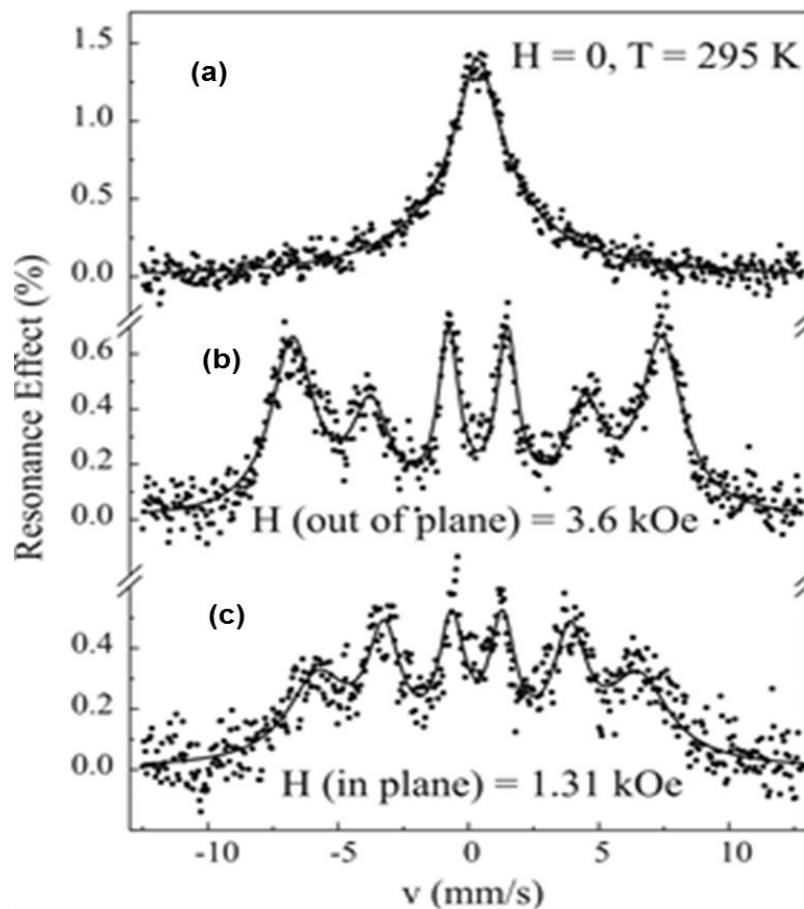
Figure 6.3. ^{57}*Fe Mössbauer spectra of a thin film consisting of 16 bilayers of DOPA polymer and iron oxide nanoparticles. The measurements are made at room temperature in the absence of magnetic field (a) and in magnetic fields oriented perpendicular (out of plane) (b) and parallel to its surface (in plane) (c).*

The Mössbauer spectrum of the thin films of DOPA polymer/iron oxide nanoparticles in the absence of magnetic field (Figure 6.3 (a)) at room temperature, gives a chemical shift of 0.352 mm/s with f ~ 200 MHz. This implies the possibility to achieve slow relaxation in the hybrid thin films applying a magnetic field at room temperature. When an external magnetic field of 3.6 kOe is applied perpendicular to the surface of the thin film, the spectrum changes considerably (Figure 6.3 (b)). The Mössbauer spectrum in this case indicates static magnetic hyperfine splitting of H_{hf} = 440 kOe and a preferential orientation of magnetic

moments "out of plane". The chemical shift observed in this case is $\delta = 0.342$ mm/s.

The third case relates to measurement of the Mössbauer spectra of the thin films in a lower external magnetic field of 1.3 kOe directed parallel to the surface of the thin film (Figure 6.3 (c)). The chemical shift observed in this case is 0.348 mm/s. The application of magnetic field of 1.3 kOe oriented "in plane" shows similar spectral transformations to the case (b) but with "in plane" orientation of magnetic moments. The magnetic hyperfine splitting, H_{hf} is smaller in this case and equal to 382 kOe. This lower value can also be due to the anisotropy present within the thin films which can be responsible for the different observed spectra obtained at out-of-plane or in-plane orientation. However, further experiments are required to lead to conclusions. Magnetic measurements (SQUID) and neutron scattering experiments of the thin films are currently in progress.

6.3. Conclusions

The transparent thin films of a DOPA polymer and iron oxide nanoparticles consisting of 16 bilayers are characterized by conversion electrons Mössbauer spectroscopy (CEMS). The results reveal the iron oxide nanoparticles to be a mixture of maghemite (28%) and magnetite (72 %). A superparamagnetic (dynamic) behavior typical for iron oxide nanoparticles is observed, indicating a particle size of about 4-5 nm. The measurements are carried out in the absence of a magnetic field. The Mössbauer measurements demonstrate that the magnetic dynamics of nanoparticles can be modified by relatively weak magnetic fields. The considerable change in spectra observed in the presence of external magnetic fields applied perpendicular and parallel to the surface of the thin films, shows that it is possible to obtain a static magnetic spectrum at low applied magnetic fields at room temperature. The outlook involves further experiments including polarized neutron reflectometry to determine whether application of external magnetic field can influence the interaction between magnetic nanoparticles and induce a magnetic ordering in thin films. The optical transparency of the hybrid thin films is an advantage that can be used to fabricate opto-magnetic devices and recording media.

6.4. Instrumentation

The Mossbauer spectra are obtained at room temperature and 5.9 K (for iron oxide nanoparticles only) with a constant acceleration transmission Mossbauer spectrometer and ^{57}Co (Rh) source. An α-Fe foil is used to calibrate the Mossbauer spectrometer in a velocity range of ±10 mm/s. The spectra for thin films are measured from spin-coated and transparent thin films on glass substrate of 3x3 cm in size.

Bibliography

1. K. Rabinovitch and H. Schechter, *J. Appl. Phys*. **1968**, 39, 2464.

2. G. Lugert, G. Bayreuther, S. Lehner, G. Gruber and P. Bruno, **Mat. Res. Soc. Symp. Proc**. **1991**, 232, 97.

3. N. I. Chistyakova, A. A. Shapkin, T. V. Gubaidulina, M. E. Matsnev, R. R. Sirazhdinov, V. S. Rusakov, *Hyperfine Interact*. Springer, **2013**, ISSN: 0304-3843.

4. J. Pyun, *Polymer Rev*. **2007**, 47, 231.

5. K. C. Souza, G. –S. Alvarez, J. D. Ardisson, W. A. A. Macedo and E. M. B. Sousa, *Nanotech*. **2008**, 19, 185603.

6. T. Shinjo, *Proc Jpn Acad Ser B Phys Biol Sci*. **2013**, 89, 80.

7. D. Yokoyama, K. Namiki, H. Fukasawa, J. Miyazaki, K. Nomura and Y. Yamada, *J. Radioanal. Nucl. Chem.* **2007**, 272, 631.

8. S. S. Shinde, S. S. Meena, S. M. Yusuf and K. Y. Rajpure, *J. Phys. Chem. C*. **2011**, 115, 3731.

9. P. Auric, S Bouat and B Rodmacq, *J. Phys. Condens. Matter*. **1998**, 10, 3755.

10. S. Sun and H. Zeng, *J. Am. Chem. Soc*. **2002**, 124, 8204.

11. M. N. Tahir, M. Eberhardt, P. Theato, S. Faiß, A. Janshoff, T. Gorelik, U. Kolb and W. Tremel, *Angew. Chem. Int. Ed*. **2006**, 45, 908.

12. M. Eberhardt, R. Mruk, R. Zentel and P. Theato, *Eur. Polym. J*. **2005**, 41, 1569.

13. K. Haneda and A. H. Morrish, *J. Physique*. **1977**, 38, C1-321.

14. G. M. Costa, E. Grave, M. A. Bakker and R. E. Vandenberghe, *Clays Clay Miner*. **1995**, 43, 656.

7

Conclusions and Outlook

This thesis is a documentation of work carried out to evolve a method of fabrication of hybrid Bragg stacks composed of alternating layers of various polymer and nanoparticles constituents with a high degree of control and the subsequent characterization of these systems to study their phononic, mechanical and magnetic properties. A soft matter approach of fabrication of one-dimensional phononic nanostructures is adopted in contrast to the well-established semi-conductor fabrication techniques. The strategy of building up the multilayered nanostructures involves using a soft polymeric component and hard inorganic nanoparticles to form a hybrid with novel properties. Modification of the constituent materials leads to different applications, spanning a wide area ranging from phononics to hard and adhesive coatings and magneto-optic devices.

The *1st chapter* of this thesis is an introduction to structural organization in nanomaterials including information about Bragg stacks. The chapter includes a detailed narrative on phononic crystals and the theory behind phononic band gaps. In particular, hypersonic phononic structures are highlighted and an overview of the methods of fabrication used to obtain them is specified. This document demonstrates the effectiveness of the fabrication approach to fabricate 1-D hypersonic phononic structures with a high degree of control and to provide a complete description of the band structure using the non-destructive technique of Brillouin Light Spectroscopy (BLS). The *2nd chapter* describes in detail the principle methods employed during the experiments. An account of the steps taken to make stable precursor solutions for fabricating hybrid Bragg stacks of poly (methyl methacrylate) (PMMA) and porous silica (p-SiO$_2$) nanoparticles is provided. High speed spin coating is adopted to fabricate multilayers of these constituents in an alternating fashion, interspersed with steps of heat treatment. The whole procedure is designed to ensure superb control on the thickness, homogeneity and sequence of individual layers in the Bragg stack.

The *3rd chapter* is a detailed study on the fabrication of 1-D Bragg stacks consisting of ten bilayers of alternating PMMA and p-SiO$_2$ using a designed spin-coating procedure. The multilayers show well-defined and large phononic "Bragg" gaps for wave propagation along the periodicity direction. A full theoretical description of the band structure, the width and position of the band gap and the intensities of the branches near the Brillouin gap is provided to compliment the experimental dispersion relation obtained through BLS. The influence of structural parameters on the band diagram is investigated by carrying out these studies on Bragg stacks consisting of same materials but different lattice spacing. Measurements done under oblique incidence suggest a new way to engineer the phononic band gap and allow an estimation of the shear modulus of the individual layers. It is observed that the phononic band gap remains robust to structural imperfections in the multilayers. The high-quality periodic structures produced at the nano scale using a soft matter approach allow an easy control over the elastic impedance contrast, making realization of large phononic band gaps possible.

The hypersound propagation in hybrid superlattices (SLs) of PMMA/SiO$_2$ containing a variety of defects is described in the *4th chapter*. Experiments suggest that the phononic band structure is very sensitive to changes in periodicity. The first clear experimental evidence of the existence of surface and cavity modes in phononic superlattices characterized by BLS and supported by theoretical calculations is presented. The subsequent interaction between surface and cavity modes depending on the position and thickness of the defect layers is clearly documented. The fabrication procedure enables superb control to obtain phononic structures of specific requirements in which the BLS measurements show a strong response to layer thickness and sequence, which can lead to phononic devices based on soft matter. Dynamic tuning of cavity modes and their interaction with other defect modes under external stimuli is also possible as a future venture. In addition, theoretical simulations suggest an optical stop-band in addition to the phononic band gap in these hybrid superlattices, which makes them *phoxonic* in nature and thus paves way for further studies concerning acousto-optic interactions.

The *5th chapter* is a documentation of the high mechanical properties exhibited by multilayers of a DOPA rich polymer and iron oxide nanoparticles (Fe$_3$O$_4$) prepared by a spin coating procedure similar to the one employed in the fabrication of phononic crystals. The inspiration for this work comes from the high strength shown by biological materials e.g. nacre and properties such as marine mussel adhesion. The interactions between the catechol groups of the DOPA-polymer

and Fe_3O_4 nanoparticles in a system of alternately packed multilayers gives a cross-linked network that imparts strength to the hybrid and greatly enhances its mechanical properties. The elastic modulus (E) of these hybrid multilayers is ~ 24 GPa, which is significantly higher than hybrid composites previously reported using other fabrication methods. This approach is applicable for different polymers and a large variety of inorganic building blocks, paving the way to a new family of bio-inspired materials. The multilayers can be employed in future as hard and adhesive coatings. Additionally, it is shown in the *6th chapter* that multilayers of DOPA-polymer/Fe_3O_4 characterized by Mössbauer conversion electrons spectroscopy (CEMS) show that the magnetic dynamics of nanoparticles can be modified by relatively weak magnetic fields. Further neutron refractometry experiments are planned to investigate the possibility of inducing a magnetic ordering in the structurally ordered thin films by application of external magnetic field. The optical transparency of the hybrid thin films is an advantage that can be used to fabricate opto-magnetic devices and recording media.

8

Appendix

8.1. Control of Thickness of Silica Layers in Superlattices

As referred to in Section 2.3 of this thesis, the concentration of the silica precursor solution has to be controlled (along with some other parameters) to obtain a layer of desired thickness. For this purpose, ellipsometric measurements of the spin coated stacks provide a slope of 1.49 nm / (g/L). If *d* is the thickness of the silica layer, the required concentration of the silica dispersion (*c*) is a ratio of *d* and the slope. (*c = d (nm) / slope (nm/gL⁻¹)*). The amount of SDS and ammonia that should be added to the silica dispersion in water depends on the volume of the precursor solution to be prepared. Therefore, a silica layer of 50 nm in the phononic Bragg stacks (described in Chapters 3 and 4) can be obtained from mixing 33.4 g/L silica dispersion in water (LUDOX AS-30) with 200 µL of SDS and 18.14 mL of NH_3 to obtain a precursor solution of 20 mL. Careful calculations along these lines enable us to make silica layers of desired thickness with a high degree of precision.

8.2. Theory of Light Scattering in BLS and Green's Method

The work presented in Chapter 3 and 4 of this thesis employs Brillouin Light Spectroscopy as a characterization technique that investigates phonons in condensed matter. Applying the classical theory of light scattering, the phonons are treated as waves with wavelengths in the range of nanometers (in this case). The classical theory assumes the medium (sample) to consist of small volume elements. The incidence of light on these volume elements creates a dipole moment leading to scattering. Depending on the position of the volume elements, the scattered waves differ in phase only and subsequently, interference takes place. Destructive interference cancels out scattered waves of equal amplitude but opposite phase if the induced

polarization is constant. Hence, the total scattered light in all directions will be zero except in the forward direction. However, some fluctuations in the dielectric constant always take place in the real medium due to the thermal motion of the atoms. As a result, only partial interference takes place and the scattered light in directions other than forward may not be zero, so this factor has to be taken into account in the theoretical calculations. Further theory on light scattering in condensed matter can be obtained here. [1]

In Chapters 3 and 4 of this thesis, the computation of BLS spectra is based on the calculation of the density of vibrational states (DOS) and photo-elastic coupling between material displacements and fluctuations in the refractive index. The calculations are based on the Green's function technique and the theory of interface response in the frame of the elasticity theory. [2] Some details of the method have been provided in Section 3.2.3 of this thesis but a few remaining points relevant to the work are discussed here. In computing the BLS spectra for the Bragg stacks of PMMA and p-silica, the modulation caused by the displacement of the interfaces ($\delta \varepsilon'$) is considered to be negligible except at the surface. The dielectric modulation of the multilayers can be neglected when the layers are thin as compared to the probing optical wavelength. The same is true if the layers show almost the same refractive indices. Therefore, the superlattices discussed in Chapter 3 and 4 can be considered a homogeneous medium from the optical point of view. The intensity of the Brillouin scattering (I_s (ω, $q_\perp$)) is therefore directly proportional to the scattered field, E_s (ω, $q_\perp$). The thickness variations in the phononic structures caused during the course of fabrication are not considered in these calculations, since they do not greatly affect the Brillouin spectra as described in Section 3.2.6.

8.3. Confocal Microscopy

Section 3.2.1 of this thesis refers to characterization of the 1-D Bragg stacks of PMMA/p-SiO$_2$ using confocal microscopy. A confocal microscope (NanoFocus® µSurf®) is used to determine the total thickness of the stacks. This robust method uses a white light confocal measurement head that is moved stepwise in z-direction. The stacks are scratched near the position of BLS measurement and the z-difference between substrate and sample surface indicated the actual total thickness. Figure 7.1 shows the results of the measurements on stack A, as described in Chapter 3 of this thesis using confocal microscopy.
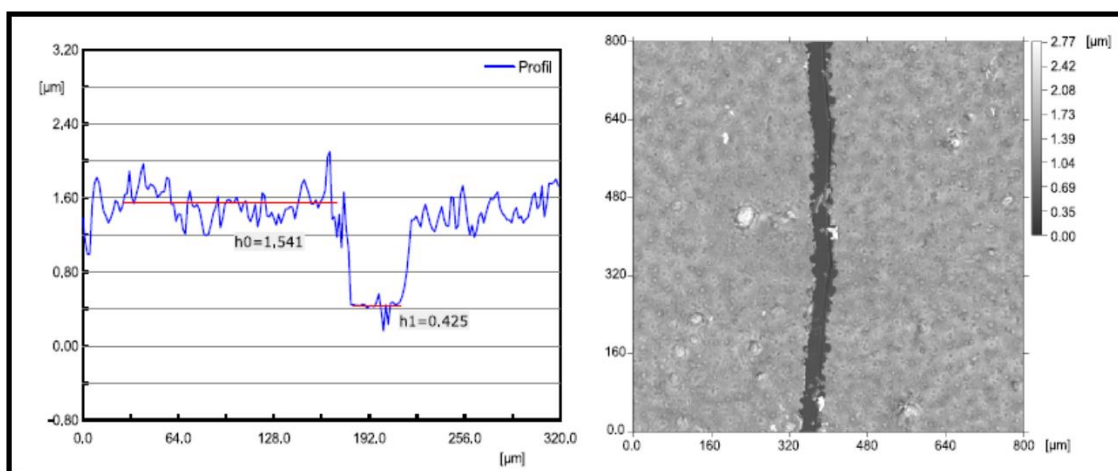
Figure 8.1. *Profile and height image of stack A obtained by confocal microscopy. The difference in height between the bottom of the scratch and the top level defines the total thickness d.*

8.4. Further Characterization of Catechol-Polymer/Fe₃O₄ Nano-hybrid Multilayers

The polymer poly (pentafluorophenyl acrylate) and the catechol polymer were synthesized using ^{1}H and ^{19}F NMR spectroscopy, as shown in Figures 8.2 and 8.3.
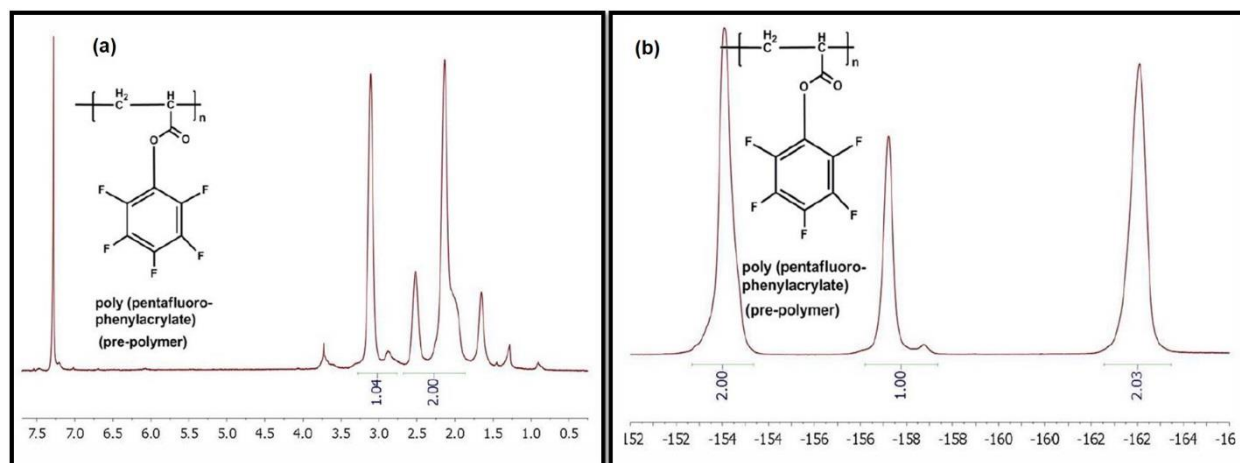
Figure 8.2. (a) ^{1}H and (b) ^{19}F NMR spectrum of poly (pentafluorophenyl acrylate)
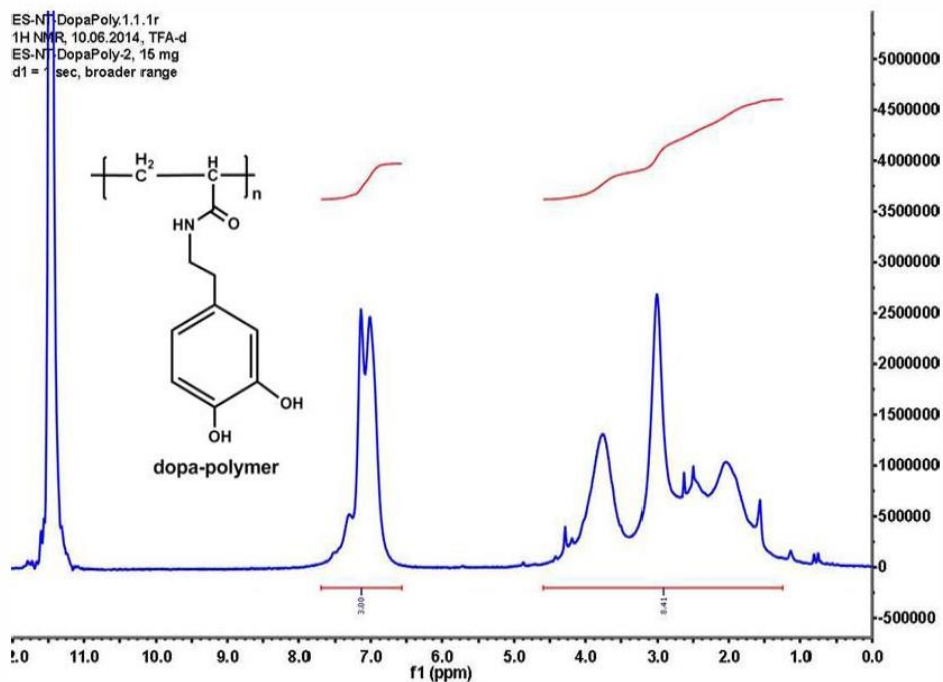
Figure 8.3. ^{1}H NMR spectrum of the dopamine modified polymer

8.4. Determination of Mechanical Properties by Nanoindentation

Nanoindentation is a technique frequently used to determine the mechanical properties of thin films, hybrids as well as other materials. The method consists of applying a load to the indenter which is in contact with the sample. The depth of indentation is measured as the load is applied and the area of contact (A) is calculated based on the radius of the indenter and depth of the indentation. The hardness (H) of the material is obtained as the ratio of maximum applied load divided by the indenter contact area at that load. The Young's modulus of the material (E) is determined from the slope of the onset of the unloading curve. The Young's modulus and hardness are calculated by fitting the indentation curves according to the Oliver-Pharr method [3] that assumes deformation during loading to be elastic as well as plastic in nature. Only the elastic displacements are considered during unloading to simplify the modeling. The hardness is determined from the equation 8.1.

$$H = \frac{P_{max}}{A} \tag{8.1}$$

The elastic modulus can be calculated from Equaions 8.2 and 8.3 where S is the stiffness of the material, E_{eff} is the effective elastic modulus and υ is the Poisson's ratio. The values E_i and υ_i are considered for the indenter and β is a dimensionless parameter that accounts for deviations in stiffness caused by different indenters. The equation 8.2 is general and not limited to any specific geometry of the indenter used.

$$S = \beta \, \frac{2}{\sqrt{\pi}} E_{eff} \sqrt{A} \tag{8.2}$$

$$\frac{1}{E_{eff}} = \frac{1-\upsilon^2}{E} + \frac{1-\upsilon_i^2}{E_i} \tag{8.3}$$

Bibliography

1. T. Still, *High Frequency Acoustics in Colloid-Based Meso and Nanostructures by Spontaneous Brillouin Light Scattering*; Springer-Verlag: Heidelberg, **2010.**

2. E. El Boudouti, B. Djafari-Rouhani, A. Akjouj and L. Dobrzynski, *Surf. Sci. Rep*. **2009**, 64, 471.

3. W. C. Oliver and G. M. Pharr, *J. Mater. Res*. **1992**, 7, 1564

List of Figures

List of Figures

List of Tables

List of Schemes

Abbreviations

PMMA   Poly (methyl methacrylate)

p-SiO$_2$ porous silica

LbL   layer by layer

SDS   Sodium dodecyl sulphate

BL   bilayers

BLS   Brillouin Light Scattering

FPI   Fabry-Perot Interferometer

SEM   Scanning Electron Microscopy

DOS   Density of States

SL   Superlattice

DOPA   3, 4-dihydroxyphenylalanine

TEM   Tunneling Electron Microscopy

AFM   Atomic Force Microscopy